

**SELECTIVE EXHALED BREATH CONDENSATE COLLECTION AND
COMPETITIVE FLUORESCENT BIOSENSOR FOR NON-INVASIVE
GLUCOSE DETECTION**

by

Divya Tankasala

A Dissertation

Submitted to the Faculty of Purdue University

In Partial Fulfillment of the Requirements for the degree of

Doctor of Philosophy



Weldon School of Biomedical Engineering

West Lafayette, Indiana

August 2020

**THE PURDUE UNIVERSITY GRADUATE SCHOOL
STATEMENT OF COMMITTEE APPROVAL**

Dr. Jacqueline Linnes, Chair

Weldon School of Biomedical Engineering

Dr. Tamara Kinzer-Ursem

Weldon School of Biomedical Engineering

Dr. Kieren Mather

Eli Lilly

Dr. Kinam Park

Weldon School of Biomedical Engineering

Approved by:

Dr. George R. Wodicka

Dedicated to my beloved grandmother, Lalitha, who never stopped cheering for me, and to my parents, Kumar and Savita, for their unwavering love and support.

ACKNOWLEDGMENTS

This dissertation is the culmination of many years of support, guidance, and encouragement from many individuals towards whom I am eternally indebted.

I would first like to thank my PhD advisor, Dr. Jacqueline Linnes, for welcoming me with open arms to join her research lab, which was just starting out, five years ago. Jackie has the rare gift of looking past an individual's scorecard metrics and seeking out the qualities that truly determine their ability to succeed as a researcher. She fearlessly took a chance on four individuals in the fall of 2015 and her charismatic and nurturing mentorship style allowed us to flourish into confident and inquisitive researchers. Her boundless curiosity and eagerness to dive headfirst into challenging projects has rubbed off on me, and I will continue to be inspired by her drive to help make the world a better place through science and engineering. To me, Jackie will always be the gold standard of what a mentor should be, and I hope to emulate her congenial optimism and enthusiasm for science, even on the toughest of days.

I am grateful for the guidance and support from all of my committee members, Dr. Tamara Kinzer-Ursem, Dr. Kieren Mather, and Dr. Kinam Park. Dr. Kinzer-Ursem's expertise in protein engineering and impeccable attention to detail in experimental design were conducive to my growth as a scientist. Her confidence in my research direction encouraged me to persevere through the challenges associated with traversing a path slightly different from my lab mates. Dr. Kieren Mather was instrumental in designing the study that allowed me to bring my research to the bedside, thanks to the partnership between Purdue University and the Indiana University Clinical and Translational Sciences Institute (CTSI). I am thankful for his valuable input as an endocrinologist and for the extraordinary opportunity to evaluate the feasibility of my device on diabetic patients – something few graduate students get to do. Dr. Kinam Park encouraged me to think beyond the bench and consider the translatability of my research. I am humbled by his wisdom and unwavering support for this challenging project, of which he is one of the pioneers. In that regard, I am especially grateful to Dr. Ann Rundell, who ambitiously took over this project from Dr. Leslie Geddes, the founder of the Weldon School of Biomedical Engineering. Thus, it has been a true honor and privilege to have worked on this project.

Outside of my committee, I would like to acknowledge the faculty and staff in the Weldon School of Biomedical Engineering who supported me in countless ways during my graduate school

journey. Dr. Karin (Kaisa) Ejendal is a phenomenal role model for me and has inspired me to be a versatile and resilient researcher. Thank you for always being up for the challenge of brainstorming new ideas to troubleshoot my experiments and for cheering me on throughout my PhD. I would also like to acknowledge Norvin Bruns and David McMillan for their invaluable expertise and guidance in designing the many iterations of my device and for also being excellent resources for the undergraduate students I have mentored. In addition, I thank Dr. Asem Aboelzahab, Dr. Lester Smith, and Dr. Rucha Joshi for cultivating my leadership and mentoring skills while I served as a teaching assistant for BME undergraduate courses. I would like to acknowledge Dr. Yunjie Tong for graciously allowing us to use his lab's end-tidal CO₂ measurement system and Dr. Kavita Shah for her tremendous guidance in improving my molecular cloning techniques. I am especially indebted to Tammy Siemers for her tireless efforts in coordinating numerous professional development opportunities and for taking the time to mentor and guide each individual graduate student through their professional journeys. Her fantastic coordination of the Boston BME industry trip in 2016 inspired me to seek out career opportunities on the east coast. Special thanks also goes out to Sandy May, Bill Schoenlein, Susan Hardy, Kirk Foster, Jo Gelfand, Kitty Cooper, Pam Lamb, Linda Doyle, and Carla Brady for all they do in terms of academic and departmental support to make the Weldon School of Biomedical Engineering a wonderful place to work.

I would like to thank the Bechtel Innovation Design Center, the Purdue Genomics Core Facility, the Purdue Statistics Department, and the Purdue Proteomics Facility for supporting numerous aspects of my thesis work. For two years of my PhD, I was supported by the NIH-sponsored T-32 fellowship for Bioengineering Interdisciplinary Training in Diabetes (BDTR), which provided me the unique opportunity to conduct translational research with the support from collaborators such as Dr. Mather and clinical pilot study coordinators Tonya Hamilton and Nick Patel. Thanks to this fellowship and the Joe Bourland travel grant, I was also able to attend several academic conferences in Minneapolis (BMES, AIChE), Honolulu (IEEE EMBS), and Orlando (AIChE), to disseminate my research and learn from colleagues in the scientific community. I am also grateful to the CTSI Pilot and Feasibility grant and the NIH NIBIB R21 Award that funded my research for three years.

I am incredibly grateful to have started my PhD journey alongside three individuals – Elizabeth Phillips, Taylor Moehling, and Orlando Hoilett. I will cherish the memories of our first year together helping to establish the lab and figuring out how to function as grad students. It has

been exciting to watch the lab grow since then, and I am thankful for the support and encouragement from all the lab members over the years, including K, Laud Anthony, Ashlee, Somi, Mindy, Emilie, Jay, Amy, Emeka, Hui, and Emilee. Outside the Linnes Lab, I would like to thank Aya Saleh, Julia Fraseur, and Scott Bolton, for taking the time to train me in several protein engineering techniques and for lending an ear to bounce off new research ideas. Furthermore, it has been an honor to mentor several exceptional undergraduate students, including Shubhankar, Gabe, Adit, Mickey, Maddie, and Pankti.

My friends have been my biggest source of support and encouragement through all the ups and downs of graduate school. I could not have gotten through the last five years without Taylor Moehling – my lab mate and close friend. I admire your work ethic, grit, and fearlessness – and I can say for certain that it has made me a better person. I am also proud to call Katherine Clayton my mentor and friend – thank you for always believing in me. Your tenacity and dedication to global health is matched by your fierce support for your friends, and I appreciate the invaluable advice you have given me along the way. I would also like to thank Tanaya Walimbe for being nothing short of a big sister to me during my initial few years at Purdue and for helping me adjust to life in West Lafayette. In addition, I am thankful for wonderful friends like Elizabeth, K, Liesl, Kelsey, Carmen, Rachel, and Andrea, whose company was appreciated during many climbing trips, potlucks, and weekend get-aways. Special shout-out goes to my amazing friends from high school and undergrad – Sunny, Mallika, Anu, Sheryl, Katie, and Sonia. Thank you for always supporting me from afar and never hesitating to pick up a call when things got tough. I would also like to thank my cat, Arya, for providing endless love, cuddles, and laughter to get through the isolating aspects of graduate school, especially during a pandemic.

Lastly, I wouldn't have been able to complete my PhD without the unwavering support from my family. Special thanks to my late grandmother, Lalitha Tankasala, who made sure I never saw any limitations in my education. I hope I have made her proud. I would like to thank my grandparents, Dr. M.M. Rao and Padma Mathihalli, for encouraging me to pursue a PhD – my grandfather is my biggest inspiration for my love of science. Thank you to my brother, Raghav, for being my rock – I am continually inspired by your perseverance and am grateful for all your pep talks. Finally, thank you to my parents, Kumar and Savita Tankasala, for giving me the world and instilling in me a sense of ambition with humility. The confidence I have today is because of your unconditional love and indomitable belief in me.

TABLE OF CONTENTS

ACKNOWLEDGMENTS	4
TABLE OF CONTENTS.....	7
LIST OF TABLES	11
LIST OF FIGURES	12
LIST OF ABBREVIATIONS.....	16
ABSTRACT.....	18
1. INTRODUCTION	19
1.1 Diabetes Mellitus	19
1.1.1 Management of disease	19
1.1.2 Advantages of non-invasive glucose detection	20
1.1.3 Non-invasive glucose-containing sample matrices	21
1.2 Airway surface liquid (ASL) glucose	21
1.2.1 Regulation of glucose from blood into ASL	22
1.2.2 Transport of glucose from ASL into exhaled breath condensate (EBC).....	23
1.2.3 Effect of diabetes and lung-related co-morbidities	24
1.3 Collection of EBC.....	24
1.3.1 Variable dilution factors.....	25
1.3.2 Surface materials for condensation and collection.....	26
1.3.3 Salivary contamination in EBC.....	27
1.4 Glucose detection methods for EBC.....	27
1.4.1 Biosensor specifications	27
1.4.2 Protein-based enzymatic glucose recognition elements.....	28
1.4.3 Protein-based non-enzymatic glucose recognition elements	31
1.5 Thesis overview: selective EBC collection and competitive fluorescent biosensor for non-invasive glucose detection	33
2. DEVELOPMENT OF AUTOMATED CONDENSER FOR SELECTIVE COLLECTION OF RESPIRATORY ZONE EBC.....	36
2.1 Rationale	36
2.2 Materials and Methods.....	38

2.2.1	Time-based selective EBC collection using solenoid valve.....	38
2.2.2	Temperature-based selective EBC collection using balloon valve	43
2.3	Results and Discussion	49
2.3.1	Time-based selective EBC collection via solenoid valve	49
2.3.2	Temperature-based selective EBC collection via balloon valve.....	51
2.4	Future Directions	56
2.5	Conclusion	56
3.	CHARACTERIZATION OF BLOOD AND BREATH GLUCOSE PROFILES IN NORMOGLYCEMIC AND DIABETIC INDIVIDUALS	57
3.1	Rationale	57
3.2	Materials and Methods.....	57
3.2.1	Subject selection and preparation.....	57
3.2.2	Blood and breath sampling.....	57
3.2.3	Statistical methods.....	58
3.3	Results and Discussion	60
3.4	Future Directions	65
3.5	Conclusion	66
4.	ENGINEERING GLUCOSE BINDING PROTEIN (GBP) WITH CHEMO- ENZYMATIC TAG.....	67
4.1	Rationale	67
4.2	Materials and Methods.....	69
4.2.1	Cloning of engineered mglB constructs	69
4.2.2	Protein expression and bio-orthogonal labeling of engineered GBP	70
4.2.3	Cell lysis and protein analysis.....	71
4.2.4	Proof-of-concept selective conjugation of 12-ADA-GBP from lysate	71
4.3	Results and Discussion	73
4.3.1	Cloning of mglB constructs with NMT sequence	73
4.3.2	Protein expression and bio-orthogonal labeling of GBP.....	74
4.3.3	Selective conjugation of 12-ADA-GBP from lysate.....	76
4.4	Future Directions	78
4.5	Conclusion	78

5.	SELECTIVE CONJUGATION OF GBP TO QUANTUM DOTS	79
5.1	Rationale	79
5.2	Materials and Methods.....	79
5.2.1	Enrichment of 12-ADA-GBP from lysate via anion exchange.....	79
5.2.2	Characterization of amino-PEG quantum dot (NH ₂ -QD) size (nm) and polydispersity index (PdI).....	80
5.2.3	Functionalization of NH ₂ -QDs with DBCO.....	80
5.2.4	Conjugation of 12-ADA-GBP to DBCO-QD via SPAAC	82
5.3	Results and Discussion	82
5.3.1	Enrichment of 12-ADA-GBP from lysate.....	82
5.3.2	Mass-spectrometry analysis of expressed protein lysate.....	84
5.3.3	Characterization of QD hydrodynamic size (nm) and polydispersity (PdI).....	85
5.3.4	Functionalization of QDs for azide reactivity	87
5.3.5	Conjugation of 12-ADA-GBP to DBCO-QDs via SPAAC	88
5.4	Future Directions	89
5.5	Conclusion	91
6.	COMPETITIVE FRET-BASED DETECTION OF GLUCOSE USING GBP-QD SENSOR	92
6.1	Rationale	92
6.2	Materials and Methods.....	93
6.2.1	Synthesis of custom ligand quenchers and fluorophores	93
6.2.2	Calibration of QD-FRET with ligand acceptors	94
6.2.3	FRET efficiency of ligand acceptors on GBP-QD and unbound QD	95
6.2.4	Glucose-responsive FRET curves using GBP-QD ligand acceptor system.....	96
6.3	Results and Discussion	98
6.3.1	Calibration of QD FRET with acceptor ligands.....	98
6.3.2	Comparing FRET signals of ligand acceptors on GBP-QD and unbound QD ...	100
6.3.3	Glucose-responsive FRET efficiency curves using GBP-QD ligand system	102
6.4	Future Directions	105
6.4.1	Characterization of ligand binding to GBP.....	105
6.4.2	In vitro evaluation of competitive FRET biosensor response	106

6.5 Conclusion	107
7. CONCLUSION.....	108
APPENDIX A. SUPPLEMENT TO CHAPTER 2.....	109
APPENDIX B. SUPPLEMENT TO CHAPTER 3.....	114
APPENDIX C: SUPPLEMENT TO CHAPTER 4.....	115
APPENDIX D. SUPPLEMENT TO CHAPTER 5.....	120
APPENDIX E. SUPPLEMENT TO CHAPTER 6.....	126
REFERENCES	130
PUBLICATIONS.....	140

LIST OF TABLES

Table 2.1. Glucose ratio and expiratory volume to condensate volume characterization.	50
Table 2.2. Effect of threshold and expiratory volume on EBC collection (n=3, mean \pm SD).	54
Table 2.3. EBC volume and glucose concentration of condensates collected from tray and R-Tube (n=3, mean \pm SD).	55
Table 5.1. Identity and size of proteins with highest abundance in overexpressed lysate.	85
Table 6.1. Ligand acceptor name, purity, and molecular weight (g/mol).	94
Table 6.2. GBP-QD ligand glucose detection system and control well components.	97
Table A.1. Subject details and capnography data signals used to calculate time ratios representative of dead space air to total exhaled volume.	109
Table B.1. Inclusion and exclusion criteria for OGTT pilot study subject selection.	114
Table C.1. Deep Vent high fidelity polymerase chain reaction protocol for wt-mglB.	115
Table C.2. Primer designs for engineering mglB with NMT recognition sequence.	116
Table C.3. Deep Vent high fidelity PCR protocol for RS1 and RS2-mglB.	117
Table C.4. DNA double-digest protocols for pET15b and RS1-mglB.	118
Table C.5. Plasmid/gene ligation protocols for experimental and control samples.	118

LIST OF FIGURES

Figure 1.1. Airway glucose homeostasis.	23
Figure 1.2. Method of condensing exhaled breath.....	25
Figure 1.3. Overall structures of GBP.	32
Figure 2.1. Components of exhaled air from various regions of respiratory tract.....	36
Figure 2.2. Diagram of selective valve opening and closing for capturing deep lung air and exclusion of anatomical dead space air.....	37
Figure 2.3. Capnography diagram depicting the phases of expiratory CO ₂ content.....	38
Figure 2.4. Front view of condenser prototype pictured with PCB circuit, Rev. C wind sensor, breathing tube, heat sink/Peltier cooler assembly, and solenoid valve.....	41
Figure 2.5. Top view of condenser prototype with embedded CO ₂ sensor.	42
Figure 2.6. Selective EBC collection device.	45
Figure 2.7. Circuit wiring of the four-relay module to the Arduino Uno microcontroller and balloon valve pneumatic actuator.	46
Figure 2.8. Representation of feasibility study set-up for data collection.	47
Figure 2.9. Overlay of temperature profile and time-based valve actuation.	49
Figure 2.10. Overlay of temperature-valve actuation, and CO ₂ data for a single exhalation.	50
Figure 2.11. Temperature and end-tidal CO ₂ profile comparison.	51
Figure 2.12. Overlay of temperature profile, temperature-based valve action, and dynamically calibrated selection threshold (40%).....	52
Figure 2.13. Temperature-based actuation and CO ₂ plateau comparison at 0%, 50%, and 70% thresholds.....	53
Figure 2.14. Comparison of glucose concentrations between 0% and 70% thresholds.	55
Figure 3.1. Blood and EBC glucose profiles for (a-b) normoglycemic and (c-d) type 2 diabetic subjects over time during oral glucose tolerance test. Dashed lines indicate time of glucose drink consumption.....	60
Figure 3.2. Blood to EBC glucose ratios for normoglycemic and type 2 diabetic subjects.	61
Figure 3.3. Linear model of EBC glucose to blood glucose.....	62
Figure 3.4. Correlogram of the observed EBC glucose profile with blood glucose profiles at various time lags, h, for normoglycemic subject N02.	63
Figure 3.5. Linear model of time-lag adjusted EBC glucose to blood glucose for normoglycemic subject N02.	64

Figure 4.1. Azide-alkyne cycloaddition reaction schematics. (A) Copper-catalyzed azide-alkyne cycloaddition; (B) Strain-promoted azide-alkyne cycloaddition. Both form triazole products....	68
Figure 4.2. Chemo-enzymatic labeling of GBP within E. coli expression system when co-expressed with NMT in the presence of 12-ADA.	69
Figure 4.3. Engineered constructs of <i>mglB</i> . The <i>wt-mglB</i> was inserted into the pGEM T-Easy vector; the remaining constructs were inserted into the pET15b vector.....	70
Figure 4.4. Diagnostic restriction digest of successfully cloned RS1- <i>mglB</i> in pET15b vector. ..	73
Figure 4.5. Expression levels of WT vs engineered GBP (RS1 & RSI-His) without fatty acid tags (32 kDa).	74
Figure 4.6. Expression of 12-ADA-GBP in soluble and membrane fractions.....	75
Figure 4.7. Expression levels of 12-ADA labeled GBP (32 kDa) engineered with either RS1 or RS2 recognition sequence in soluble and membrane fractions (5 hours, n=1).....	75
Figure 4.8. Expression of 12-ADA-GBP and Myr-GBP in soluble fraction.	76
Figure 4.9. Selective conjugation of 12-ADA-GBP from cell lysate via strain-promoted azide alkyne cycloaddition (SPAAC).....	77
Figure 4.10. Selective conjugation of 12-ADA-GBP (engineered with RS1 and RS2) to DBCO-TAMRA from clarified lysate.....	77
Figure 5.1. Anion exchange enrichment of 12-ADA-GBP from clarified lysate.	83
Figure 5.2. Mass spectrometry analysis of protein sample.	84
Figure 5.3. Hydrodynamic diameter and polydispersity index (PdI) measurements of QDs in various buffer conditions.	86
Figure 5.4. Fluorescence emission spectra of QD functionalized with DBCO (excitation 380 nm). NH ₂ -QDs refer to unfunctionalized amino-PEG-QDs; DBCOQD-100 – 100:1 ratio of linker to QD; DBCOQD-500 – 500:1 ratio of linker to QD; DBCOQD-1000 – 1000:1 ratio of linker to QD..	87
Figure 5.5. Agarose gel electrophoresis analysis of unbound QD and DBCO-QD (green) azide reactivity with Alexa-647 dye (red). QD0-1000 refers to ratio of DBCO to QD (QD0 = no DBCO; QD1000 = 1000:1 ratio). FT = filtrate sample containing only Alexa dye.	88
Figure 5.6. Confirmation of GBP-QD conjugation via SDS-PAGE analysis.....	89
Figure 6.1. Proposed sensor schematic for FRET-based glucose detection system using GBP-QD conjugates and galactosamine-Alexa-633 acceptor.	93
Figure 6.2. Structures of D-glucose anomers. (a) The beta anomer of D-glucose is the preferred substrate for GBP; (b) the alpha anomer of D-glucose.....	94
Figure 6.3. FRET quenching of unbound QD with increasing molar ratios of quencher:QD. Dashed line represents average fluorescence intensity of QD in absence of quencher.	98
Figure 6.4. Alexa-633 and QD FRET calibration with intensity comparisons.....	99

Figure 6.5. Peak intensity ratio of QD and Alexa-633 ligand with increasing molar ratios. A minimum molar ratio of 1:1 was required to generate a significant decrease in peak intensity ratio from the control (p=0.016, n=3).	99
Figure 6.6. FRET efficiency of Alexa-633 ligand targets on unbound QDs at increasing molar ratios.....	100
Figure 6.7. Comparison of peak intensity ratios for GBP-QD and unbound QD with increasing molar ratios of ligand acceptors.....	101
Figure 6.8. FRET efficiency of ligand acceptors on GBP-QD and unbound QD.	102
Figure 6.9. FRET efficiency of GBP-QD-ligand system in the presence of glucose (0, 0.3, 1, 7 μ M) (n=3).....	103
Figure 6.10. FRET efficiency of GBP-QD-ligand (Target C) system in presence of glucose (0.1-1000 μ M) (N=2, n=2).	104
Figure A.1. Condensation surface for droplets in original prototype of selective condenser.....	110
Figure A.2. Printed circuit board (PCB) schematic to integrate wind and temperature sensor, Arduino microcontroller, solenoid valve, and Peltier cooler.	110
Figure A.3. Selective EBC condenser fitted with R-Tube collection platform (connected to pneumatic balloon T-valve).	111
Figure A.4. Average glucose concentrations in samples collected from R-Tube (n=3).....	112
Figure A.5. Titration curves of the glucose assay buffer (GAB) from the Abnova Glucose Assay Kit using (a) 1 M NaOH and (b) 1 M HCl.....	112
Figure A.6. Combined effects of both NaCl and NH ₄ Cl on the reported fluorescence intensity of a 0.5 μ M glucose solution (n=3).....	113
Figure B.1. Assessing normality of EBC and blood glucose relationship for all data points (normoglycemic- N=2, n=19; diabetic – N=2, n=24).....	114
Figure C.1. Sequencing results confirming successful cloning of RS1-His-mglB into pET15b vector.....	119
Figure D.1. Confirmation of 12-ADA-GBP presence in enriched (first wash) samples.	120
Figure D.2. Gel electrophoresis of DBCO-QDs in pH 6-8, 0.0-0.1% Tween-20.....	120
Figure D.3. Fluorescence spectra and emission intensity of DBCO-QDs clicked (via SPAAC) with Azide-Alexa-Fluor-647.....	121
Figure D.4. QD fluorescence intensity under various buffer conditions.	122
Figure D.5. QD fluorescence emission spectra under various buffer conditions over time.	123
Figure D.6. Protein concentration (BSA) on DBCO-QDs after filtration steps (washes 1-3) and comparison of original and final (reconstituted) concentrations.	124

Figure D.7. Hydrodynamic diameter (nm) of GBP-QD conjugates compared to unfunctionalized QDs.	125
Figure E.1. Molecular structure of ligand quenchers.....	126
Figure E.2. Molecular conjugation structure of ligand acceptor molecules. (a) structure of glucosamine-PEG ₆ -Alexa-Fluor-633 (Target D); (b) structure of galactosamine-Alexa-Fluor-633 (Target A, not synthesized).....	127
Figure E.3. Fluorescence emission spectra of NH ₂ -QD and ligand-Alexa-633 molecules (targets B-D) at increasing molar ratios of Alexa-633:QD (0, 0.1, 10, 20) Excitation wavelength of 380 nm; QD emission at 590 nm; Alexa-633 emission at 645 nm.	127
Figure E.4. Fluorescence emission spectra of NH ₂ -QD and ligand-Alexa-33 molecules (target B-D) at increasing molar ratios of Alexa-633:QD (0, 50-200). QD peak emission measured at 590 nm; Alexa-633 peak emission measured at 645 nm.	128
Figure E.5. Ratio of peak wavelength of QD (590 nm emission) to peak wavelength of ligand-Alexa-633 (645 nm emission, targets B-D) at increasing molar ratios of Alexa-633:QD (n=1).129	
Figure E.6. FRET efficiency of individual ligand acceptors (Targets B-D) on both GBP-QD (closed symbols) and unbound QD (open symbols) at molar ratios (Alexa-633:QD) of 0.5, 1, 2, and 5 (n=4 for 0.5-2, n=1 for 5).	129

LIST OF ABBREVIATIONS

12-ADA	12-azidodecanoic acid
ACF	autocorrelation function
Alexa-633	Alexa-Fluor-633
ALF	alveolar lining fluid
ApE	A plasmid Editor
ASL	alveolar surface liquid
BHQ2	black hole quencher-2
BLI	bio-layer interferometry
CCF	cross-correlation function
CF	cystic fibrosis
CGM	continuous glucose monitoring
ConA	concanavalin A
COPD	chronic obstructive pulmonary disease
CTSI	Clinical and Translational Sciences Institute
CuAAC	copper catalyzed click chemistry
DBCO	dibenzocyclooctyne
DBCO-QD	DBCO-functionalized quantum dot
DTT	dithiothreitol
EBC	exhaled breath condensate
ELF	epithelial lining fluid
EtCO ₂	end-tidal carbon dioxide
FCS	fluorescence correlation spectroscopy
FRET	Forster resonance energy transfer
GBP	glucose binding protein
GBP-QD	GBP-bound quantum dot
GDH	glucose dehydrogenase
GLUT	facultative glucose transporters
GOx	glucose oxidase

HPAEC-PAD	high performance anion exchange chromatograph-pulsed amperometric detection
iBAQ	intensity-based absolute label-free quantification
IPTG	isopropyl β -D-1-thiogalactopyranoside
ISF	interstitial fluid
ITC	isothermal titration calorimetry
K_D	dissociation constant
K_m	Michaelis-Menten constant
LC	liquid chromatography
LTL	low-throughput laboratory
MWCO	molecular weight cut-off
Myr	myristic acid
NH ₂ -QD	amino-PEG coated CdSe/ZnS quantum dot
NMT	N-myristoyl transferase
OGTT	oral glucose tolerance test
pCO ₂	partial pressure of carbon dioxide
PCR	polymerase chain reaction
PdI	polydispersity index
QD	quantum dot
RF	respiratory fluid
RS1	recognition site 1
RS2	recognition site 2
RT	room temperature
SMBG	self-monitoring of blood glucose
SPAAC	strain-promoted azide alkyne cycloaddition
T2D	type 2 diabetic
TAMRA	tetramethylrhodamine
TBE	tris-borate-EDTA
TEM	transmission electron microscopy
W1	first wash

ABSTRACT

Two thirds of patients with diabetes avoid regularly monitoring their blood glucose levels because of the painful and invasive nature of current blood glucose detection. As an alternative to blood sample collection, exhaled breath condensate (EBC) has emerged as a promising non-invasive sample from which to monitor glucose levels. However, the inconsistency in the methods used to collect EBC significantly impacts the reliability of reported analyte concentrations in EBC. Furthermore, this dilute sample matrix requires a highly sensitive glucose biosensor to enable robust and accurate glucose detection at the point-of-care. Together, a reliable collection method and sensitive detection system can enable accurate modeling of glucose transport from blood to breath that is reflective of airway glucose homeostasis.

I address this research gap by simultaneously designing a standardized EBC collection method that allows for separation of dead space and alveolar air and developing a competitive fluorescent biosensor that can resolve micromolar glucose concentrations changes. First, I develop a low-cost, automated condenser that selectively collects exhaled breath that has been exchanged with lung fluid based on the detection of higher breath temperatures that are characteristic of the lower respiratory regions. Using this device, I investigate the relationship between blood and EBC glucose in diabetic and normoglycemic human subjects. Next, I engineer the exquisitely sensitive *E. coli* glucose binding protein (GBP) with a chemo-enzymatic tag to selectively conjugate it to highly photostable quantum dots (QDs). Finally, I take advantage of the competitive binding of glucose ($K_D=0.35 \mu\text{M}$) and galactose ($K_D=1.4 \mu\text{M}$) to GBP to develop a fluorescent glucose biosensor using the GBP-QD conjugate.

1. INTRODUCTION

Parts of this chapter are reproduced from *Translational Research*, 213, D. Tankasala and J. Linnes, “Non-invasive glucose detection in exhaled breath condensate”, 1-22, Copyright © 2019 Elsevier Inc. All rights reserved¹.

1.1 Diabetes Mellitus

Diabetes mellitus is a serious metabolic condition caused by hyperglycemia, which results from either insufficient insulin secretion or defects in insulin action². According to the 2017 National Diabetes Statistics Report from the CDC, approximately 30.3 million people (over 9.4% of the U.S. population) are afflicted with this disease. Diabetes is classified into two primary types: type 1 – insulin-dependent/juvenile-onset diabetes, and type 2 – non-insulin dependent/adult-onset diabetes. Type 1 diabetes affects 5-10% of the individuals diagnosed with diabetes and those individuals are usually under 20 years old. Type 2 diabetes, on the other hand, accounts for 90-95% of the diabetic population and is commonly diagnosed in adults over the age of 20. Furthermore, around 84.1 million individuals have pre-diabetes, which if untreated, can lead to type 2 diabetes within five years³.

1.1.1 Management of disease

Methods exist to manage diabetes and lower blood glucose levels but there is currently no cure for either type. Glycemic control options can reduce the risk of developing severe complications associated with hyperglycemia, such as retinopathy (loss of vision), peripheral neuropathy, and cardiovascular symptoms.² However, if medications or insulin injections are not administered properly, patients can develop hypoglycemia. Despite the recent advances in the self-monitoring of blood glucose (SMBG) at the point of care, glycemic control is unfortunately still a challenge for many diabetic patients^{4,5}.

As many as 67% of diabetic patients fail to monitor their blood glucose; citing finger soreness, pain, and inconvenience as the most common reasons for noncompliance⁶. To mitigate this issue, many researchers are working to develop non-invasive glucose sensors that possess the same level of accuracy as traditional blood-dependent measurement systems. The non-invasive

measurement of glucose may enable patients to conveniently check their glucose levels without the painful side effects of finger prick measurements.

It is important to note that type 1 and type 2 diabetic patients have different needs when it comes to how they choose to maintain glycemic control. Type 1 diabetes is caused by an absolute deficiency of insulin secretion whereas type 2 diabetes is caused by a combination of insulin resistance and inadequate insulin secretory response⁷. Therefore, most patients with type 1 diabetes rely on insulin injections in addition to monitoring their blood glucose levels. To ensure that glucose levels are within the normoglycemic range at all times, especially during insulin injections, continuous glucose monitoring systems (CGMs) are beneficial⁸. On the other hand, most type 2 and insulin-free diabetic patients do not require continuous monitoring of glucose levels. After performing informal interviews with 100+ stakeholders in the glucose biosensor market, including diabetic patients (type 1 and 2), ICU/NICU nurses, nursing home caretakers, and medical device companies, I found that most type 2 diabetic patients prefer to only check their blood glucose levels when they deviate from their diet or have not eaten regularly. According to the American Diabetes Association, at least three finger prick blood glucose measurement should be taken daily to maintain glycemic control⁹. From my findings, this number varies significantly across type 2 diabetic patients; from two times a day to once in two months, depending on whether they feel their blood glucose levels are well-controlled. Many patients mentioned that the inconvenience of finger-prick whole-blood sample collection prevents them from wanting to check more frequently, which was consistent with observations in previously published studies.

1.1.2 Advantages of non-invasive glucose detection

While CGM devices are extremely beneficial for the percentage of the diabetic patient population that requires continuous readouts to balance glucose and insulin concentrations, the larger percentage of the diabetic population (type 2 and insulin-free patients) and pre-diabetic individuals can benefit from a non-invasive, intermittent method of glucose detection. This will potentially encourage them to check glucose levels more regularly and ultimately improve glycemic control.

Blood glucose concentrations for a healthy person are within the range of 4.9 mmol/L to 6.9 mmol/L, which translates roughly to 80 to 120 mg/dL¹⁰. Glucose passively diffuses from the blood into other less-complex physiological fluids, including: interstitial fluid (ISF), sweat, tears,

aqueous humor, saliva, and exhaled breath condensate¹¹⁻¹⁶. Each of these fluids are associated with a specific glucose concentration range but not all are well correlated with blood glucose due to fluctuations in the glucose dilution factor and time-lag between changes in blood glucose and these other fluids^{17,18}.

1.1.3 Non-invasive glucose-containing sample matrices

ISF is well characterized and represents blood glucose values accurately but possesses a significant time delay that limits its application for real-time glucose measurements. For ISF measurements, the dynamic range of the sensor should be between 2-10 mM in order to cover hypoglycemic to hyperglycemic ranges. Devices like the GlucoWatch, which rely on transdermal mechanisms to electrochemically detect glucose in ISF, have had limited success because of environmental factors that affect sensor performance. Temperature fluctuations, excess perspiration, and mechanical shock can alter the electrolyte concentrations responsible for the sodium-glucose gradient¹⁹.

For sweat, tears, and the aqueous humor, it is unclear how the glucose concentrations rise during hyperglycemic episodes. Furthermore, the glucose concentrations vary greatly depending on physical activity and disease states (i.e., retinopathy can alter aqueous humor glucose concentrations). Saliva is the least reliable sample, as studies have proved that salivary glucose is easily altered by meal consumption and does not reflect true blood glucose values^{16,17}. Exhaled breath condensate originates from airway surface liquid, which maintains a rapid and stable glucose exchange with plasma. Thus, it is a promising candidate for non-invasive glucose detection.

1.2 Airway surface liquid (ASL) glucose

The thin layer of fluid covering the mucosa of the alveoli as well as both the small and large airways is interchangeably referred to as the airway surface liquid (ASL), alveolar lining fluid (ALF), epithelial lining fluid (ELF), and respiratory fluid (RF) in the literature²⁰⁻²². For simplicity, it will be referred to as ASL. This fluid serves numerous purposes and is the first layer of defense between the lungs and the outside world.

ASL in the conducting zone of the airway (from nose to proximal bronchioles) exists as a sol-gel compartment whereas in the respiratory zone of the airway (from distal bronchioles to

alveoli), it exists as a soluble layer to prevent collapse of alveoli²³. Nasal secretions of ASL do not normally contain glucose, but a study by Phillips *et al.*²⁴ found that glucose concentrations at 2-7 mM are present in nasal secretions during episodes of hyperglycemia and epithelial inflammation. However, nasal secretions are not necessarily representative of blood glucose concentrations due to the disturbance of normal glucose absorption across the epithelium during these episodes. As such, the composition of ASL is highly varied across the respiratory tract.

1.2.1 Regulation of glucose from blood into ASL

ASL in the respiratory zone of the lungs contains glucose concentrations that are ~12-fold lower than that of plasma glucose. Previous work by Baker *et al.* demonstrated that airway glucose homeostasis is regulated by facilitative glucose transporters (GLUT), which are present along the apical and basolateral membranes of airway epithelial cells, and tight junction proteins²⁵ (Figure 1.1). In healthy individuals, the abundance of tight junction proteins limits the paracellular diffusion of glucose from the lung interstitium into ASL. GLUTs not only allow passive diffusion of glucose from lung interstitium but also directly reduce glucose concentrations in ASL via intracellular uptake and metabolism to ensure that it is significantly lower than that of blood glucose^{25,26}. In the case of acute hyperglycemia and lung inflammation, this homeostasis is disturbed, and ASL glucose is significantly increased, despite the upregulation of GLUTs, due to compromised tight junctions. High, unregulated ASL glucose levels are directly linked to upper and lower respiratory bacterial loads²⁷. Thus, in diabetic patients, where ASL glucose concentrations are higher than those observed in non-diabetic individuals, there is an increased risk for respiratory bacterial infections if glucose homeostasis is not effectively achieved²⁸.

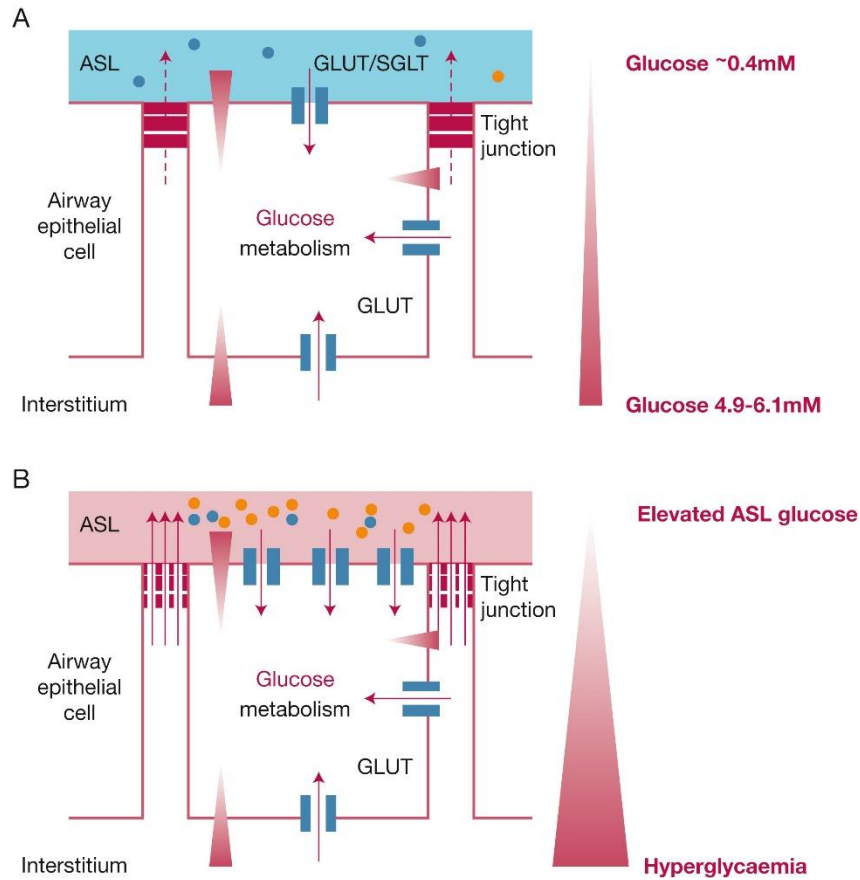


Figure 1.1. Airway glucose homeostasis.

(A) Airway surface liquid (ASL) glucose concentrations are normally ~ 12 times lower than that of blood concentrations; this is maintained by the tight junctions between the airway epithelial cells, which limit glucose influx, as well as by GLUTs on the apical and basal membranes that actively uptake and metabolize glucose; (B) During hyperglycemia, the gradient of glucose movement into ASL is increased. With airway inflammation, tight junction protein expression is reduced and allows an increased influx of glucose into the ASL. The upregulation of GLUTs is not enough to actively lower ASL glucose concentrations and thus the airway glucose homeostasis is disrupted. Reprinted from *CHEST*, **153**, E. H. Baker and D. L. Baines, Airway Glucose Homeostasis: A New Target in the Prevention and Treatment of Pulmonary Infection, 507-514, Copyright © 2018, with permission from Elsevier.

1.2.2 Transport of glucose from ASL into exhaled breath condensate (EBC)

ASL is secreted from the epithelial cell lining throughout the respiratory tract and is non-invasively collected in the form of exhaled breath condensate (EBC), which has previously been used as a non-invasive matrix to evaluate biomarkers of lung disease²⁹⁻³¹. The rate of respiratory droplet formation is dependent on the epithelial cell permeability in the various regions of the tract and the glucose transport from the alveoli. During turbulence in the airways caused by the

reopening of bronchioles and alveoli, non-volatile compounds in the ASL, such as glucose, undergo aerosolization^{32,33}.

Thus, when ASL is collected as EBC (via cooling of the air exhaled by a subject), it is greatly diluted by water vapor as it travels from the respiratory zone to the conducting zone. While EBC glucose is assumed to have a theoretical dilution factor from plasma glucose of 1:10000^{16,34}, the variable nature of water vapor dilution and droplet aerosolization has resulted in reported EBC glucose concentrations varying significantly from 0.24-5.5 μM ³⁴⁻³⁸.

1.2.3 Effect of diabetes and lung-related co-morbidities

Previous studies have shown that patients with lung-related diseases such as chronic obstructive pulmonary disease (COPD) or cystic fibrosis (CF) have altered glucose concentrations in EBC^{16,33,39,40}. A study by Baker *et al.* concluded that CF patients have elevated ASL glucose levels compared to diabetic patients without any lung-related ailments. Compared to both CF and diabetic patient groups, patients with CF-related diabetes had significantly higher concentrations of glucose in EBC. In other studies, while EBC itself wasn't sampled, it was found that in other airway samples (nasal lavage fluid, sputum, bronchoalveolar lavage fluid) from patients with COPD, ASL glucose concentrations were higher than those of healthy subjects^{41,42}. This means that lung-related comorbidities may influence the reliability of using ASL derived glucose measurements as an alternative to blood glucose measurements unless a reliable model for glucose airway homeostasis is established for diabetic and non-diabetic individuals.

1.3 Collection of EBC

The appeal of using EBC as a sample for biomarker detection and biomolecule analysis is its non-invasive collection method. Compared to bronchoalveolar and nasal lavage, EBC collection samples a much larger area of the lung and does not alter the physiology of the respiratory tract lining⁴³. Despite this ease of accessibility, there are several physiologic and environmental factors affecting EBC glucose concentrations that must be considered and controlled for during collection.

Most commercially-available devices for EBC collection, such as R-Tube and EcoScreen, rapidly cool the exhalate so that aerosol particles can adhere to cooled surfaces such as silicone or

Teflon^{44,45}. In a typical procedure, a subject breathes into a collection tube that is maintained at a much lower temperature than ambient air (between 5-10 °C). Cooling is normally achieved via an ice bath or dry ice immersion of the collection surface prior to collection (Figure 1.2). This allows the aerosolized droplets of exhaled air to condense into a liquid that can be collected and analyzed.

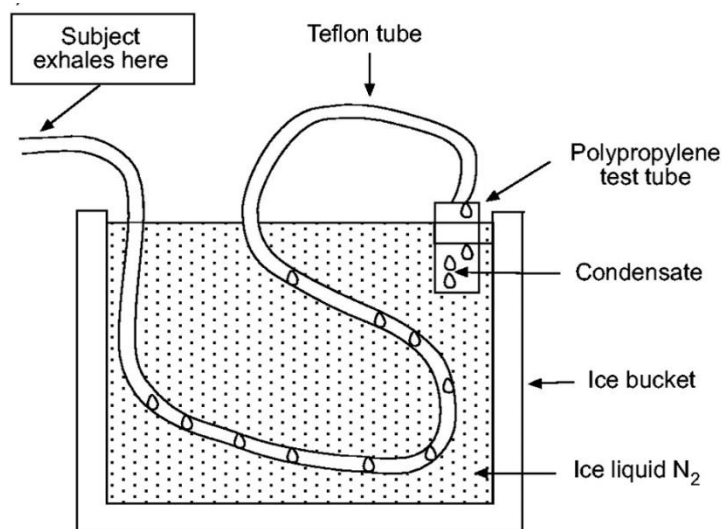


Figure 1.2. Method of condensing exhaled breath.

Reprinted with permission of the American Thoracic Society. Copyright © 2020 American Thoracic Society. All rights reserved. G. M. Mutlu, *et al.*/2001/Collection and Analysis of Exhaled Breath Condensate in Humans/*Journal of Respiratory and Critical Care Medicine*/164/731-737. The American Journal of Respiratory and Critical Care Medicine is an official journal of the American Thoracic Society.

1.3.1 Variable dilution factors

A major issue affecting the reliability of EBC glucose measurements is the variable dilution factors due to water vapor when ASL is collected as EBC. While ASL is secreted throughout the epithelial cell lining of the respiratory tract, it is aerosolized and diluted by droplets of water vapor as it travels from the lower airways to the mouth. Thus, all non-volatile solutes, such as glucose, are diluted to a certain degree by water vapor when they are collected in EBC. This makes it challenging to determine whether changes in reported EBC glucose concentrations reflect fluctuations in water vapor droplet formation or the concentration changes of glucose in the fluid lining³⁴. A possible explanation for the large variability in dilution factors of EBC is the inclusion of anatomical dead space air in the condensed exhaled air sample. Anatomical dead space is the

portion of air from the upper respiratory tract (mouth, nose, trachea), that does not participate in gas exchange and thus does not contain solutes of clinical relevance from the alveolar epithelial lining⁴⁶. Therefore, the inclusion of ASL from the dead space air in EBC can dilute solute concentrations to levels that are below the limit of detection for many assays. Recent devices such as the EcoScreen 2 have been developed to separate alveolar air from dead space air by discarding the first 50 mL of each breath cycle⁴⁷. However, this threshold volume may not accurately estimate the dead space volume, which can fluctuate between breaths and can vary across subjects. The inconsistency in collection methods and lack of standardization for separating alveolar analytes from dead space air have contributed to the wide range in experimental blood-to-breath glucose ratios (anywhere from 1000:1 to 50,000:1)³⁴.

1.3.2 Surface materials for condensation and collection

The material chosen for droplet condensation and collection should be sufficiently hydrophobic to allow for ease of droplet flow while also not trapping small molecules or proteins on its surface. Fouling of the collection surface with biomolecules can affect the concentration of glucose in the sample if residual glucose remains on the collection surface. Any material used in collection surfaces should also be tested to ensure it does not leach or contaminate the EBC sample as certain surfactant adhesive properties may affect the concentration of biomarkers and small molecules collected. Copper, for example, has been shown to leach into EBC samples; since it is also a highly reactive material⁴⁸.

The current devices on the market for EBC collection, EcoScreen and R-Tube, use different materials for trapping and cooling EBC. The R-Tube uses a polypropylene tubing with an outer aluminum cooling sleeve to collect EBC and the coating material for EcoScreen is very similar to Teflon. Although not tested on R-Tube and EcoScreen specifically, one study analyzed the interaction effects of four different collection materials on glucose measurements and found that Teflon had the least impact on glucose solutions, making it the most appropriate material for glucose collection⁴⁹.

Furthermore, a larger surface area may allow for increased interaction and cooling to enable droplet formation and condensation. However, too large of surface area can hinder collection of the condensate if the droplets cannot coalesce. Therefore, an optimal design for

condensation and collection should allow enough surface area for droplet formation but in a smaller geometry that can allow for droplet coagulation and collection.

1.3.3 Salivary contamination in EBC

Salivary contamination is an issue when collecting EBC, as studies have shown that salivary glucose does not accurately represent blood glucose^{15,16,50-52}. To combat salivary contamination, individuals should rinse their mouth thoroughly prior to exhalation into the collection device because certain food or drinks present in saliva may affect the concentration of glucose as well as other analytes. The device should also incorporate a saliva trap and subject should swallow periodically to avoid excess saliva from escaping the saliva trap. Because amylase is found only in the saliva and not the rest of the respiratory circuit, some studies have assayed the concentration of amylase in the saliva as well as EBC collected to determine the extent of salivary contamination in EBC. If the amylase concentration in EBC is at least 10-fold lower than that of the saliva, then salivary contamination is considered minimal^{39,53}.

1.4 Glucose detection methods for EBC

In addition to proper controls and standardized methods for collecting EBC, several design and performance criteria are required for accurate and rapid sensing of glucose at these low concentrations. Most of the previously published studies on EBC glucose detection use small molecule detection instruments to quantify glucose concentration. In contrast to chromatography-based laboratory instruments, biosensors are more suitable for rapid, point-of-care glucose detection.

1.4.1 Biosensor specifications

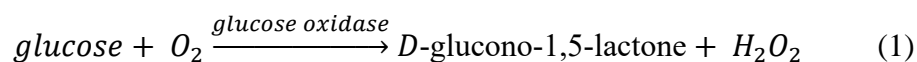
Glucose biosensors currently make up 85% of the global biosensor market, which is worth approximately \$11.5 billion USD⁵⁴. A biosensor is an analytical device that incorporates biologically-derived recognition elements to detect analytes through a physiochemical transducer⁵⁵. The main components of a biosensor include: the analyte (glucose), a bioreceptor or recognition element, and a transducer, which converts the biorecognition element into a measurable signal. There are many different molecular recognition elements but those commonly

used in glucose biosensors are protein-based, including enzymes, binding proteins, and lectins⁵⁶. The type of recognition element is determined by the type of physiological sample and signal of interest. Transduction mechanisms for glucose biosensors typically include electrochemical detection, fluorescence intensity measurements, and surface plasmon resonance, among others.

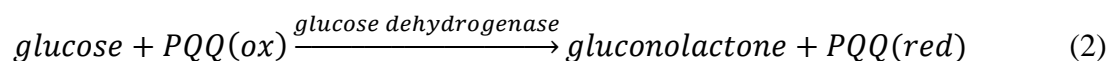
Certain recognition elements and transduction mechanisms are promising for low-concentration glucose detection. For successful application in exhaled breath condensate, the limit of detection of a glucose biosensor should be at the sub-micromolar level. The dynamic range should cover normal and hyperglycemic ranges for all literature values: ideally between 0.2 μM and 2 mM. Because the differentiation between normal and hyperglycemic ranges are reported to be at the sub-micromolar range for some studies, the resolution should be 0.1 μM or smaller³⁸.

1.4.2 Protein-based enzymatic glucose recognition elements

The most widely used method for glucose detection is based on the interaction of the analyte with glucose-specific enzymes. Glucose oxidase (GOx) and glucose dehydrogenase (GDH) are the two enzymes used in monitoring blood glucose. GOx has been shown to have high selectivity for glucose in blood and other fluids such as interstitial fluid, tears, sweat, and saliva⁵⁷⁻⁶⁰. GOx catalyzes the oxidation of β -D-glucose into D-glucono-1,5-lactone using molecular oxygen as an electron acceptor⁶¹. Hydrogen peroxide is a byproduct of this enzymatic reaction (Eq. 1).



While GOx is the gold standard of glucose sensing due to its high stability, it uses molecular oxygen as the primary electron acceptor and is unable to transfer electrons efficiently to electrode surfaces^{62,63}. GDH combined with redox cofactors to transfer electrons to electrode surfaces is an alternative to GOx-based biosensors. GDHs are further categorized according to redox cofactors used, which act as primary electron acceptors. Cofactors used with GDH include nicotine adenine dinucleotide (NAD), nicotine adenine dinucleotide phosphate (NADP), and pyrroloquinoline quinone (PQQ)⁶⁴ (Eq. 2).



Traditionally, the enzyme of choice is immobilized on a surface which interacts with the biological sample of interest^{54,65,66}. Enzyme-based glucose biosensors are commonly quantified using an electrochemical (amperometric) sensing modality. The presence of a redox center in the enzyme and the mechanism of electron transfer make electrochemical or amperometric detection the most popular application for GOx and GDH enzymes⁶⁶. Originally introduced by Clark and Lyons for use in glucose monitoring, first generation glucose biosensors used molecular oxygen as the primary electron acceptor in an enzyme-catalyzed (GOx) glucose reaction, and glucose concentration was amperometrically determined by monitoring either the decrease in oxygen or the production of hydrogen peroxide^{67,68}. GOx and GDH have similar affinities for glucose ($K_m=14.6$ mM and 10 mM, respectively) and are stable in a wide range of concentrations⁶⁹⁻⁷¹.

Modifications to GOx and GDH-based electrochemical sensors have been made to achieve the low limit of detection and reasonable resolution required for non-invasive fluids with sub-micromolar glucose concentrations. Two studies from the Ren group have demonstrated GOx-based electrochemical glucose sensing for application in EBC^{72,73}. These studies used zinc oxide (ZnO)-functionalized high electron mobility transistors (HEMTs) to immobilize GOx for electrochemical glucose detection. Using the changes of drain current as a function of glucose concentration, a linear range of 0.5 nM to 14.5 μ M with a limit of detection of 0.5 nM was achieved⁷².

Neither study tested the sensor on collected EBC samples from human subjects but the second study by Chu *et al.* integrated the sensor into a condensing unit comprising of a Peltier (thermoelectric) cooler to demonstrate condensation of an aerosolized solution and direct detection of glucose from the condensed sample. They found that only 3 μ L of condensed sample was required to cover the sensing area, which took less than 2 seconds to form when the temperature of the cooling surface was maintained at 7 °C⁷³. While this device was able to attain low detection limits and a physiologically relevant linear range, the high dependence on pH and temperature for enzymatic activity limits its ability to produce robust and reproducible measurements under physiological conditions⁷³.

In an effort to overcome some of the drawbacks associated with non-invasive electrochemical glucose detection, researchers have used enzyme-based elements with fluorescence, surface plasmon resonance, and colorimetry⁷⁴⁻⁷⁸. Due to the higher glucose

selectivity and stability of GOx over GDH, most studies for non-invasive glucose detection at low concentrations use GOx as the recognition element. Apart from organic fluorophores and luminescent probes such as ruthenium and platinum, some studies have used quantum dots to achieve higher sensitivity with GOx-based glucose detection. Quantum dots (QDs) are inorganic, semiconducting nanocrystals which have well-defined energy levels and are used in a wide range of applications. Unlike organic dyes, which operate over a limited range of colors and are susceptible to photobleaching, QDs are significantly brighter, more photostable, and can be tuned to produce any color of visible light. They have been employed in enzyme-based glucose biosensors that have achieved micromolar and sub-micromolar detection limits *in vitro*⁷⁸⁻⁸¹.

The most successful study was done by Cao *et al.* in which a complex consisting of CdTe QDs bound by four GOx structures was developed⁸². When glucose was introduced to the complex, the GOx would produce hydrogen peroxide that quenched the QDs in a proportional manner to the amount of glucose detected. The hydrogen peroxide was immediately reduced to oxygen when the electron transfer occurred on the surface of the QDs. The oxygen is then stored in electron hole traps on the QDs and can be used as an acceptor for future GOx reactions; this allows for greater temporal resolution. The complex exhibited better thermal stability compared to native GOx as it was stable between 20-80 °C and had maximum activity in the 40-50 °C range. A linear range of 5 µM to 1 mM was demonstrated along with an experimental detection limit of 0.1 µM⁷⁸. However, the sensor able to achieve the desired detection limit and linear detection range only under optimized pH conditions.

Although significant work has been done in developing enzyme-based sensors for non-invasive glucose detection, few studies have demonstrated sub-micromolar sensitivity and detection ranges suitable for EBC^{75,76,83}. The inherently high Michaelis-Menten constant of GOx ($K_m = 3.5-38$ mM) prevents it from being suitable for sub-micromolar detection unless expensive modifications are made for signal amplification⁷¹. Furthermore, the enzymatic activity of GOx is greatly dependent on pH and temperature – both of which can fluctuate greatly in physiological conditions. In addition, byproducts such as hydrogen peroxide and gluconic acid (hydrolyzed form of D-glucono-1,5-lactone) can deactivate the enzyme, affect the stability of electrodes when used in electrochemical detection, and ultimately reduce the shelf-life of the device^{73,84,85}. The presence of baseline hydrogen peroxide in normal EBC samples may limit the accuracy of enzymatic sensors that rely on glucose quantification through the production of hydrogen peroxide. Thus,

recognition elements that are highly stable, lack byproducts, and possess inherently higher affinity for glucose may be more suitable for detection in EBC.

1.4.3 Protein-based non-enzymatic glucose recognition elements

The glucose binding protein (GBP) is a periplasmic binding protein found in Gram negative bacteria. It is natively expressed in the periplasmic space of *E. coli*, which makes it an easily acquirable recognition element. This protein undergoes a conformational change from “open” to “closed” upon binding with glucose (Figure 1.3).

Due to its high affinity for glucose ($K_D=0.35 \mu\text{M}$), it has been used in glucose sensors to detect concentrations at the μM range without much modification or signal amplification, which is a significant advantage over other recognition elements. Unlike enzymatic recognition elements, GBP does not alter the chemistry of glucose with its conformational changes. Because it does not possess electron transfer capabilities, fluorescent detection is the sensing modality used for this protein. The Daunert group has previously engineered the GBP with fluorescently labeled amino acid residues near the binding site. The fluorescent quenching was demonstrated to be proportional to the concentration of glucose and the limit of detection for one mutant GBP was reported to be $0.05 \mu\text{M}$, which is well-suited for detection at EBC glucose concentrations⁸⁶.

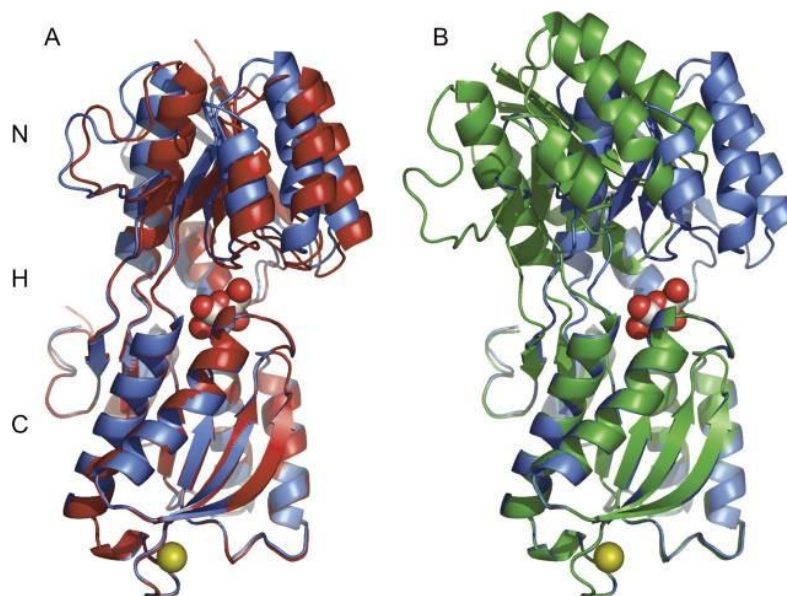


Figure 1.3. Overall structures of GBP.

The GBP structure (blue ribbon) bound to glucose (red oxygen and gray carbon spheres) and calcium ion (gold sphere) with the previously solved *E. coli* glucose-bound structure (red ribbon). The N- and C-terminal domains as well as the three-segment hinge (H) that connects them are labeled. (B) The superposition of the C-terminal domains of the glucose-bound (blue) and open resolution (green) GBP structures reveals the 31 ° hinge opening movement. Source: M. J. Borrok, L. L. Kiessling, and K. T. Forest. (2007), Conformational changes of glucose/galactose-binding protein illuminated by open, unliganded, and ultra-high-resolution ligand-bound structures. *Protein Science*. **16(6)**. John Wiley and Sons, p. 1032-1041, figure 2. Reproduced with permission from John Wiley and Sons. Copyright © 2007 The Protein Society

A common method used for fluorescent glucose detection with GBP is Förster resonance energy transfer (FRET), in which the distance between the donor and acceptor molecules determines the rate of energy transfer. Many of the studies published on FRET-based glucose detection with GBP have wide-ranging reported sensitivity values. This is due to the variable positioning of fluorescent labels on GBP and the types of fluorescent dyes used. Furthermore, FRET based on the conformational change of GBP results in insufficient fluorescence intensity changes due to the limited range of motion of the N-terminus with respect to the protein domains upon glucose binding⁸⁷. To address this, Hsieh *et al.* developed a dual-labeled GBP sensor with an environment-sensitive fluorophore, nitrobenzoxadiazole (NBD) on the outer surface of the binding pocket and a Texas Red (TR) fluorophore on the inner surface of the binding site⁸⁸. Ratiometric measurement of the two molecules was used to determine fluorescence response curves; glucose was detectable in the millimolar range (1-30 mM) with an apparent K_D of 1.7 mM. While this

method improved the fluorescent intensity changes in FRET by avoiding the dual-terminal labeling of the protein, the sensitivity was significantly compromised⁸⁸.

Concanavalin A (ConA) is another popular molecular recognition element for fluorescence-based glucose detection. It is a plant-derived lectin, which is a family of proteins with strong binding affinities for glycans due to their multivalent interactions⁵⁶. It contains four binding sites for glucose and competitively binds to glucose in biosensor schemes. Typically, ConA is bound to an existing labeled carbohydrate derivative such as dextran but is displaced from the molecule when glucose preferentially binds to it. ConA has been extensively studied in various sensing schemes involving different combinations of fluorophores and fluorescent particles^{89–93}. Most of these systems demonstrate a linear detection range of sub-micromolar to 25 mM of glucose, but with varied response times depending on the type of sensor. However, ConA has exhibited problems with aggregation and leakage, limiting its performance in physiological conditions. This can be especially problematic in low-concentration glucose samples such as EBC.

1.5 Thesis overview: selective EBC collection and competitive fluorescent biosensor for non-invasive glucose detection

EBC is a promising non-invasive sample for glucose monitoring purposes due to its origination from ASL, which maintains a tightly regulated glucose exchange with blood. However, as discussed in **1.3 Collection of EBC**, methods used to collect EBC are highly inconsistent. The variable dilution factors associated with water vapor and the inclusion of dead space significantly impact the reliability of the theoretical glucose dilution between blood and EBC (1000:1 to 50000:1). Because anatomical dead space does not participate in gas exchange and does not contain glucose, its inclusion when condensing exhaled air further dilutes the EBC sample.

Furthermore, the large range in reported EBC glucose concentrations calls for a robust and highly sensitive detection system that can resolve sub-micromolar concentration changes. Many studies examining EBC glucose use bulky chromatography-based small molecule detection systems that are not suitable for point-of-care detection. As discussed in **1.4 Glucose detection methods for EBC**, glucose biosensors using various recognition elements and transduction mechanisms have shown promise in recent years for sub-micromolar sensitivity. However, not all

are stable in physiological conditions due to high dependence on pH and temperature, degradation from enzymatic byproducts, and aggregation effects.

The *E. coli* glucose binding protein (GBP) has a stronger and more specific affinity to glucose ($K_D=0.35 \mu\text{M}$) compared to that of GOx ($K_m=14.6 \text{ mM}$) and ConA ($K_D=2.5 \text{ mM}$)^{70,71}. Fluorescence is the most versatile transduction mechanism because it provides single molecule sensitivity, and high dynamic, temporal, and spatial resolution⁹⁴. Thus, GBP can be harnessed as a fluorescent biosensor for glucose detection at the sub-micromolar level.

Together, a non-invasive glucose monitoring system for EBC should incorporate 1) a standardized EBC collection method that accounts for variable dilution factors due to water vapor and dead space air; and 2) a robust, non-enzymatic fluorescent biosensor with high glucose affinity that can achieve the sensitivity and resolution required to distinguish sub-micromolar glucose changes in EBC.

In **Chapter 2**, I develop a method to selectively collect exhaled air from the deep lung circuit using a temperature-based separation of dead space air. I characterize the impact of the selective temperature threshold on the volume of collected condensate and corresponding glucose concentration through IRB-approved feasibility studies involving human subjects. For ease-of-use and portability, I implement effective valving mechanisms and collection design and compare the performance of my condenser to commercially available EBC collection platforms. In **Chapter 3**, I investigate the change in EBC glucose (from selectively collected condensate) with respect to the rise and fall of blood glucose through a pilot study of oral glucose tolerance test trials conducted on normoglycemic and type 2 diabetic subjects.

Conjugation of protein to fluorescent probes traditionally require extensive purification steps and the incorporation of a functional tag. In **Chapter 4**, I take advantage of bio-orthogonal labeling to engineer the GBP with an N-terminal chemo-enzymatic azide tag from within the *E. coli* expression system. I characterize the incorporation and selective conjugation efficiency of this tag through azide-alkyne cycloaddition reactions directly from cell lysate. A drawback to the currently reported fluorescence-based GBP sensors is the use of organic fluorophores which are susceptible to photo-bleaching, pH dependence, and narrow excitation spectra^{11,95}. In order to develop a robust GBP-based fluorescent biosensor, a highly photo-stable nanomaterial with limited pH/temperature dependence is required. In **Chapter 5**, I conjugate azide-labeled GBP to

functionalized quantum dots (QDs). QDs were chosen due to their high photostability, resistance to pH and temperature fluctuations, and large Stoke's shift owing to broad excitation spectra and narrow, tunable emission spectra.

Lastly, in **Chapter 6**, I take advantage of the large Stoke's shift of QDs to develop a FRET-based glucose detection system. The competitive binding of GBP to glucose and galactose motivated the incorporation of a fluorescently labeled galactosamine acceptor molecule, which would quench the QD emission upon GBP ligand binding. I characterize the optimal molar ratio of the acceptor (ligand acceptor) to donor (GBP-QD) that would permit highly sensitive FRET signals indicative of competitive glucose binding. These studies provide the basis for further characterization of the GBP-QD-ligand system, including binding kinetics, dynamic and temporal resolution, and detection performance (limit of detection, sensitivity) in physiological EBC samples.

2. DEVELOPMENT OF AUTOMATED CONDENSER FOR SELECTIVE COLLECTION OF RESPIRATORY ZONE EBC

Parts of this chapter are reprinted, with permission from D Tankasala *et al.*, “Selective collection and condensation of exhaled breath for glucose detection”, *Conf Proc IEEE Eng Med Biol Soc*, July 2018. Copyright © 2018 IEEE⁹⁶.

2.1 Rationale

To minimize the variability in reported glucose concentration in EBC due to the inclusion of dead space air, a selective collection system was developed to condense only deep-lung (alveolar) air. By eliminating dead-space air from EBC collection, the concentration of non-volatile solutes will be less dilute. There is no diffusion occurring between the epithelial cells and plasma in the dead space region, which means that there is no dependence on an ionic gradient to propel the gas exchange between oxygen and carbon dioxide⁹⁷.

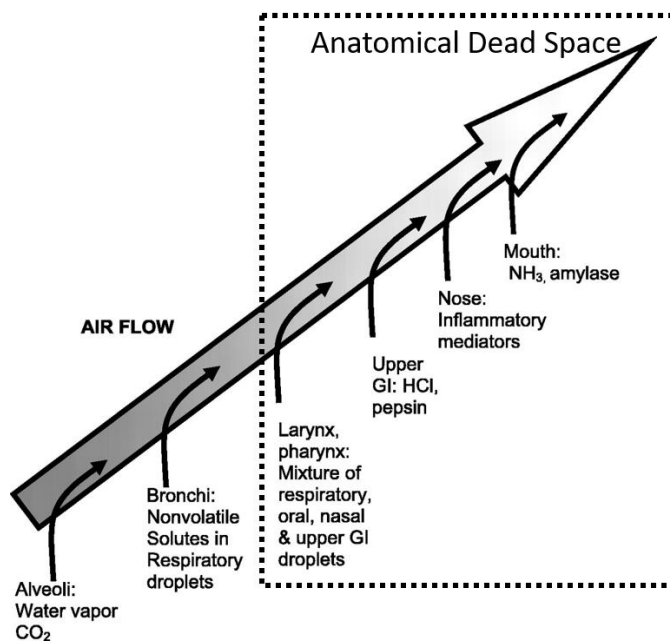


Figure 2.1. Components of exhaled air from various regions of respiratory tract.

The box indicates the anatomical dead space of the airway tract, which does not contain solutes of interest. The respiratory zone contains the alveoli and proximal bronchi, which participate in gas exchange and contain non-volatile solutes of interest, such as glucose. Reprinted (adapted) with permission from The American Physiological Society. Source: R. M. Effros, M. B.

Dunning, J. Biller, and R. Shaker, *American Journal of Physiology: Lung Cellular and Molecular Physiology*, 2004, **287**(6), p. 1073-1080, figure 2. Copyright © 2004 The American Physiological Society.

Therefore, the elimination of dead space air is necessary to minimize variable dilution factors. Other parameters to control include the subject's rate of breathing and the total volume air exhaled and collected into the device. Figure 2.2 shows how a selective valve mechanism can be used to separate dead space air from deep lung air.

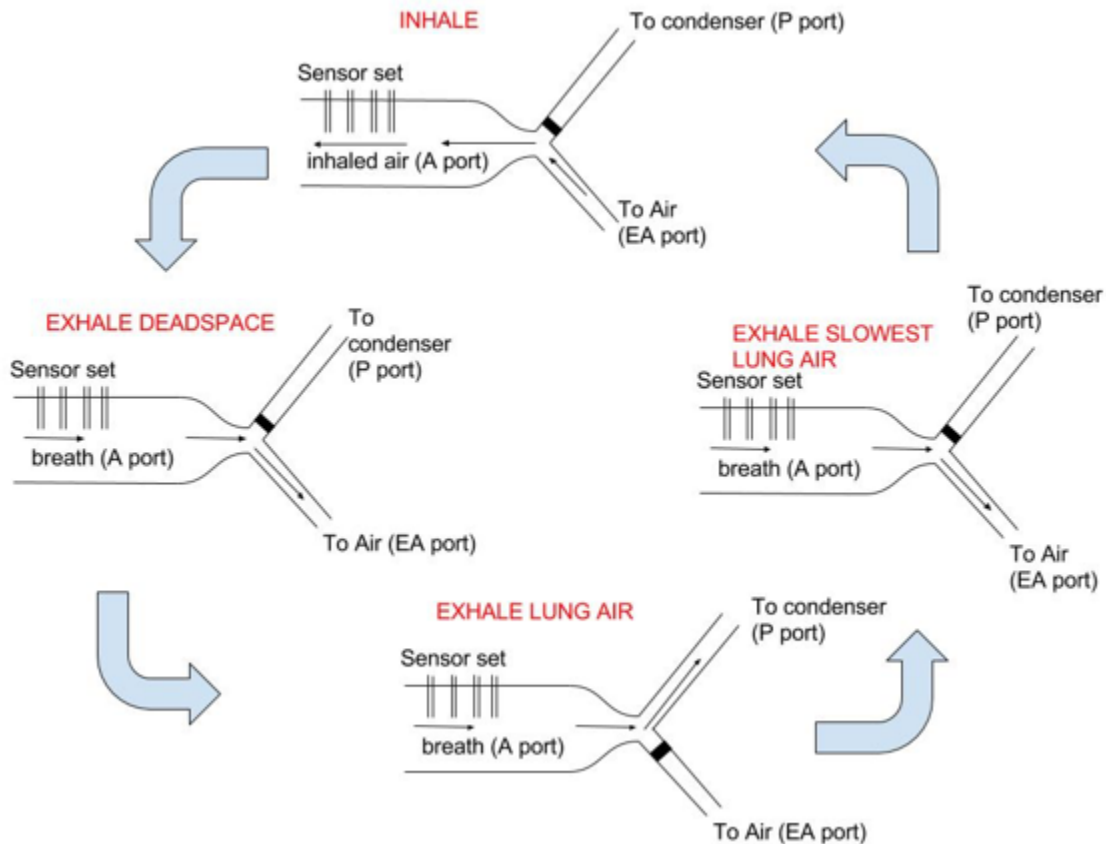


Figure 2.2. Diagram of selective valve opening and closing for capturing deep lung air and exclusion of anatomical dead space air.

The initial period of exhalation characterized as dead space air must be removed to collect EBC that contains a large fraction of respiratory fluid. During a normal exhalation period, the transition from dead space air to deep lung air is characterized by a rise in CO₂ levels (Figure 2.3)⁹⁸. Previously, Schubert *et al.* had demonstrated that it was possible to sample alveolar gas in mechanically ventilated patients using a CO₂-controlled sampling method to separate dead space gas from alveolar gas⁹⁹. Furthermore, the average temperature of exhaled breath is 37 °C and for inhalation, the temperature is found to be 20 °C; this difference was used to distinguish between inhalation and exhalation. Rather than using an expensive end-tidal CO₂ (EtCO₂) sensor, I

developed a system using an analog windspeed and temperature sensor to use a threshold to identify deep lung air.

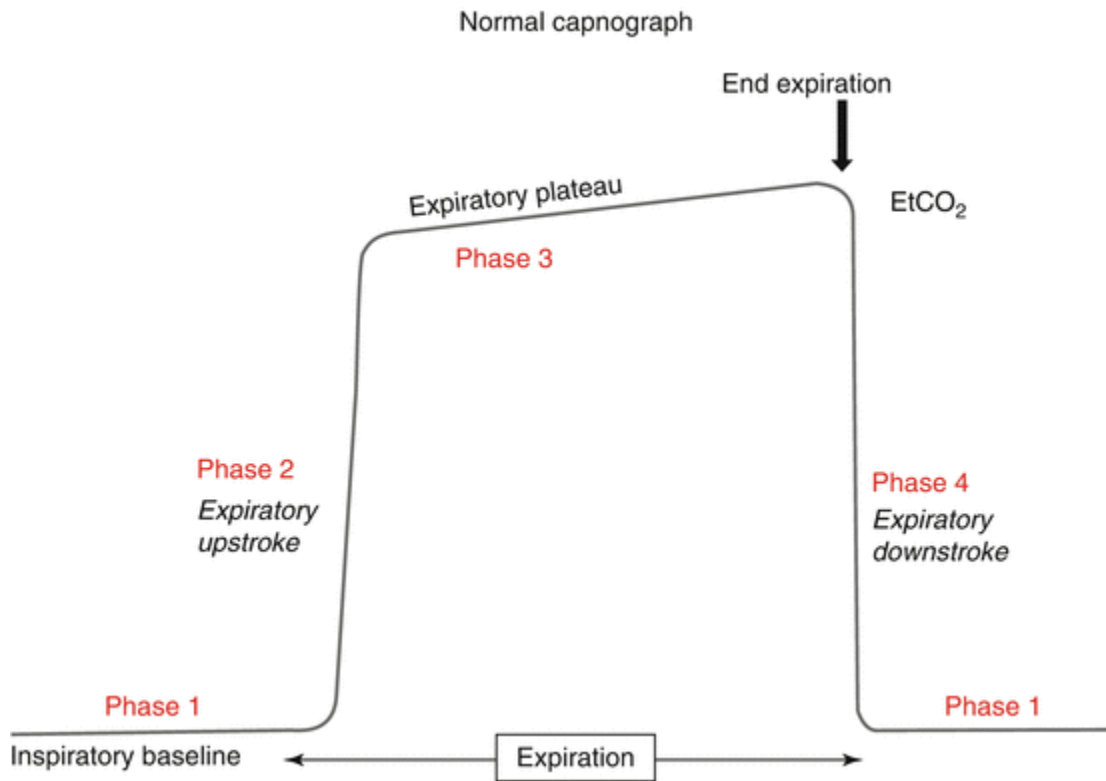


Figure 2.3. Capnography diagram depicting the phases of expiratory CO₂ content.

Phase I: exhalation of CO₂ free gas from dead space; phase II: combination of dead space and alveolar gas; phase III: exhalation of mostly alveolar gas; phase IV: inhalation of CO₂ free gas. Reprinted by permission from Springer Nature: Springer, *Data Interpretation in Anesthesia* by R. Ganta and T. D. Raj, Copyright © Springer International Publishing AG 2017

2.2 Materials and Methods

2.2.1 Time-based selective EBC collection using solenoid valve

Time-based threshold selection

The Rev. C Wind Sensor (Modern Devices, RI, USA) was chosen because of its low-cost, compact design and excellent sensitivity and temporal resolution. It contains temperature and wind-speed pins that output a voltage based on the temperature and speed of passing air. An Arduino Pro Mini microcontroller (5V) was used to convert voltages from the sensor to digital values. The code uses the trapezoid rule to calculate the volume of exhaled air passing through the

sensor pins. The area under the curve of the volumetric flow rate (based on the cross-sectional area of the tube in which the sensor is placed) is summed across the duration of the breathing period to calculate the total exhaled volume. The data is then recorded into arrays along with time throughout the period in which the valve is opened. The temperature pin voltages were calibrated against thermocouple measurements.

To determine the time-based ratio of dead space air to total exhale air, I analyzed published capnographs of healthy individuals as I did not have access to an end-tidal capnometer. The middle of expiratory upstroke (Figure 2.3) was used as the starting point of the exhalation (T_s) the end of the transition phase was designated as the start of deep lung air exhalation (T_t), and the end of the plateau phase was used as the end of the exhalation (T_e). Dead space time was then defined as $T_t - T_s$ and the total exhaled time was defined as $T_e - T_s$. Equation (3) shows the ratio of dead space to total exhalation time This ratio was applied to each exhalation to identify the start of deep lung air exhalation.

$$\frac{T_t - T_s}{T_e - T_s} \quad (3)$$

The time ratios were calculated for 16 healthy individuals (ages 1-74 years) based on their capnograms (from CapnoBase.org) and assessed for normal distribution¹⁰⁰. Complete subject data can be found in Table A.1. Analysis determined that the average ratio of dead space to total exhalation time is 0.31 ± 0.12 , which translated to a time-based threshold of 31% with an upper bound of 43%. The upper bound was used as a time threshold in the Arduino code to enable a stricter selection criterion across all subjects.

In the Arduino code, the first three breaths were used to calibrate the average time for an exhalation profile (determined by higher temperature ranges than the inhalation period). Then, the average time was multiplied by 43% to determine the average time point at which the selective valve should allow collection of the exhaled air. The point at which expiratory flow rate starts to slow down (based on volumetric flow rate data obtained from the windspeed sensor) was used to control valve closure.

Valve mechanism and collection body design

A pneumatically actuated 3-way 2 position electric solenoid assembly (US. Solid, OH, USA) was fitted onto a Y-shaped connector (two inlet ports, one outlet). On one inlet of the tube, the windspeed and temperature sensor was inserted cross-sectionally. The other inlet was fitted with a check valve to prevent back-flow of inhaled air. The outlet of the solenoid valve was connected to the inlet port of an octagonal (10 mm and 25 mm edges) aluminum condensation surface that had an additional 25 37 mm x 0.4 mm “fins” for increased surface area (2760 mm²) (Figure A.1).

To effectively cool exhaled breath into condensate, I used a Peltier cooler (40 mm x 40 mm, SparkFun Electronics, CO, USA), a thermoelectric cooler that creates a temperature differential by removing heat from its cooler surface to the hotter surface when a voltage is applied across it. When a heat sink mechanism (heat sink and fan) is attached to the hot side, the temperature differential allows the cold side to reach temperatures of down to -10 °C. The aluminum condensation surface was attached to the cold side of the Peltier assembly via thermal adhesive for condensate formation. The outlet port of the condensation surface was connected to clear (1 cm inner diameter) tubing for collection of EBC.

The temperature and windspeed sensor, solenoid valve, and Peltier cooler were connected to a 5 V Arduino Pro Mini microcontroller and an additional 12 V power source was used to operate the solenoid valve. A printed circuit board (PCB) was designed to seamlessly integrate the electrical components with the microcontroller (OSH Park, OR, USA). Details of the PCB schematic can be found in Figure A.2. The entire assembly, including the condensation plate, tubing, and heat sink, was held together by two sets of C-clamps on a ring stand (Figure 2.4).

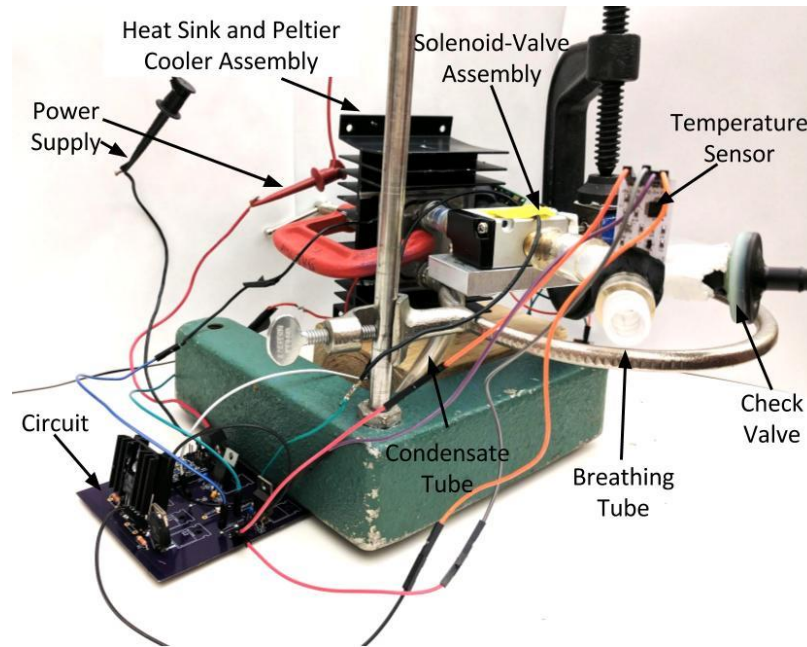


Figure 2.4. Front view of condenser prototype pictured with PCB circuit, Rev. C wind sensor, breathing tube, heat sink/Peltier cooler assembly, and solenoid valve.

Comparison with CO₂ profile of exhaled breath

To compare the time-series of valve action (open and close) with the temperature and CO₂ profile of exhaled breath, I incorporated a CO₂ sensor (SprintIR, CO₂ Meter Inc., FL, USA) into the device, powered by a separate Arduino Uno microcontroller (Figure 2.5). The sensor was connected to a secondary outlet from the solenoid valve (8 inches from the temperature windspeed sensor). A binary output of valve actuation (1 – open; 0 – closed), temperature, volumetric flow rate, and CO₂ profile of exhaled breath was recorded for one subject. The time series were overlaid to determine whether selective valve actuation based on a time-based approach captured exhalate at peak CO₂ levels.

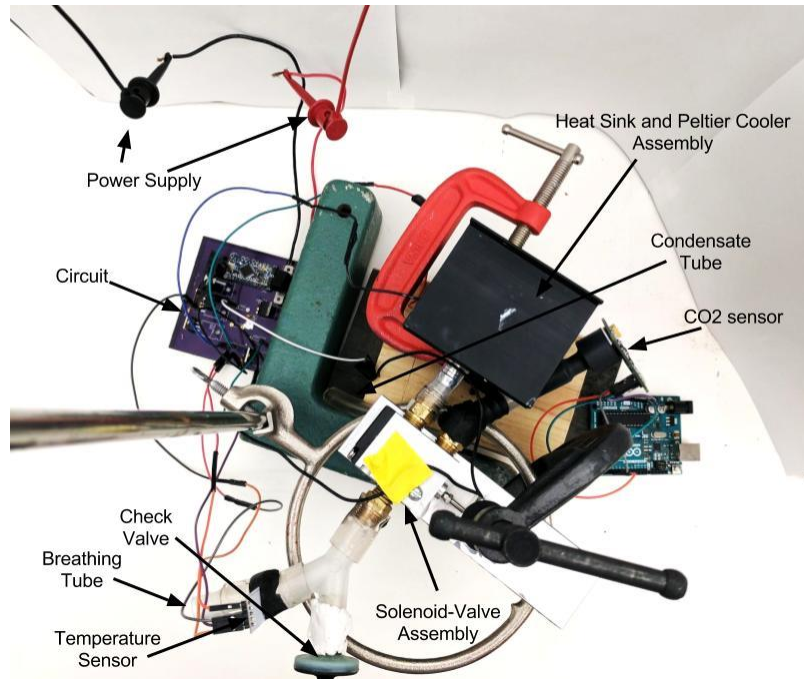


Figure 2.5. Top view of condenser prototype with embedded CO₂ sensor.

Device feasibility studies for EBC collection

A set of feasibility studies using this device was performed on human subjects to determine whether it can consistently collect reproducible volumes of EBC from fixed total expiratory volumes. EBC samples were analyzed for glucose concentration and compared with finger-prick blood glucose measurements to determine dilution factors between blood and EBC glucose at baseline concentrations.

Four healthy normoglycemic subjects with no history of lung-related ailments or diabetes (ages 22-25, female) were recruited for the study and all gave written consent to the experimental procedures, which had been approved by Purdue University's Institutional Review Board. Subjects were asked to fast at least two hours prior to sample collection. Subjects were provided sterilized disposable mouthpieces and optional nose clips and were instructed to breathe into the device (inhale and exhale through the mouth) for 4 ½ minutes. Immediately after collection, a finger prick sample of blood glucose was measured via a glucometer (Roche Diagnostics, IN, USA). The condensate sample on the aluminum finned surface was collected via micropipette and stored in microcentrifuge tubes at -20 °C until further analysis. The condensate plate was rinsed with DI water and dried in between each collection period. A total of 8 collection periods were taken for each subject that included EBC collection and blood glucose measurement. The total expiratory

volume was recorded by the Arduino program, along with the temperature measurement and valve actuation data. Samples were then analyzed for total EBC volume and glucose concentration. The expiratory volume required to produce a minimum condensate volume of 100 μL was calculated for each sample and assessed for variance using One-way ANOVA. A commercial fluorometric glucose oxidase assay (Abnova, Taipei, Taiwan) was used to quantify glucose concentrations. Fluorescence was measured using the SpectraMax M5 Microplate Reader (Molecular Devices, CA, USA) at ex./em. 540 nm/590 nm. Blood glucose concentrations were converted to micromolar units and divided by corresponding EBC glucose concentrations to determine blood to EBC glucose dilution factor. One-way ANOVA was used to analyze significant differences

2.2.2 Temperature-based selective EBC collection using balloon valve

In the second iteration of this selective condenser, I based valve actuation off the actual temperature profile of the exhaled breath, which is better adapted to fluctuations in the user's breathing profile. The solenoid valve in the previous iteration of the device increased breathing resistance for the user and the dependence on the external 12 V power supply was cumbersome. Therefore, I switched to a pneumatically actuated balloon valve in the newer iteration of the device. The previous device was also not user-friendly due to the lack of streamlined device components, so I eliminated the Peltier cooler and heat sink assembly to reduce the bulk, since a pre-chilled aluminum surface was enough for lab based EBC collection procedures. The same Rev. C Wind sensor was used, but I used an Arduino Uno microcontroller (instead of Arduino Pro Mini) along with a 4-relay module interface to control balloon valve actuation. This reduced the dependence on power supply to just 5 V.

Temperature-based algorithm

I implemented a temperature-based algorithm which employs a dynamic calibration window to continuously update the temperature thresholds for valve actuation and adapt to changes in the breathing profile over the testing period. The algorithm uses the average temperature range of the last three breaths to calculate a threshold increase in temperature. The valve is programmed to open when the difference between the current temperature and the temperature at the start of the exhalation period exceeds the calculated threshold and is programmed to close after two successive

temperature decreases. The threshold temperature can be set to be within a percentage of the average temperature range observed within the last three breaths.

Correlation of temperature and CO₂ profiles

To demonstrate the reliability of the temperature sensor over an end-tidal CO₂ meter, I simultaneously compared the temperature and pCO₂ profiles collected using our temperature sensor and the capnometer function of the RespirAct Gas Control System (Thornhill Medical, Toronto, Canada), respectively. The pCO₂, partial pressure of CO₂ gas in mmHg, directly relates to CO₂ concentration. For this test, the temperature sensor was embedded within the respiratory mask connected to the capnometer. Two healthy human subjects were asked to breathe deeply into the device and multiple trials of 3-minute breathing periods were recorded to collect pCO₂ and temperature profiles.

Valve mechanism and collection body design

A square perpendicular-facing flat collection frame coming from the T-Valve was designed for condensate collection. This collection body design allowed for a cooled aluminum plate with a large surface area (12.5 cm x 13.3 cm; 166 cm²) to be attached to the external face of the device to ensure the collection surface (also aluminum) is maintained at sufficiently low temperatures (8 to 12 °C) for the entire duration of condensate collection. The square frame (made from PVC) contains slots for an aluminum collection plate and a clear acrylic plate (both 13.4 cm x 13.8 cm) with a 1.5 cm diameter hole that draws intake from the T-Valve. Once the breath has been condensed on the cooled collection plate, a built-in linear wiper is manually pushed across the collection surface to consolidate the EBC droplets (Figure 2.6). This collection design was compared to the commercially available R-Tube, which was also fitted with the selectively actuated pneumatic valve (Figure A.3).

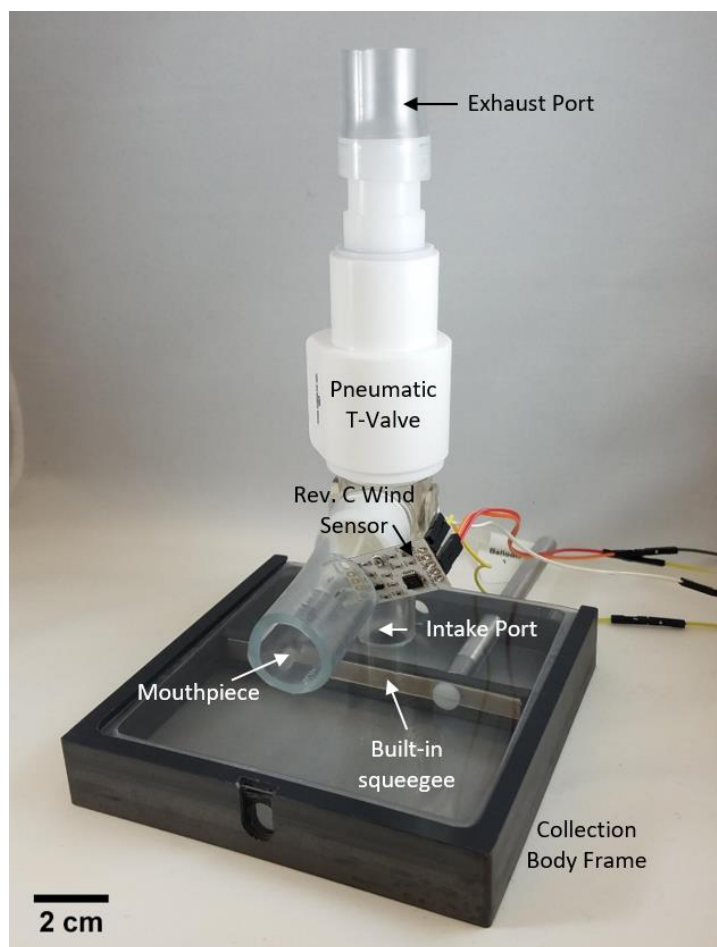


Figure 2.6. Selective EBC collection device.

Pictured with pneumatically actuated balloon T-valve, embedded Rev. C wind and temperature sensor. The selective valve in this design is a pneumatically actuated balloon T-Valve (Hans-Rudolph, Kansas, USA). The valve has one input to receive breath and two outputs: one for intake to the collection chamber when the user's breath is composed of deep lung air, and one for exhaust of the first portion of expiration that is not deep lung air. The selective valve is connected to a mouthpiece that allows the user to breathe fresh air through the entire collection process via a one-way diaphragm valve. Exhaled anatomical dead space air enters the device through the mouthpiece and exits at the exhaust port. The exhaled deep lung air is then collected through the mouthpiece, enters the intake port, and is collected on the cooled collection plate of the device. sensor, condensation plate with collection frame, and built-in linear wiper (squeegee).

Valve actuation for selective collection

The Arduino was interfaced with a Controller for Actuation of Inflatable Balloon-Type Automated Directional Control Valves (Hans-Rudolph, Kansas, USA) through a four-relay module as seen in Figure 2.7. A compressed air supply is fed to the controller at approximately 40 psi. To actuate the valve, a balloon inflates to create a seal on the flow passage bore of the T-valve. The controller relies on two buttons to move a switch between the normally open (NO) and normally closed (NC) pins that inflate and deflate the balloon valve, respectively. The manual balloon valve controller was adapted by replacing the push-button pin connections with a circuit originating from the relay module to control the switches (and subsequent valve actuation) based on the input from the Arduino. When the algorithm determines that the temperature has reached the appropriate threshold, it sets the relay to 'HIGH' to flip the switch and actuate the valve opening.

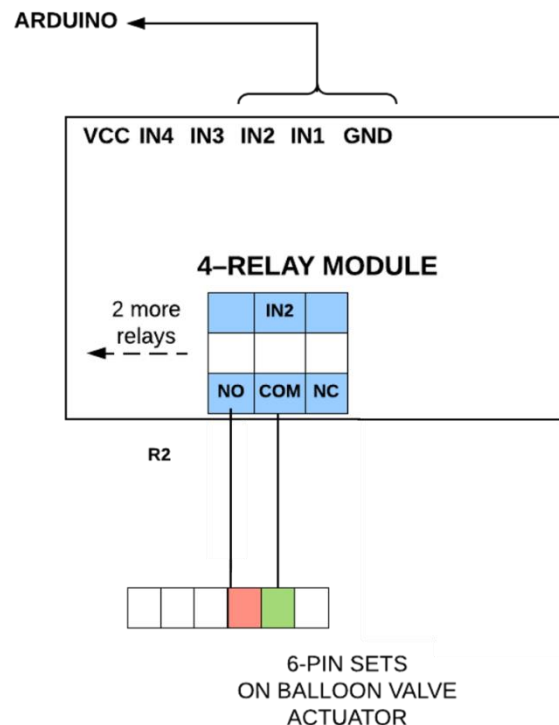


Figure 2.7. Circuit wiring of the four-relay module to the Arduino Uno microcontroller and balloon valve pneumatic actuator.

Shown is the one relay module used in the circuit (out of four modules). The relay is connected to pins inside the controller circuit board and serve to turn on/off the pneumatically powered balloons to control valve opening and closing.

The pneumatic valve actuation was employed at either a non-selective or selective threshold for each collection design (tray vs. R-Tube). Additionally, for each threshold, samples were collected from expiratory volumes of 7.5 L or 15 L. To determine the optimal collection design to be used for future feasibility studies on human subjects, two separate two-factor ANOVA analyses were performed to determine the effects of either 1) collection design and threshold or 2) collection design and total exhaled volume on the total volume of collected EBC condensate.

Device feasibility studies with temperature-based selective collection

Two device feasibility studies were conducted on human subjects to determine 1) whether selective valve actuation increases the glucose concentration or reduces the glucose concentration variability in collected EBC at different expiratory volumes and 2) whether collection platform or threshold had significant effects on glucose concentration variability. Subjects enrolled in the study did not have any history of diabetes or lung-related diseases. All subjects gave written consent to the experimental procedures, which had been approved by the Purdue University's Institutional Review Board. A total of six healthy subjects aged 19-22 years old (three females, three males) were recruited for the studies. Subjects were asked to fast for at least two hours prior to the study to ensure EBC glucose levels were as close to baseline as possible. Figure 2.8 illustrates the study set-up using the selective condenser.

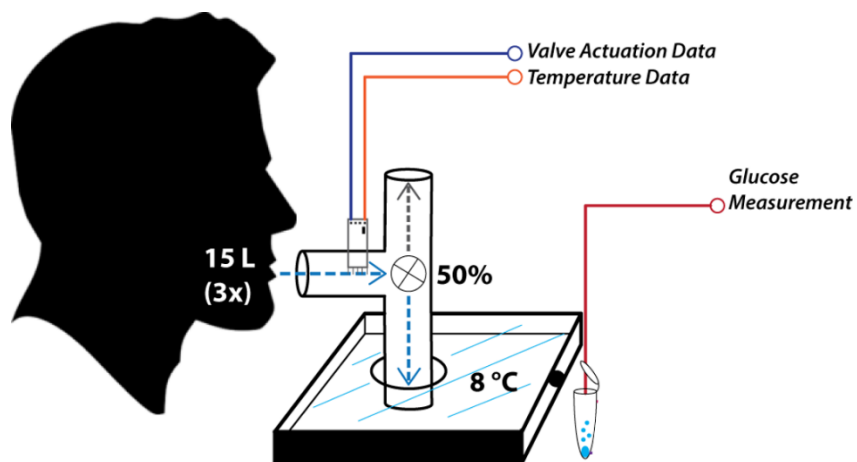


Figure 2.8. Representation of feasibility study set-up for data collection.

For both studies, the temperature, valve actuation, time for collection, total condensate volume, and EBC glucose concentration were measured and recorded.

Study 1: Three subjects (two females, one male) were enrolled in this study, which sought to compare the effect of expiratory volume and selective valve actuation on the collected EBC volume, time for collection, and corresponding glucose concentration. The pneumatic valve was used in combination with the tray-based platform, and EBC samples were collected in triplicate from expiratory volumes of 7.5 L or 15 L, with either non-selective or selective valve actuation (12 samples per subject). A sterilized, disposable mouthpiece was used for each subject and they were instructed to breathe normally into the device through their mouth for both inhalation and exhalation until the desired volume was collected. Samples were collected in a randomized order and stored in microcentrifuge tubes at -20 °C until further use. The collection tray, inlet port of the valve, and mouthpiece were disinfected with 70% ethanol between each sample collection to prevent contamination of residual glucose. A commercial fluorometric glucose oxidase assay (Abnova, Taipei, Taiwan) was used to quantify glucose concentrations. Fluorescence was measured using the SpectraMax M5 Microplate Reader (Molecular Devices, CA, USA) at ex./em. 540 nm/590 nm. The total volume of condensate, time for collection, and glucose concentration were recorded for each sample. Two-way ANOVA analysis was applied to determine if either expiratory volume or threshold level resulted in significant effects. Post-hoc Tukey pairwise tests were performed on trials where ANOVA reported significant differences.

Study 2: Three subjects (one female, two males) were enrolled in the second study, which sought to compare the effect of selective valve actuation and use of the R-Tube collection platform on collected EBC glucose concentration and variability. For each subject, EBC samples were collected (in a randomized order) in triplicate from total exhaled air volume of 15 L with either non-selective or selective valve actuation. The R-Tube, inlet port of the valve, and mouthpiece were disinfected with 70% ethanol between each sample collection to prevent contamination of residual glucose. New R-Tubes were used for each subject to prevent contamination between subjects. Glucose concentration was quantified using the previously described assay and time for collection and volume of condensate was recorded. A two-factor ANOVA analysis was used to determine the effects of threshold and expiratory volume on the glucose concentration. To analyze the extent of glucose concentration variability, coefficients of variation were calculated for each threshold and compared for significant differences. For comparison, similar calculations were performed on the first study to determine whether use of the R-Tube reduces glucose concentration variability in collected condensate, regardless of selective collection.

2.3 Results and Discussion

2.3.1 Time-based selective EBC collection via solenoid valve

Valve actuation comparison with temperature and CO₂ profiles

The time-based valve actuation demonstrated valve opening during the middle portion of the exhalation, as shown in Figure 2.9. However, the dependence on time did not account for fluctuations in breathing rate. In some exhalation periods, the valve opened too early or accidentally during the inspiratory downstroke.

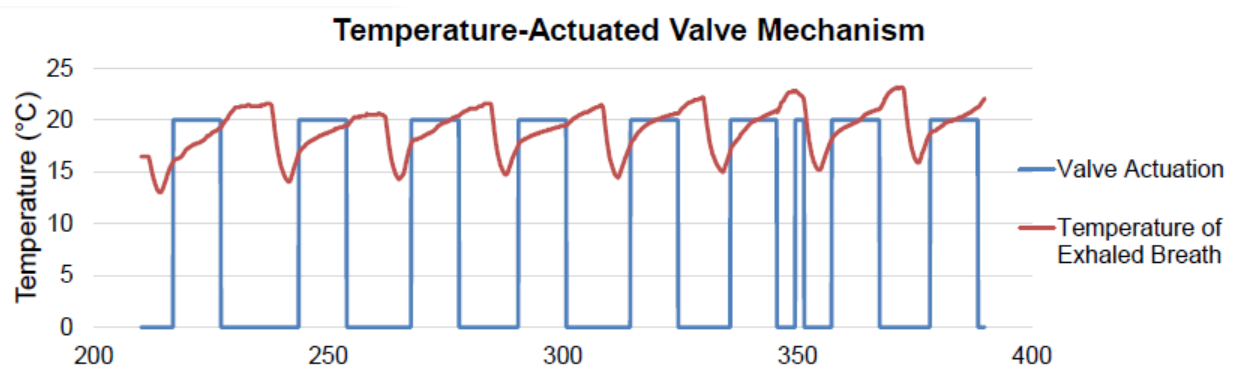


Figure 2.9. Overlay of temperature profile and time-based valve actuation.

The temperature data from the Rev. C wind sensor and CO₂ data acquired from the CO₂ sensor were not well-correlated (Figure 2.10). For one breath pattern, the valve was actuated for the latter portion of the exhalation. However, the CO₂ sensor was not able to accurately capture the capnography curve observed from end-tidal CO₂ meters. Furthermore, future valve actions did not correctly align with the peak temperature profiles. Thus, I determined that a dynamic calibration window can better accommodate changes in the user's breathing profile. Due to fluctuations in breathing rate and duration of exhalations, I concluded that valve action based on temperature rather than time may be a more reliable method to separate dead space from respiratory zone air.

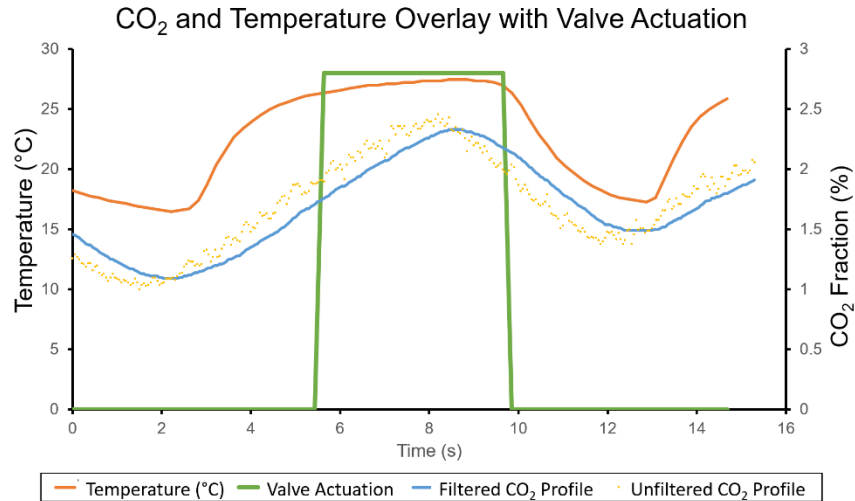


Figure 2.10. Overlay of temperature-valve actuation, and CO₂ data for a single exhalation.

Feasibility studies examining blood and EBC glucose

Feasibility studies conducted on human subjects demonstrated high intra-subject variability in blood to breath ratio but no significant subject-subject variability (Table 2.1). The average ratio for blood to breath glucose was 19581 ± 7390 , which is approximately 20-fold higher than the theoretical dilution factor of 1000. The condensation efficiency of this device was very poor, as it required, on average, greater than 15 L of total expiratory volume to produce 100 μL of condensate. The condensation plate used in this device had a large surface area for droplet formation, but collection very difficult and inefficient due to the fins on the collection surface.

Table 2.1. Glucose ratio and expiratory volume to condensate volume characterization.

Subject	1	2	3	4	Average	p-value
Blood to Breath Glucose Ratio	$30157 \pm$ 18545	$13391 \pm$ 4821	$15968 \pm$ 11701	$18807 \pm$ 12323	$19581 \pm$ 7390	0.112
Expiratory Volume (L) for 100 μL EBC	$9.70 \pm$ 3.86	$16.38 \pm$ 9.91	$21.51 \pm$ 8.98	$15.96 \pm$ 11.59	$15.89 \pm$ 4.84	0.104

2.3.2 Temperature-based selective EBC collection via balloon valve

Temperature and CO₂ profile comparison of exhaled breath

Human breathing profiles showed consistent, strong correlation between temperature and CO₂ data, as shown in Figure 2.11. The CO₂ curve is characterized by a steep initial rise of pCO₂ followed by a plateau during exhalation and subsequent decrease during inhalation. The buildup of residual humidity and temperature may have affected the Rev. C wind and temperature sensor's temporal resolution and thus prevented a plateau from forming on the temperature curve. However, the two profiles were well-correlated and there was little to no time lag observed. Therefore, it can be concluded that a temperature sensor can be used for selective collection of deep lung air instead of a costly EtCO₂ meter.

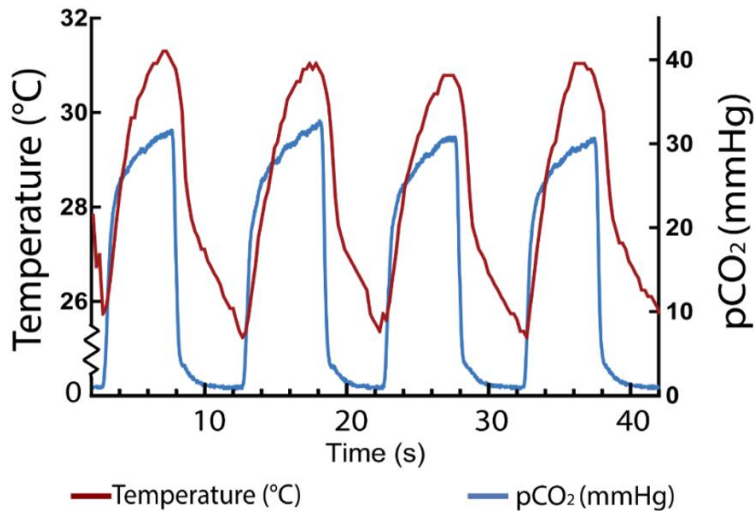


Figure 2.11. Temperature and end-tidal CO₂ profile comparison.

Valve actuation algorithm for selective collection

The valve actuates based on the temperature threshold determined by the algorithm. Figure 2.12 shows results from a trial taken from a healthy human subject in which the valve is programmed to open when the current temperature has crossed 40% of the calculated threshold range. The temperature threshold in green remains consistently within the temperature bounds of the breath.

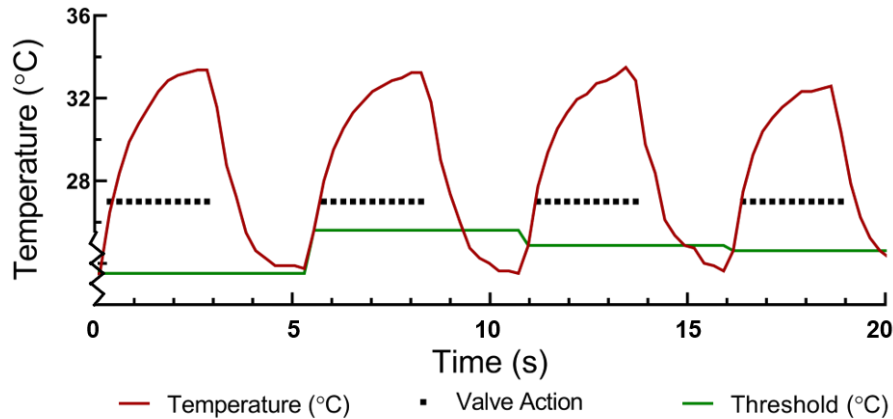


Figure 2.12. Overlay of temperature profile, temperature-based valve action, and dynamically calibrated selection threshold (40%).

The temperature-CO₂ correlation results were used to select an appropriate threshold for EBC studies to reliably eliminate the dead-space and transition regions. The derivative of the CO₂ profile was used to identify the beginning of the plateau region (Figure 2.13). This is when the slope of CO₂ has fully leveled out (no longer increasing), which ensures the transition region has been exited and only the plateau phase is collected. A threshold percentage of 70% of the temperature profile ensured that exhaled air was collected only after the plateau phase was reached. This was confirmed after comparing the overlap of the thresholds and the start of the CO₂ plateau. The 70% threshold was used for all feasibility studies evaluating the effects of selective collection on condensate volume, glucose concentration, and time for collection.

Temperature-Based Actuation and CO₂ Plateau Comparison at 0%, 50%, and 70% Thresholds

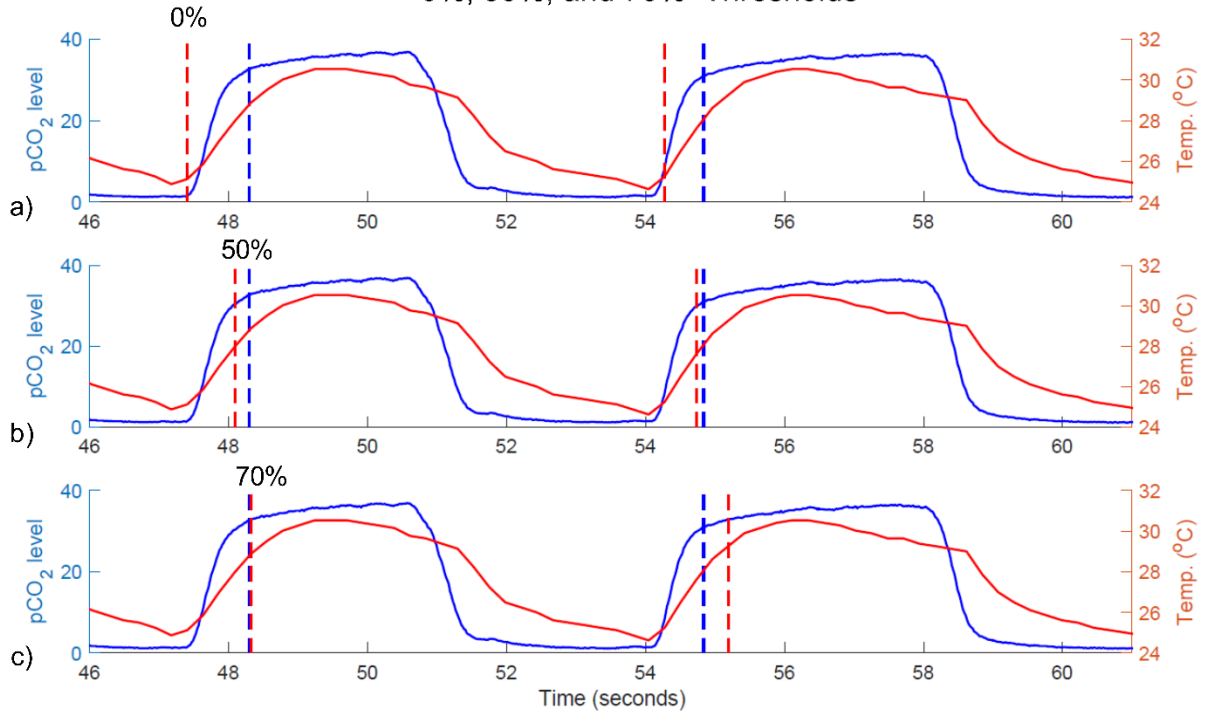


Figure 2.13. Temperature-based actuation and CO₂ plateau comparison at 0%, 50%, and 70% thresholds.

Effect of selective threshold and expiratory volume on EBC glucose concentration

In EBC collected from three subjects using the tray-based condenser design, two-factor ANOVA revealed that the threshold effect on glucose concentration was not significant ($p=0.07$), although trends pointed to increased glucose concentration with a selective threshold (Table 2.2). Expiratory volume had no significant effect on glucose concentration ($p=0.79$) and there were no interaction effects observed between threshold and expiratory volume ($p=0.28$). It took significantly longer to collect EBC from 15 L of exhaled breath compared to 7.5 L (mean difference of 88.5 ± 39.7 s) but the time to collect EBC did not significantly change between threshold levels. Effects on volume of collected condensate were evaluated with two participants, as one subject did not have condensate volume data. Larger expiratory volumes resulted in significantly higher condensate volumes (mean difference 55.42 ± 13.54 μ L) and the threshold level (mean difference 16.25 ± 13.545 μ L).

Table 2.2. Effect of threshold and expiratory volume on EBC collection (n=3, mean \pm SD).

Expiratory Volume	7.5 L		15 L	
	0%	70%	0%	70%
Threshold				
Time (s)	82.0 ± 13.2	85.2 ± 11.0	180 ± 13.0	164 ± 43.7
Volume (μ L)	61.7 ± 7.07	78.3 ± 7.07	150 ± 4.71	101 ± 8.25
Glucose (μ M)	0.42 ± 0.15	0.54 ± 0.11	0.24 ± 0.16	0.65 ± 0.36

Selective collection of respiratory zone condensate based on peak temperature profiles in our studies did not yield conclusive results for changes in glucose concentration nor variability. I originally hypothesized that a selective threshold level of 70% would enrich the glucose concentrations in samples collected selectively due to the exclusion of dead space air. The start of the CO₂ plateau (when the slope of the CO₂ profile levels out to zero) was best correlated with the temperature value that was at 70% of its peak for a given exhalation profile. While the effect of threshold on EBC glucose concentration was not significant, the p-value for the ANOVA test was borderline (0.0708). Additionally, changing the threshold (from non-selective to selective) for individual participants at a given volume resulted in a decrease in glucose concentrations in only one of the six combinations. Although, this would support the hypothesis that selective condensation would increase glucose concentration, the small sample size (n=3) was a limiting factor.

Comparison of EBC volume and glucose concentration using R-Tube

The mean EBC volume collected at both non-selective (0%) and selective (70%) temperature thresholds using the R-Tube was significantly greater ($p < 0.0001$) than the volume collected using the tray from expiratory volumes of 7.5 L and 15 L. (Table 2.3). EBC collected from the R-Tube was especially sensitive to condensate loss at selective thresholds ($p < 0.0001$).

Table 2.3. EBC volume and glucose concentration of condensates collected from tray and R-Tube (n=3, mean \pm SD).

Collection Method	Tray		R-Tube	
Threshold	0%	70%	0%	70%
Volume from 7.5 L (μ L)	54.0 \pm 5.3	38.3 \pm 2.9	227.7 \pm 2.5	157.3 \pm 6.4
Volume from 15 L (μ L)	90.0 \pm 15.0	103.3 \pm 25.2	403.3 \pm 6.1	286.7 \pm 20.8
Glucose (μ M)*	0.24 \pm 0.16	0.65 \pm 0.36	0.44 \pm 0.26	0.26 \pm 0.11
CV (%)	75.2 \pm 71.6	79.1 \pm 62.7	34.6 \pm 18.4	49.3 \pm 42.4

*Glucose concentration data corresponds to EBC collected from 15 L expiratory volumes only.

Samples collected with the R-Tube showed no significant difference in glucose concentrations or variability between thresholds (Figure 2.14b). Trends pointed towards lower variability (coefficient of variation) in glucose concentrations but this difference was not quite significant when compared to samples collected with the tray (Table 2.3)..

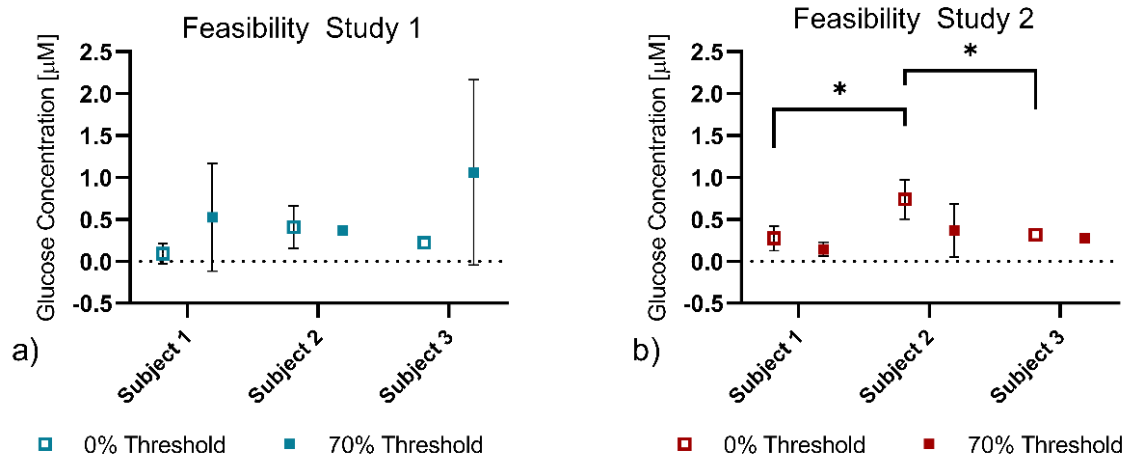


Figure 2.14. Comparison of glucose concentrations between 0% and 70% thresholds.

Glucose concentrations are shown for each subject for a) feasibility study 1 (N=3, n=3) and b) feasibility study 2 (N=3, n=3) collected from an expiratory volume of 15 L.

2.4 Future Directions

While the temperature-based selection threshold did not significantly improve glucose concentrations or reduce variability, a conclusive result cannot be established due to the small size and narrow age range. A larger study with a broader demographic of non-diabetic individuals without lung-related comorbidities should be conducted to determine the impact of selective thresholds on EBC glucose concentration and variability. In the future, an even higher selection threshold should be implemented and characterized for its effect on condensate glucose concentration and intra-subject variability. In this study, we were limited to a threshold of 70% because higher thresholds resulted in significant condensate loss in the tray-based platform. Moving forward, for efficient condensation with a more selective threshold, the R-Tube should be used with the selective valve in place of the tray. Although selective EBC collection is sensitive to condensate loss, the R-Tube produces more than enough condensate for glucose analysis to compensate for this loss. For long term portability, the valve design and operation should not rely on external air supply or pneumatic regulator. In this regard, a servo-operated butterfly valve may be implemented.

2.5 Conclusion

I have demonstrated that temperature based selective EBC collection is a reliable method to exclude exhalate in the transition phase of the alveolar plateau by employing a dynamically calibrated threshold. Compared to the time-based method, this method accounts for fluctuations in the user's breathing profile (breathing rate, temperature range of exhalation) to generate a robust and tunable selection threshold. In doing so, this device bypasses the need for expensive end-tidal CO₂ sensors. The pneumatically actuated balloon valve in the final prototype sufficiently seals the passage of the exhaust port during valve actuation, allowing exhalate to be directed through the inlet port of the device for subsequent condensation. Design iterations focused on improving condensate formation and ease of collection; ultimately, the R-Tube proved to be the best collection platform. The condensate collected from this device provides a robust sample for evaluating EBC glucose concentrations as well as other analytes of interest such as inositols, inflammatory markers, and peptide biomarkers.

3. CHARACTERIZATION OF BLOOD AND BREATH GLUCOSE PROFILES IN NORMOGLYCEMIC AND DIABETIC INDIVIDUALS

3.1 Rationale

To establish a functional relationship between EBC glucose and blood glucose, a pilot study of oral glucose tolerance tests (OGTT) on normoglycemic and type 2 diabetic subjects was conducted at the Indiana University (IU) Clinical and Translational Sciences Institute (CTSI) (Indianapolis, IN). The purpose of these studies was two-fold: to examine the linear relationship of glucose concentrations in these fluid compartments and to also determine whether diabetes significantly affects the blood to EBC glucose ratios. The studies also serve to further evaluate the feasibility of using the previously developed selective EBC condenser on normoglycemic and type 2 diabetic human subjects during a three-hour OGTT. By sampling EBC from the deep lung circuit, we hypothesized that glucose concentrations would be less dilute and exhibit less variability, enabling a more standardized approach to non-invasively collect key respiratory analytes and biomarkers.

3.2 Materials and Methods

3.2.1 Subject selection and preparation

All subjects gave written consent to the experimental procedures, which had been approved by Indiana University's Institutional Review Board. Two normoglycemic and two obese type 2 diabetic patients were recruited for the study. Full inclusion and exclusion criteria are provided in Table B.1. All subjects were in good health, except for diabetes. For the diabetic subjects, all blood pressure and/or cholesterol lowering medications were withheld the morning of the glucose testing procedure. Subjects were admitted to IU CTSI Clinical Research Center (CRC) the morning of the planned study after fasting for 10 hours (water only from 10 pm).

3.2.2 Blood and breath sampling

An intravenous catheter was placed antegrade for blood sampling. Blood samples were collected at baseline, prior to administration of the standardized glucose drink on the morning of

the study (designated T-10 minutes). Baseline (T-5) intravenous blood glucose was measured using a bedside YSI 2300 STAT-plus glucose analyzer (Yellow Springs Instruments, OH, USA) and exhaled breath samples were collected using the condenser (pneumatic valve with tray-based collection platform). Each subject was provided with a sterilized, disposable mouthpiece for the duration of the trial. For each sample, subjects exhaled a total of 7.5 L of air into the device and condensate was collected at a selection threshold of 70%. A standard 75 g oral glucose drink was administered (T 0) and completely ingested within 5 minutes. Blood and EBC were then simultaneously sampled every 5 minutes for the first 60 minutes, then every 20 minutes for the subsequent 120 minutes (T 180). For one type 2 diabetic subject (T2D01), blood and exhaled breath were sampled every 10 minutes during the remaining 120 minutes. For one normoglycemic subject (N01), the study was cut short by 1 hour and 20 minutes due to scheduling conflicts. The subjects were instructed to begin breathing into the device approximately 45 s prior to the blood draw to ensure that the EBC and blood glucose measurements were aligned. Between sample collections, the collection tray, mouthpiece, and inlet port of the valve were disinfected with 70% ethanol to prevent residual glucose contamination. The collected EBC samples were transported (in dry ice maintained at $-20\text{ }^{\circ}\text{C}$) back to Purdue University and stored at $-80\text{ }^{\circ}\text{C}$ until analysis. Glucose content was analyzed within one day of the collection date using a commercial fluorometric glucose assay in two replicates of $25\text{ }\mu\text{L}$.

3.2.3 Statistical methods

EBC glucose and blood glucose concentrations (converted to micromolar units) were plotted over time for each subject to visualize trends in correlation and apparent time lag. A nonparametric Spearman correlation was computed for all data sets independently at 95% confidence. Next, blood to EBC glucose ratios were calculated by dividing the blood glucose concentrations by EBC glucose concentrations and separated into diabetic ($n=49$) and normoglycemic sample ($n=38$) groups. To investigate whether diabetes significantly affects the glucose dilution factor, a two-tailed unpaired t-test assuming unequal variances was performed with a 95% confidence interval.

To develop a linear model for EBC and blood glucose for diabetic subjects compared to normoglycemic subjects, only the values in the first hour of the trials were used due to inconsistencies in the time increments in the second and third hours between studies. Equation (4)

describes the predicted relationship between blood glucose x_t and EBC glucose y_t , in which β_0 , β_1 , and ε correspond to the y-intercept, blood to breath glucose ratio, and the error, respectively. The EBC glucose values were logarithmically transformed to ensure normality, as confirmed by a Shapiro-Wilk test. Next, separate first order least squares regression models were generated for the transformed normoglycemic and diabetic data, respectively. The model slopes were compared for significance using an extra sum of squares F-test. All statistical analysis was performed using GraphPad Prism version 8.2.1.

$$y_t = \beta_0 + \beta_1 x_t + \varepsilon \quad (4)$$

For data sets with poor goodness of fit with the linear regression models, the first hour of blood and EBC profiles were investigated for potential time lag using the sample cross correlation function (CCF) in R. After adjusting the previously transformed data set for the apparent time lag, a new least squares regression model was generated and analyzed for goodness of fit, normality of residuals, and whether correlation was significant. Cross correlation analysis was performed using R Studio version 1.1.463.

3.3 Results and Discussion

OGTT studies demonstrated highly varied relationships between blood and EBC glucose (Figure 3.1). Spearman correlation tests resulted in significant correlation for EBC and blood glucose for both diabetic subjects T2D01 and T2D02 ($r=0.57$ and $r=0.49$, respectively). Neither normoglycemic subject N01 and N02 showed significant correlation between EBC and blood ($r=-0.15$ and $r=0.24$, respectively). The apparent time lag in the normoglycemic subject N02 EBC glucose profile may have significantly contributed to the weak correlation. The distinct spike in EBC glucose concentration at the end of the T2D01 trial and spike at the start of the N01 trial were significant outliers ($Q=1\%$) and may have also weakened the correlation.

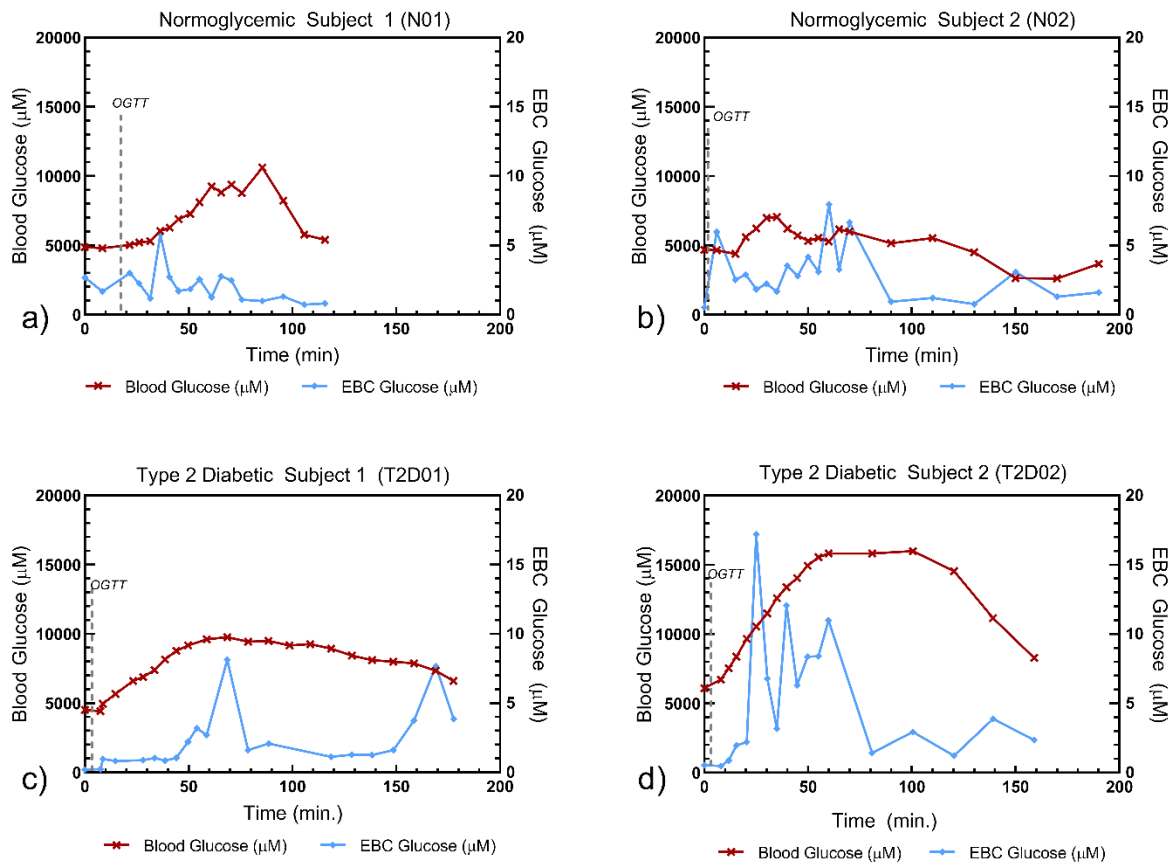


Figure 3.1. Blood and EBC glucose profiles for (a-b) normoglycemic and (c-d) type 2 diabetic subjects over time during oral glucose tolerance test. Dashed lines indicate time of glucose drink consumption.

The glucose ratios between blood and EBC were not consistent for the duration of the trials and showed high variability especially at the beginning of the OGTT. Furthermore, the difference between normoglycemic and diabetic blood to EBC glucose ratios (2019 ± 795) was significant ($p=0.01$), as illustrated in Figure 3.2b. Glucose ratios across all subjects were higher in the latter half of the trial due to sharp drops in EBC glucose profiles compared to the gradual fall of blood glucose profiles (Figure 3.2a). This difference was more pronounced in diabetic subjects due to the relatively high blood glucose profiles compared to those of normoglycemic subjects.

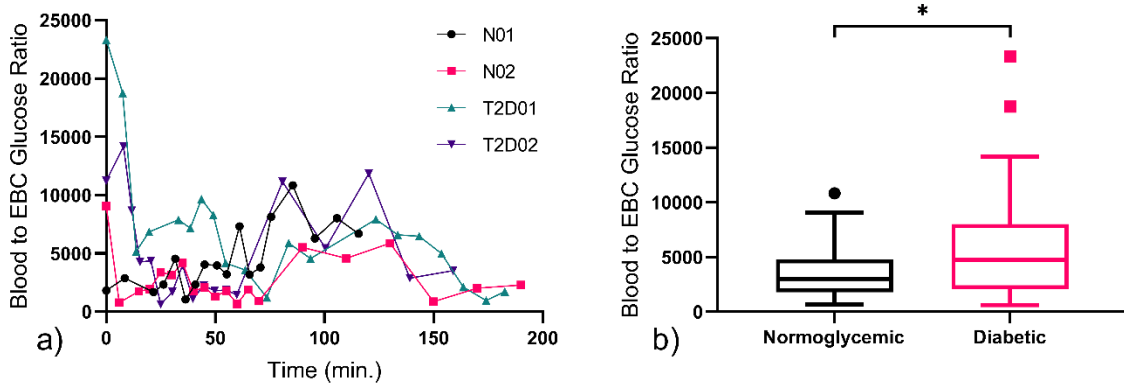


Figure 3.2. Blood to EBC glucose ratios for normoglycemic and type 2 diabetic subjects.

(a) blood to EBC glucose ratios over time for all subjects (normoglycemic – N01/N02; type 2 diabetic: T2D01/T2D02). (b) Distribution of blood to EBC glucose ratios for normoglycemic ($N=2$, $n=19$) vs. type 2 diabetic ($N=2$, $n=24$) data points indicated by Tukey box-whisker plots ($p=0.01$).

EBC glucose concentration data were logarithmically transformed for both diabetic and normoglycemic samples to ensure normality (Figure B.1). Two linear least squares regression models were developed to predict EBC glucose from blood glucose for normoglycemic (5) and diabetic (6) sample populations for the first hour of OGTT, with x corresponding to blood glucose concentration (μM) and y corresponding to EBC glucose concentration (μM).

$$\log(y) = -6.11 \times 10^{-5}(x) + 0.81 \quad (5)$$

$$\log(y) = 1.29 \times 10^{-4}(x) - 0.94 \quad (6)$$

The model slopes were significantly different ($p < 0.0001$), demonstrating that diabetes may impact the relationship between EBC and blood glucose. However, the normoglycemic model slope was not statistically significant from a slope of zero ($p > 0.05$) and only had a coefficient of determination of $r^2=0.16$. Conversely, the diabetic model had a significantly higher coefficient of determination ($r^2=0.80$) and resulted in normally distributed residuals when plotted with the experimental data (Figure 3.3).

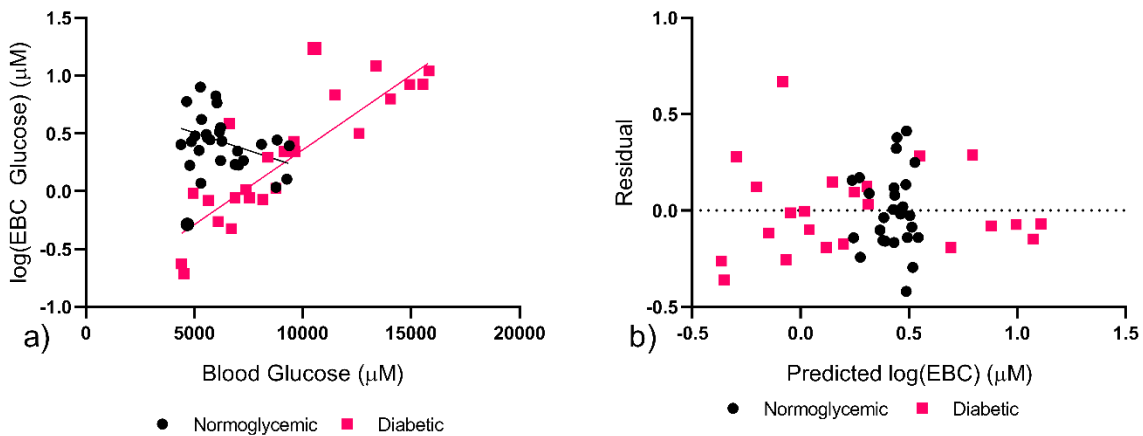


Figure 3.3. Linear model of EBC glucose to blood glucose.

(a) Linear regression of logarithmically transformed EBC glucose to blood glucose values for diabetic (pink squares) and normoglycemic (black circles) data points during the first hour of OGTT (during rise of glucose profiles); (b) Residual plot of experimental data to linear model for diabetic and normoglycemic data points.

Higher correlation between blood and EBC glucose was observed for diabetic subjects over normoglycemic subjects due to a significant time lag in EBC glucose for one normoglycemic subject. Upon further examination, the blood and EBC glucose profiles for diabetic subjects followed a better linear relationship for the first hour of the trial, during the rise of blood glucose ($r^2 = 0.80$).

Time lag analysis of subject N02’s EBC glucose profile for the first hour of the OGTT revealed a high autocorrelation factor with for a lag value of $h = -6$, suggesting that the blood glucose profile may lead the EBC glucose profile by 30-minutes ($h = 5$ minute increments) (Figure 3.4).

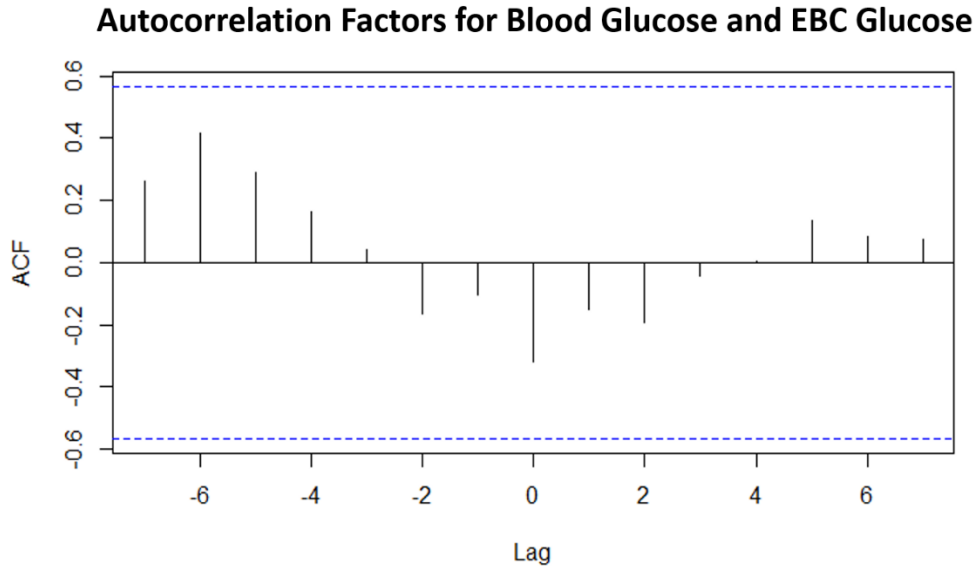


Figure 3.4. Correlogram of the observed EBC glucose profile with blood glucose profiles at various time lags, h , for normoglycemic subject N02.

Assuming blood glucose and EBC glucose are time series $x_{(t+h)}$ and y_t , respectively, h corresponds to a series of values $0, \pm 1, \pm 2, \pm 3$, and so on that are representative of discrete time intervals. The CCF function was used to create a set of autocorrelations (ACF) between $x_{(t+h)}$ and y_t and identify the time delay value (h) that results in the highest correlation. When $x_{(t+h)}$ is correlated with y_t , with h being negative, then it is implied that blood glucose leads EBC glucose.

Although the relationship between EBC and blood glucose for the time-lag adjusted N02 normoglycemic profile resulted in a stronger goodness of fit ($r^2=0.38$ vs. $r^2=0.16$), the correlation was not significant enough to establish a non-zero linear relationship between blood and EBC glucose (Figure 3.5). Since time lag was not universally observed across subjects, more studies are necessary to determine if this is expected of glucose transport from blood to ASL and ultimately EBC.

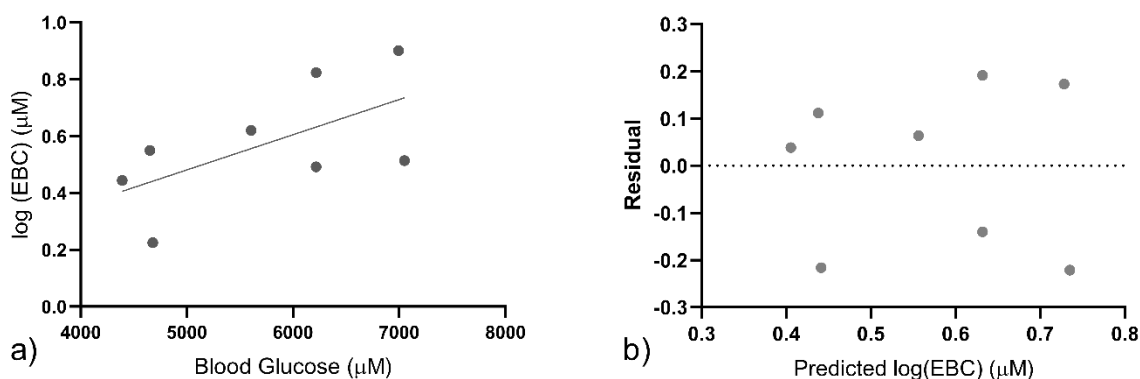


Figure 3.5. Linear model of time-lag adjusted EBC glucose to blood glucose for normoglycemic subject N02.

(a) Linear regression of logarithmically transformed EBC glucose (adjusted by 30 minutes) to blood glucose values for the first hour of normoglycemic subject N-02 OGTT; (b) Residual plot of experimental data to linear model.

The gradual fall in blood glucose did not translate to a gradual fall in EBC glucose; there was a sharp drop in EBC glucose concentrations across all subjects. The peak EBC glucose concentrations for diabetic subjects were significantly higher than those observed in the normoglycemic subjects. Thus, the sharp drop in EBC concentrations to baseline values resulted in significantly higher ($p=0.01$) blood to EBC glucose ratios for diabetic subjects (5640 ± 4750) compared to normoglycemic subjects (3621 ± 2549). In previous studies, dilution corrections based on conductivity were used to estimate blood to breath glucose ratios for healthy and diabetic individuals. Baker *et al.* calculated median dilution factors (ASL glucose to condensate glucose) of 4248 and 15520, for healthy and diabetic volunteers, respectively³⁰. The dilution corrections resulted in ASL glucose concentrations of 0.4 mM and 1.2 mM for healthy and diabetic individuals, with no difference in the corresponding blood to ASL glucose ratios. The significantly dilute EBC glucose concentrations (in relation to blood glucose) in diabetic subjects observed in our study and in literature warrants further analysis of how airway glucose homeostasis is reflected in exhaled breath condensate.

In most individuals without lung-related comorbidities such as COPD and CF, which cause chronic airway inflammation, the airway glucose homeostasis capability is not compromised. In our experiments, the OGTT trials induced hyperglycemic blood glucose profiles but none of the subjects had pre-existing conditions related to lung disease. The rapid fall of EBC glucose

concentrations back to baseline levels may indicate functional airway glucose homeostasis. Recent studies have shown that high ASL glucose concentrations fall back to baseline when normoglycemia is restored but it is unclear at what rate, when compared to blood glucose. For diabetic subjects, blood glucose levels were slower to reach baseline concentrations (Figure 3.1c-d), but EBC glucose concentrations fell at the same rate as normoglycemic subjects, leading to higher blood to EBC glucose ratios in the diabetic subjects. If the same trend is observed in ASL glucose homeostasis for the same subjects, then blood to ASL glucose ratios may also be higher in diabetic subjects; this supported by studies confirming that diabetic subjects without lung-related co-morbidities have a higher dilution factor for blood to ASL glucose³⁰. Therefore, the blood to breath glucose ratio during homeostasis may indicate whether the individual's airway glucose homeostasis mechanisms are compromised and consequently, if they are at risk for respiratory infections.

3.4 Future Directions

Characterizing the rate of glucose homeostasis in the airways with relation to blood glucose will be especially beneficial for diabetic patients, whose airway glucose levels may exacerbate respiratory infections if not effectively regulated by GLUTs. The advantage of using EBC as a sample matrix for key respiratory biomarkers and analytes is the non-invasive and convenient method of collection when compared to ASL, which requires bronchioalveolar lavage. To establish a better model of glucose homeostasis rates in blood and EBC, a larger study should be performed that focuses on the latter part of OGTT, with more time increments to establish a linear model for blood and EBC during the fall of glucose concentrations back to baseline. Analysis of glucose concentration changes during homeostasis for blood vs. EBC sampled from various regions of the respiratory tract, including alveoli, proximal bronchioles, and the conducting zone will also shed light on how ASL glucose is transported to EBC. In this regard, our device can provide tunable selection criteria to condense specific regions of the exhalate and is not only limited to deep lung air.

3.5 Conclusion

I have assessed the relationship between blood and EBC glucose during the rise of glucose concentrations in OGTT studies. Using the previously developed EBC condenser, I evaluated the functionality and patient ease-of-use during the studies. I characterized a stronger linear relationship between blood and EBC glucose for type 2 diabetic subjects compared to normoglycemic subjects. However, more studies are required to support this observation. In addition, blood to EBC glucose ratios significantly differed between normoglycemic and diabetic subjects in this study; this is representative of trends observed in literature. This study provides new knowledge of respiratory physiology in terms of how glucose airway homeostasis function is represented in EBC for normoglycemic vs. diabetic subjects.

4. ENGINEERING GLUCOSE BINDING PROTEIN (GBP) WITH CHEMO-ENZYMATIC TAG

4.1 Rationale

The *E. coli* glucose binding protein (GBP) is a promising candidate for a highly stable, fluorescent biosensor for EBC glucose detection due to its exquisite sensitivity for glucose ($K_{D, \text{glucose}}=0.35 \mu\text{M}$)¹⁰¹. Most of the techniques used to engineer GBP have relied on introducing site-directed mutations such as cysteine residues near the binding pocket or the N-terminus of the protein for thiol-reactive surfaces to covalently attach. However, many of these covalent modifications in published studies require additional purification steps and have resulted in reduced sensitivity of the GBP sensor^{87,88,102}. Thus, a bio-orthogonal and site-specific labeling method may result in highly functional GBP that can be conjugated via common chemistries, such as click reactions, to functionalized surfaces directly from lysate.

A chemo-enzymatic labeling technique developed by the Kinzer-Ursem lab at Purdue University is used to achieve site-specific bio-orthogonal labeling of bacterial proteins with an azide tag for streamlined conjugation to alkyne-labeled surfaces¹⁰³. Azide and alkyne groups are bio-orthogonal and thus are not found in native biological systems; this makes it possible for them to be selectively introduced to specific biological components. Bio-orthogonal azide-labeling of proteins has been previously demonstrated in Calmodulin (CaM), a calcium (Ca^{2+})-binding protein. This method takes advantage of the properties of the enzyme, N-myristoyl transferase (NMT), which when co-expressed with a natural substrate protein, appends a fatty acid analog, myristic acid, to the N-terminus of the substrate protein¹⁰⁴. NMT is only found in eukaryotic cells and certain species of yeasts and protozoan parasites, making it orthogonal towards bacterial expression systems, which do not have endogenous NMT. The bio-orthogonality prevents non-specific crosstalk between NMT and endogenous bacterial proteins when co-expressed in *E. coli*. Kulkarni *et al.* previously engineered CaM with an N-terminal recognition sequence for NMT (derived from either the human calcineurin B subunit or yeast ADP ribosylation factor). By co-expressing NMT and engineered CaM in the presence of an azide-fatty acid, 12-azidodecanoic acid (12-ADA) instead of the natural substrate (myristic acid), bio-orthogonal labeling of CaM with an N-terminal azide group was achieved within the *E. coli* expression system with over 98%

labeling efficiency¹⁰³. Selective conjugation of 12-ADA-CaM to alkyne-labeled tetramethylrhodamine (TAMRA) via copper-catalyzed azide alkyne cycloaddition (CuAAC) was possible directly from clarified cell lysate containing the overexpressed protein.

CuAAC is the most prominent click chemistry conjugation technique, in which azides undergo a [3+2] cycloaddition with copper(I)-catalyzed terminal alkynes to form a triazole product¹⁰⁵ (Figure 4.1a). Because copper, when used as a catalyst, demonstrates significant toxicity issues and irreversible quenching of other fluorescent particles such as QDs, alternate methods of azide-alkyne cycloaddition have been developed in recent years¹⁰⁶. One such reaction is strain-promoted azide-alkyne cycloaddition (SPAAC) (Figure 4.1b) developed by Bertozzi and co-workers in 2004¹⁰⁵.

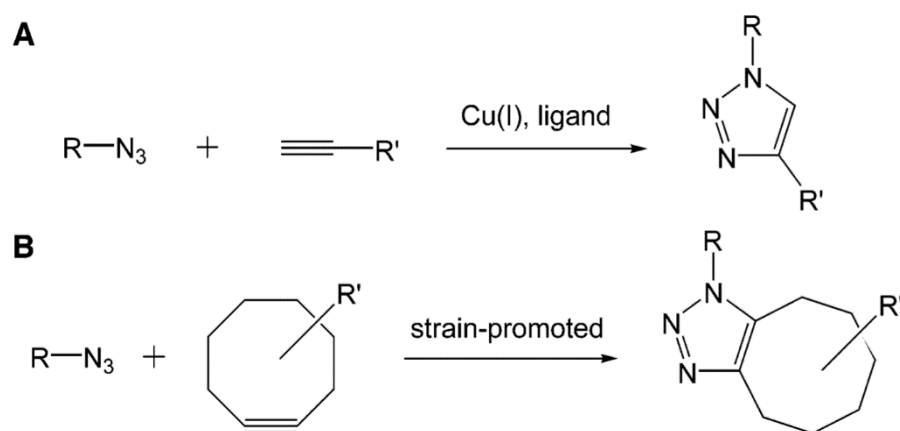


Figure 4.1. Azide-alkyne cycloaddition reaction schematics. (A) Copper-catalyzed azide-alkyne cycloaddition; (B) Strain-promoted azide-alkyne cycloaddition. Both form triazole products.

In this reaction, a [3+2] cycloaddition with an azide group was achieved through a ring-strained destabilization of a cyclooctyne derivative to form a triazole product. While the SPAAC reaction proceeds for a longer time than CuAAC, it occurs in the absence of auxiliary reagents, making it a convenient conjugation method for biological applications¹⁰⁷. I take advantage of bio-orthogonal chemo-enzymatic labeling to engineer GBP with an N-terminal azide tag for downstream conjugation to alkyne-labeled surfaces via SPAAC (Figure 4.2).

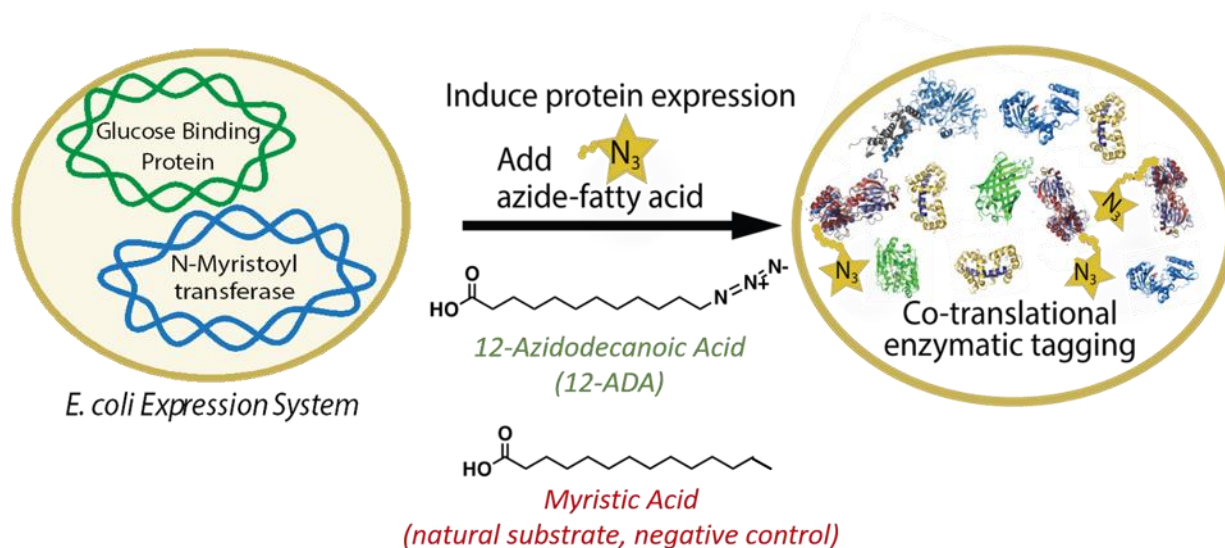


Figure 4.2. Chemo-enzymatic labeling of GBP within *E. coli* expression system when co-expressed with NMT in the presence of 12-ADA.

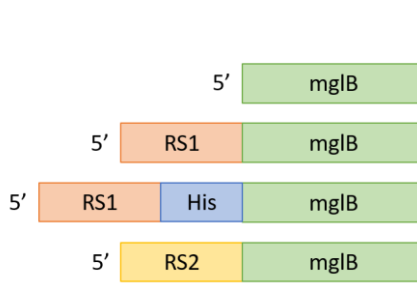
4.2 Materials and Methods

4.2.1 Cloning of engineered *mglB* constructs

The gene encoding GBP in *E. coli* is *mglB* (~1 kb). To engineer the protein with an N-terminal recognition sequence for NMT, several plasmid constructs were created from the wild-type (*wt-mglB*) plasmid, a generous gift from the Tolosa lab at the University of Maryland, Baltimore County (UMBC). The *wt-mglB* plasmid was then digested and re-ligated into a pGEM T-Easy vector. To engineer the protein, the plasmid vector used for cloning was pET15b. A nucleotide sequence encoding the NMT recognition site (RS1) derived from the human Caliceneurin B subunit was inserted at the 5' end of *wt-mglB* via polymerase chain reaction (PCR) using a high-fidelity polymerase (Deep Vent, New England Bio-Labs, Ipswich, MA). After restriction digestion, the PCR insert was ligated into the pET15b vector and transformed into chemically competent *E. coli* DH5 α cells. Similarly, another *mglB* construct was engineered with a shorter nucleotide sequence encoding the NMT recognition site (RS2) derived from the yeast ADP ribosylation factor. For alternative affinity purification purposes, a 6xHistidine sequence was cloned into the *RS1-mglB* plasmid via 2-step PCR (Figure 4.3). To confirm successful cloning, samples were analyzed via low-throughput laboratory (LTL) sequencing through the Purdue Genomics Core Facility. Custom primers corresponding to the pET15b vector backbone near

restriction sites were used in the sequencing analysis. Sequencing results were compared to expected sequences through the sequence alignment feature on A plasmid Editor (ApE) (Figure C.1). In addition, a diagnostic restriction digest and subsequent gel electrophoresis analysis was performed to visually confirm successful cloning of the engineered constructs into the pET15b vector. For information on *mglB* primer design, PCR, digestion, and ligation protocols, please refer to Appendix C.

4.2.2 Protein expression and bio-orthogonal labeling of engineered GBP



Name	Description	Sequence
<i>mglB</i>	Gene encoding glucose binding protein	n/a
RS1	Recognition sequence for N-myristoyl transferase from human calcineurin B subunit	MGNEASYPL
His	Hexahistidine linker	HHHHHH
RS2	Recognition sequence for N-myristoyl transferase from yeast ADP ribosylation factor	MGLFASK

Figure 4.3. Engineered constructs of *mglB*. The *wt-mglB* was inserted into the pGEM T-Easy vector; the remaining constructs were inserted into the pET15b vector.

The *RS1-mglB* and *RS2-mglB* plasmids were independently co-transformed with the plasmid encoding human NMT (*hNMT1*) into chemically competent BL21 (DE3) *E. coli* cells. Expression cultures were grown in an incubator/shaker (37 °C, 250 rpm) in LB medium supplemented with 50 µg mL⁻¹ kanamycin and 100 µg mL⁻¹ ampicillin. Once cultures grew to an OD₆₀₀ of 0.4-0.6, protein expression was induced with 1 mM IPTG. Along with IPTG, 0.5 mM of 12-ADA was added to the expression culture. As a negative control, 0.5 mM of myristic acid was added to the expression culture instead of 12-ADA. Myristic acid is the natural substrate of NMT and does not contain an azide moiety (Figure 4.2). After 3, 6, and 20 hours of protein expression, cells were harvested via centrifugation and stored at -80 °C until use. An uninduced pellet was also stored at -80 °C until use. In addition, a separate culture for RS1-GBP and RS1-His-GBP was expressed in the absence of both 12-ADA and Myristic Acid. As a control experiment, *wt-mglB* (in pGEM T-Easy vector) was also transformed into chemically competent BL21 (DE3) *E. coli* cells but in the absence of the *hNMT1* plasmid. Control expression cultures were grown in LB

medium supplemented with 100 $\mu\text{g mL}^{-1}$ ampicillin under the same incubation conditions as the engineered construct.

4.2.3 Cell lysis and protein analysis

Frozen cell pellets from the *E. coli* cultures expressing either WT-GBP, RS1-GBP, RS2-GBP, or RS1-His-GBP (no tags), as well as 12-ADA-labeled GBP (12-ADA-GBP, either through RS1 or RS2) and Myristic Acid-labeled GBP (Myr-GBP, either through RS1 or RS2) were lysed using 5 mL g^{-1} lysis buffer (30 mM Tris [pH 8.0], 20 mM NaCl, 1 mM DTT, 1 mg mL^{-1} lysozyme, 1x Halt protease inhibitor cocktail, 0.04 U μL^{-1} benzonase) via sonication, then clarified via centrifugation (12,500 rcf for 20 minutes at 4 °C). The total protein concentration of the clarified lysate was then quantified with a Pierce 660 nm Protein Assay. Normalized concentrations of clarified lysate samples were then analyzed via SDS-PAGE (4-20% Mini-PROTEAN®TGX™ Precast Gels, Bio-Rad, Hercules, CA). Gels were imaged using visible light on the Azure c400 (Azure Biosystems, Inc., Dublin, CA).

To assess whether engineering GBP with an azide tag altered the solubility of the protein, membrane-bound protein fractions of 12-ADA-GBP were lysed using 5 mL g^{-1} membrane lysis buffer ([pH 7.5] 150 mM NaCl, 1% Triton-X-100, 0.1% SDS, 50 mM Tris-HCl, 1 mM DTT, 1mg mL^{-1} lysozyme, 1x Halt protease inhibitor cocktail, 0.04 U μL^{-1} benzonase) via sonication then clarified via centrifugation. Clarified membrane fraction samples were equilibrated with 20 mM HEPES and analyzed alongside clarified lysate samples via SDS-PAGE.

4.2.4 Proof-of-concept selective conjugation of 12-ADA-GBP from lysate

To demonstrate that selective conjugation of 12-ADA-GBP to an alkyne labeled surface is possible, a strain-promoted azide alkyne cycloaddition (SPAAC) reaction was employed with a TAMRA fluorophore conjugated to the strain-promoted alkyne, dibenzocyclooctyne (DBCO). Approximately 45 μL of 0.5 mg mL^{-1} of clarified lysate containing overexpressed 12-ADA-GBP was incubated with 3 μL of 0.5 M iodoacetamide (IAA) for 30 minutes on an end-to-end rotator to prevent disulfide bond formation between free thiol groups on the proteins. Afterwards, 80 μM of DBCO-TAMRA (Click Chemistry Tools, Scottsdale, AZ) was added to the alkylated lysate solution and 20 mM HEPES was added to a final reaction volume of 60 μL . As a negative

conjugation control reaction, Myr-GBP was incubated with the DBCO-TAMRA. Additional negative controls for non-specific binding included uninduced clarified lysate samples of 12-ADA-GBP and Myr-GBP. The reactions were incubated in the dark on an end-to-end rotator overnight at room temperature. After 16 hours, the samples were precipitated via methanol chloroform, resuspended in 4x Laemmli- β ME sample buffer, and analyzed via SDS-PAGE. SDS-PAGE gels were first imaged on the Azure c400 with fluorescent light (Cy3) to investigate selective labeling of 12-ADA-GBP to the TAMRA fluorophore (excitation/emission: 557/583 nm) and then stained with Coomassie and imaged with visible light to reveal total protein distribution in the samples.

4.3 Results and Discussion

4.3.1 Cloning of mglB constructs with NMT sequence

The wild-type and engineered mglB sequences were successfully cloned into pGEM T-Easy and pET15b vectors, respectively. Originally, all sequences were cloned into pGEM T-Easy. However, it was determined that this vector is not suitable for protein expression as it does not contain a ribosomal binding site. Therefore, the engineered mglB plasmids (RS1-mglB, RS2-mglB, RS1-His-mglB) were subcloned into pET15b; this is confirmed by the diagnostic restriction digest analysis in **Figure 4.4** and sequencing alignment analysis (Figure C.1).

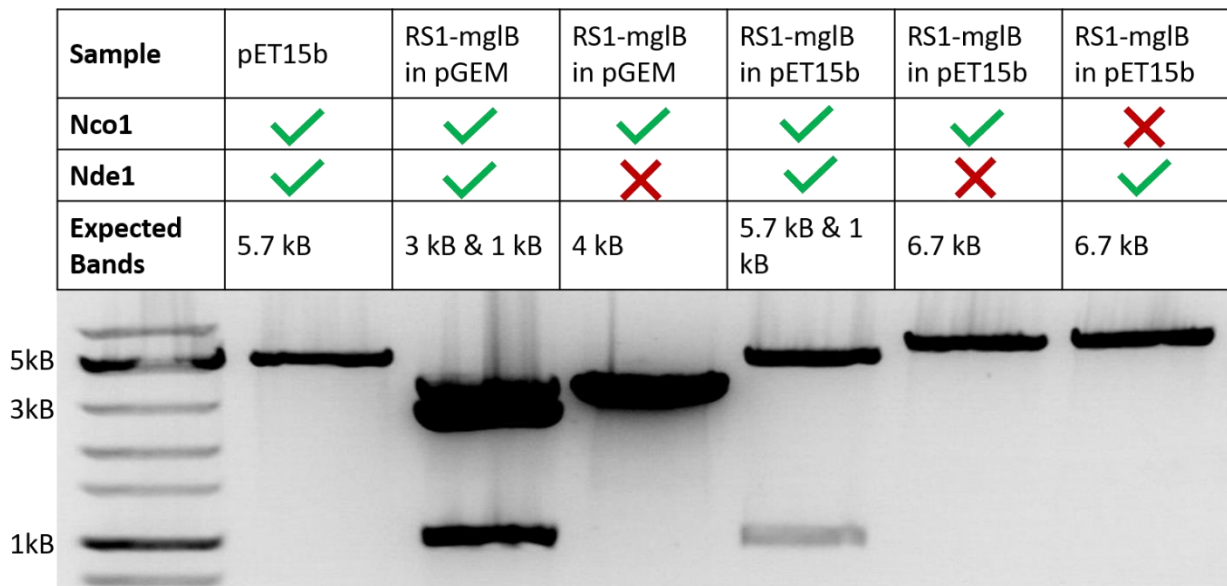


Figure 4.4. Diagnostic restriction digest of successfully cloned RS1-mglB in pET15b vector.

From left to right: pET15b plasmid cut with restriction enzymes Nco1 and Nde1 (5.7 kB expected size corresponds to band location); RS1-mglB in pGEM T-Easy cut with Nco1 and Nde1 (expected sizes of 3 kB for pGEM T-Easy and 1 kB for RS1-mglB insert reflected in banding pattern, with excess un-cut plasmid at 4 kB); RS1-mglB in pGEM T-Easy cut with only Nco1 (expected size of 4 kB for insert + plasmid reflected in band); RS1-mglB subcloned into pET15b cut with Nco1 and Nde1 (expected size of 5.7 kB for pET15b and 1 kB for RS1-mglB insert reflected by banding pattern); RS1-mglB subcloned into pET15b cut with only Nco1 (expected band size of 6.7 kB for insert + plasmid reflected in band); the same RS1-mglB-pET15b construct cut with only Nde1 (expected size of 6.7 kB reflected in band).

4.3.2 Protein expression and bio-orthogonal labeling of GBP

Coomassie-stained SDS-PAGE gels revealed wild-type GBP (WT-GBP), RS1-GBP, and RS1-His-GBP reached peak expression levels within 2-4 hours, indicated by the thick band at approximately 32 kDa compared to the uninduced control samples (Figure 4.5). Thus, engineering the GBP with the N-terminal recognition site for NMT did not alter expression levels compared to the wild type. Similarly, *E. coli* cultures expressing either 12-ADA-GBP (engineered with RS1 or RS2) or Myr-GBP (RS1 or RS2) were analyzed for protein expression with SDS-PAGE. It was observed that at 4 hours, GBP engineered with RS1 had higher expression levels in the soluble fraction than GBP engineered with RS2.

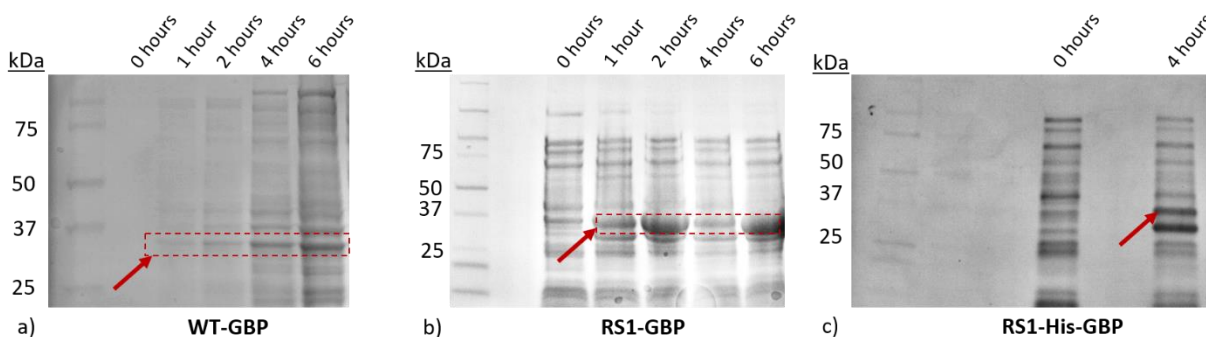


Figure 4.5. Expression levels of WT vs engineered GBP (RS1 & RS1-His) without fatty acid tags (32 kDa).

(a) WT-GBP expression levels for 1-8 hours; (b) RS1-GBP expression levels for 1-6 hours; (c) RS1-His-GBP expression at 4 hours.

Comparison of soluble and membrane fraction protein content from cultures containing overexpressed 12-ADA-GBP (engineered with RS1) demonstrated that the protein of interest was present in both fractions, with a slightly higher abundance in the membrane fraction (Figure 4.6). However, this difference was not significant; thus, it can be inferred that the azide tag does not significantly impact the solubility of the protein. Furthermore, acquiring the protein from the soluble fraction is more efficient and preserves the protein function as no harsh detergents are used. 12-ADA-GBP engineered with the RS2 recognition sequence had similar expression levels in the membrane fraction when compared to GBP engineered with RS1 (Figure 4.7). However, as the RS2-GBP expression levels were negligible in the soluble fraction, the RS1-engineered protein was used for further bio-orthogonal labeling and downstream conjugation steps.

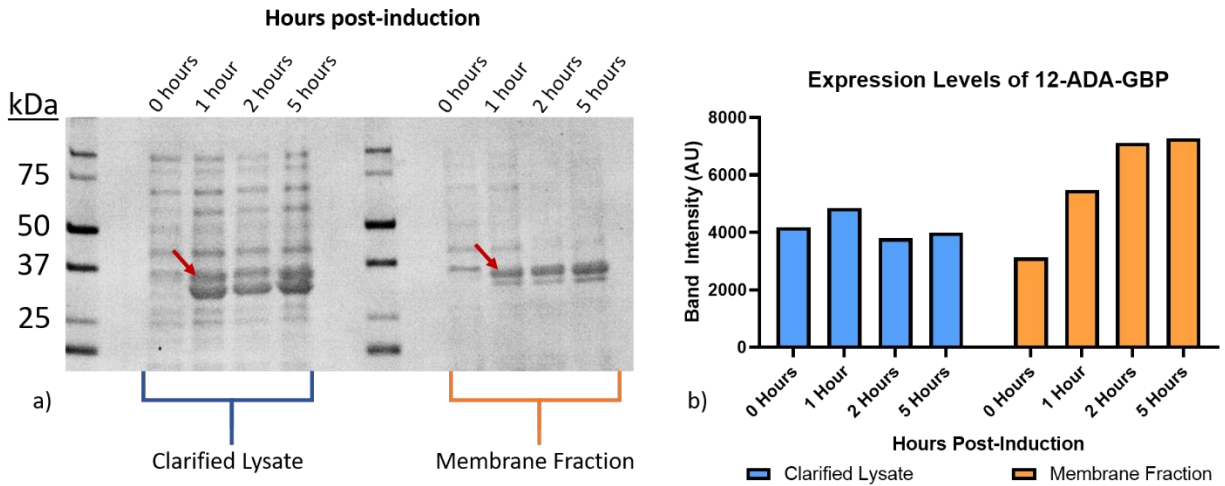


Figure 4.6. Expression of 12-ADA-GBP in soluble and membrane fractions.

(a) Coomassie-stained SDS-PAGE displaying peak expression within 5 hours for 12-ADA-GBP (32 kDa). Banding in clarified lysate is similar to banding in membrane fraction for protein. Membrane fraction contains negligible background protein; (b) ImageJ analysis of band intensity at 32 kDa.

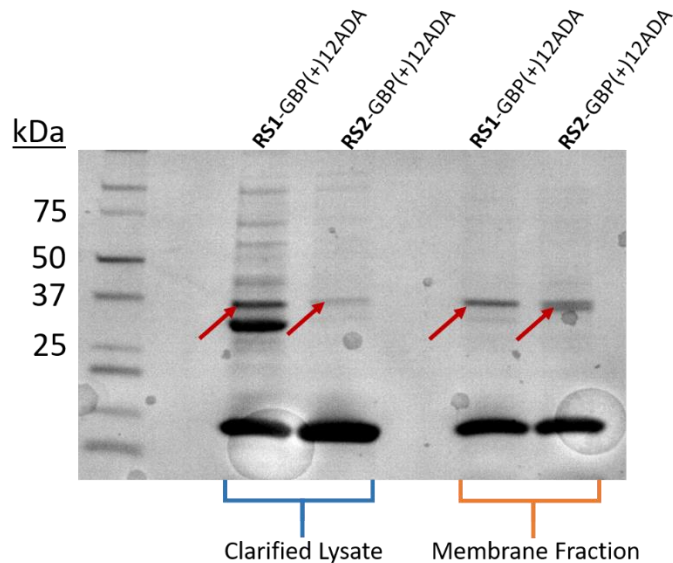


Figure 4.7. Expression levels of 12-ADA labeled GBP (32 kDa) engineered with either RS1 or RS2 recognition sequence in soluble and membrane fractions (5 hours, n=1).

SDS-PAGE analysis of 12-ADA-GBP and Myr-GBP expression compared to the uninduced control revealed peak expression of protein within 2 hours in the soluble fraction. No significant difference was observed in the expression levels for protein tagged with 12-ADA or Myristic Acid (Figure 4.8).

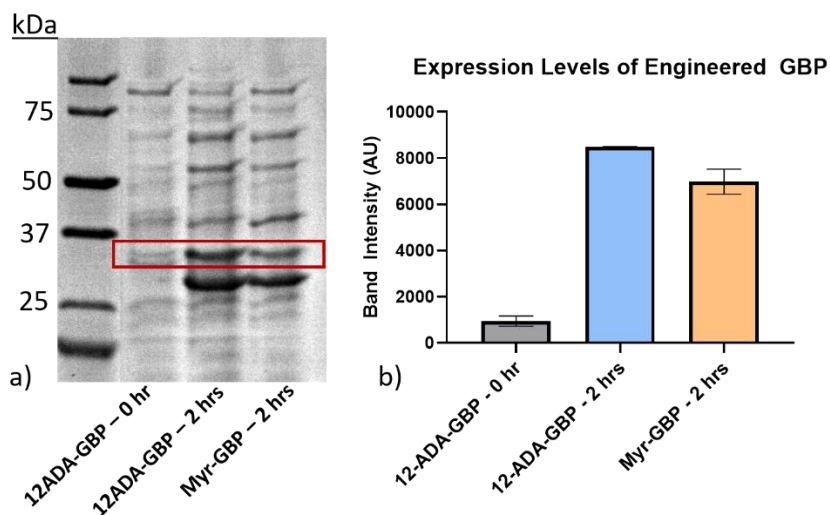


Figure 4.8. Expression of 12-ADA-GBP and Myr-GBP in soluble fraction.

(a) Coomassie-stained gel of uninduced control and clarified lysate collected from 2 hours post-expression containing overexpressed 12-ADA-GBP and Myr-GBP (32 kDa), respectively; (b) ImageJ analysis of band intensity at 32 kDa for all samples.

4.3.3 Selective conjugation of 12-ADA-GBP from lysate

In-gel fluorescence analysis showed that in the entire lane of clarified lysate containing overexpressed protein, only 12-ADA-GBP was successfully clicked with the TAMRA fluorophore, as indicated by the fluorescent band at 32 kDa in Figure 4.9b. As expected, the Myr-GBP sample lane did not display any fluorescent banding. This demonstrated successful selective conjugation of the 12-ADA-GBP directly from clarified lysate.

To demonstrate the functionality of both recognition sites RS1 and RS2, 12-ADA-labeled GBP engineered with both recognition sites was clicked with DBCO-TAMRA directly from lysate and analyzed for fluorescence. Results demonstrated that, as expected, both 12-ADA-GBP samples were able to selectively conjugate to the fluorophore. However, due to the previously observed low expression level of RS2-GBP, the fluorescent band intensity was also much lower for 12-ADA-GBP engineered with the RS2 site (Figure 4.10b).

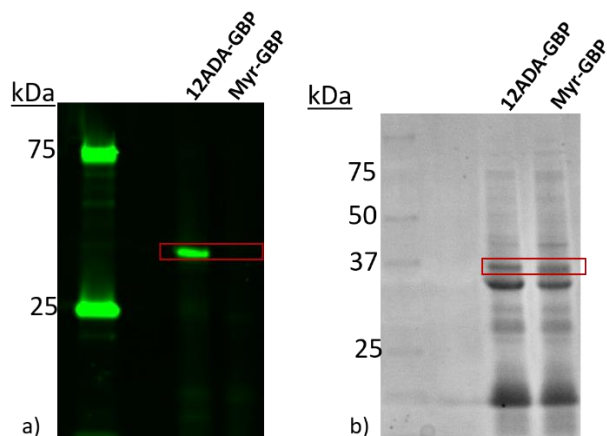


Figure 4.9. Selective conjugation of 12-ADA-GBP from cell lysate via strain-promoted azide alkyne cycloaddition (SPAAC).

(a) Fluorescent image of SDS-PAGE gel containing TAMRA-clicked 12-ADA-GBP and Myr-GBP samples and imaged using the Cy3 channel on Azure c400 gel analyzer. Only 12-ADA-GBP is successfully conjugated to the fluorophore. (b) Coomassie-stained image of the clarified lysate lanes containing overexpressed 12-ADA-GBP and Myr-GBP at 32 kDa, respectively. Both samples underwent SPAAC reactions with DBCO-TAMRA and were precipitated via methanol chloroform before loading on the gel.

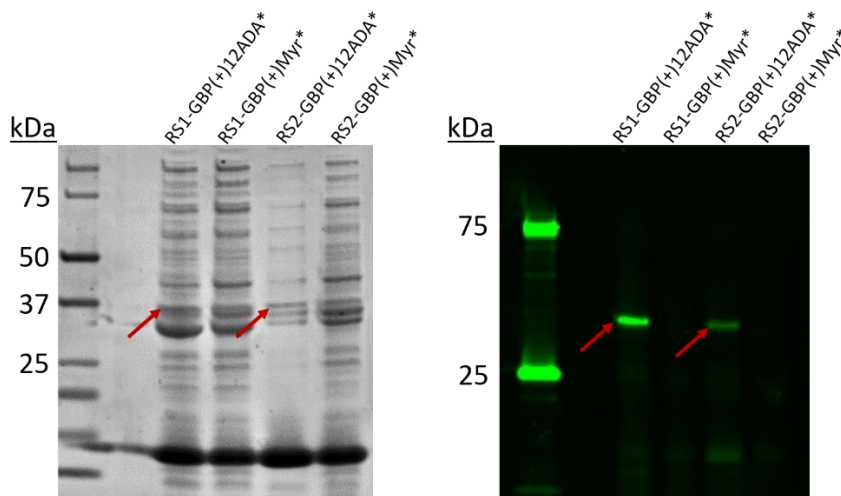


Figure 4.10. Selective conjugation of 12-ADA-GBP (engineered with RS1 and RS2) to DBCO-TAMRA from clarified lysate.

(a) Coomassie-stained gel of clarified lysate samples containing 12-ADA or Myristic Acid labeled RS1-GBP or RS2-GBP clicked with DBCO-TAMRA via SPAAC (32 kDa). Samples were precipitated after SPAAC via methanol chloroform prior to gel loading. (b) Fluorescent image of the same gel analyzed through the Cy3 channel of the Azure c400 gel analyzer demonstrating selective conjugation of 12-ADA-GBP engineered with both RS1 and RS2 NMT recognition sites (32 kDa).

4.4 Future Directions

In this chapter, I demonstrated that chemo-enzymatic labeling of the glucose binding protein was possible within the *E. coli* expression system. The bio-orthogonal appendage of fatty acid analogs 12-ADA and Myristic Acid to the N-terminus of the protein was made possible through the orthogonally co-expressed NMT enzyme. This allowed for streamlined and specific conjugation to cyclooctyne-labeled fluorophore, TAMRA, directly from soluble cell lysate. However, there was a noticeable difference in expression levels and subsequent conjugation efficiency between the GBP samples engineered with the two different recognition sites for NMT. GBP engineered with RS1, the recognition sequence derived from human Calcineurin subunit B, demonstrated consistently stronger expression and labeling efficiency compared to GBP engineered with RS2, the recognition sequence derived from the yeast ADP ribosylation factor. Future work should focus on improving expression conditions for RS2-GBP and examine whether difference in recognition sequence affects the solubility of the protein. As observed in Figure 4.7, RS2-GBP maintained stronger expression in the membrane fraction of the cell compared to RS1-GBP.

4.5 Conclusion

Chemo-enzymatic labeling of substrate proteins within cell expression systems has been successfully demonstrated to streamline conjugation steps and bypass the need for extensive purification. This technique is especially useful for functionalizing recognition elements such as binding proteins to be used in biosensing applications. By eliminating the need for additional purification steps, a greater yield of functionalized protein can be harvested. I have demonstrated that the glucose binding protein can be functionalized with an azide tag from within the *E. coli* expression system, enabling it to be selectively conjugated to alkyne-labeled surfaces directly from cell lysate without additional purification.

5. SELECTIVE CONJUGATION OF GBP TO QUANTUM DOTS

5.1 Rationale

Numerous studies have used fluorescence modalities for GBP-based glucose sensing and have achieved micromolar limits of detection¹⁰⁸. However, a drawback to the currently reported fluorescence-based GBP sensors is the use of organic fluorophores, which are susceptible to photobleaching, are highly sensitive to pH and temperature changes, and possess narrow excitation with broad emission spectra^{11,95}. Thus, photostable nanomaterials such as QDs are a robust alternative⁹⁵. Furthermore, QDs also make for excellent fluorescent donor molecules for FRET since they have broad absorption and narrow emission spectra, owing to a large Stoke's shift. This enables selective excitation of the donor molecule at low wavelengths, which avoids direct excitation of acceptor molecules that contain narrow Stoke's shifts. Hence, I sought to conjugate 12-ADA-GBP to QDs using SPAAC.

5.2 Materials and Methods

5.2.1 Enrichment of 12-ADA-GBP from lysate via anion exchange

Anion exchange chromatography was performed to enrich the concentration of 12-ADA-GBP in the clarified lysate sample prior to conjugation to DBCO-functionalized QDs (DBCO-QDs) to improve SPAAC efficiency by reducing non-specific adsorption to the quantum dot surface. Macro-Prep® DEAE resin (1 mL packed, Bio-Rad, Hercules, CA) was equilibrated with 10 column volumes of wash buffer (10 mM Tris-HCl, pH 8.0) in a 27 mL gravity flow-column (1.5 x 15 cm, Econo-Column® Chromatography Column, Bio-Rad, Hercules, CA). Then, 10 column volumes of (1.0 mg mL⁻¹) clarified lysate containing 12-ADA-GBP was applied to the equilibrated resin and the resulting flow-through was collected. Three 10 mL washes were collected using wash buffer and A280 measurements were taken to ensure protein concentrations reached baseline values. For the elution fractions, 2 mL samples were collected containing the following NaCl concentrations: 0.0, 0.05, 0.1, 0.15, 0.2, 0.4, 0.6, and 0.8 M. Finally, 10 mL of elution buffer (10 mM Tris-HCl + 1.0 M NaCl, pH 8.0) was applied to the column to collect remaining protein bound to the resin. All samples were normalized to concentrations of 0.2 mg

mL⁻¹ using 20 mM HEPES, pH 8.0 (samples below this concentration were not diluted) and analyzed via SDS-PAGE. ImageJ analysis was performed to identify lanes that contained the highest ratio of GBP to total protein. Since the first wash (W1) contained the most enriched fraction of 12-ADA-GBP, this 10 mL sample was concentrated via a 30 kDa molecular weight cut-off (MWCO) Amicon® Ultra-15 mL centrifugal filtration column (5,000 rcf for 30 minutes, Millipore Sigma, Burlington, MA). For immediate confirmation of the protein band in the first wash, the concentrated sample was clicked with DBCO-TAMRA and analyzed on SDS-PAGE. The gel was visualized for fluorescence using the Cy3 channel of the Azure c400 and then stained with Coomassie and visualized under visible light. The concentrated sample was analyzed on SDS-PAGE and the gel was sent to the Purdue Proteomics Facility for protein identification and relative molar abundance of each protein via mass spectrometry (Q-Extractive Orbitrap HF mass spectrometer, ThermoFisher Scientific, Waltham, MA) and intensity-based absolute label-free quantification (iBAQ)

5.2.2 Characterization of amino-PEG quantum dot (NH₂-QD) size (nm) and polydispersity index (PDI)

Amino-PEG coated CdSe/ZnS core/shell quantum dots (NH₂-QDs, 580 nm, 8 μM, Ocean Nanotech, San Diego, CA) were measured for size and polydispersity index (PDI) with a Malvern Zetasizer Nano ZS90 (Malvern, UK). The QDs were resuspended in buffers with pH ranges of 6-8 at either room temperature (25 °C) or 37 °C, with and without Tween-20 (0% or 0.1%), over a period of 48 hours to identify appropriate buffer conditions to minimize aggregation effects. Fluorescence spectra (excitation wavelength of 380 nm) were characterized at 0 hours, 24 hours, and 48 hours using the Synergy H1 Hybrid Multi-Mode Reader (BioTek US, Winooski, VT, USA).

5.2.3 Functionalization of NH₂-QDs with DBCO

The NH₂-QDs were diluted to 1 μM using 20 mM HEPES, pH 8. Diluted QDs were then buffer exchanged via 3 kDa MWCO centrifugal filtration columns (Amicon® Ultra-0.5 mL centrifugation columns, Millipore Sigma, Burlington, MA) with 400 μL of 20 mM HEPES, pH 8.0, to remove sodium azide prior to functionalization. For characterization of QD stability under varying buffer conditions, please refer to Appendix D. After buffer-exchange, 1 μM of the NH₂-

QDs were reacted with a molar excess of sulfo-dibenzocyclooctyne-ester (DBCO-sulfo-NHS, Click Chemistry Tools, Scottsdale, AZ) for 30 minutes at RT in a total volume of 500 μ L adjusted with 20 mM HEPES, pH 8.0. Originally, DBCO-PEG₄-NHS was used as the linker, as PEG improves the solubility of the compound to counteract the hydrophobic property of DBCO. However, as the QDs were already coated with an amino-PEG layer, the PEG linker was redundant and risked increasing steric hindrance due to its size. Therefore, DBCO-sulfo-NHS was chosen due to its smaller molecular weight and solubility of the sulfonate linker. After incubation, the NHS reaction was quenched with the addition of a final concentration of 50-100 mM Tris-HCl, pH 8.0. Excess DBCO was removed via centrifugal filtration using 3 kDa MWCO columns for three washes at 14,000 rcf, 10 minutes each. The DBCO-QDs were then resuspended to a final volume of 500 μ L in 20 mM HEPES, pH 8.0. QD concentration was determined from a standard curve of NH₂-QD fluorescence intensities (ex. 380 nm/em. 590 nm) using the Synergy plate reader. Additionally, NH₂-QD and DBCO-QD sample absorbance spectra (200-350 nm) and fluorescence spectra (ex. 380 nm, em. 500-700 nm) were measured using the microplate reader.

To determine the optimal linker-to-QD ratio for azide reactivity, three samples of varying DBCO:QD molar ratios (100:1, 500:1, 1000:1) were reacted with 1.5x molar excess of Azide-Alexa-647 (Click Chemistry Tools, Scottsdale, AZ) for 4 hours, covered, on an end-to-end rotator at RT. After filtration of excess Alexa dye via 3 kDa MWCO column (three washes using 20 mM HEPES, pH 8.0 at 14,000 rcf, 10 minutes each), the absorbance spectra (200-350 nm) and the fluorescence spectra (ex. 380 nm) of the samples were analyzed. To visualize incorporation of DBCO on the QD surface and the efficiency of the SPAAC reaction between the DBCO-QD and Azide-Alexa-647, 10 μ L of NH₂-QD, DBCO-QD (100:1 to 1000:1 ratios), and all three Alexa-QD samples (normalized to 0.2 μ M QD concentration) were analyzed on a 0.75% w/v agarose gel in 0.5x TBE, pH 8.4 at 150 V for 50 minutes. Samples were combined with Gel Loading Dye, Purple (6X) at a ratio of 10 μ L sample to 2 μ L dye (New England Biolabs, Ipswich, MA). The gel was imaged on the Azure c400 for QD and Alexa fluorescence separately using Cy3 and Cy5 channels, respectively. The images were then overlaid and analyzed for SPAAC efficiency.

5.2.4 Conjugation of 12-ADA-GBP to DBCO-QD via SPAAC

While GBP does not contain any cysteines, non-specific proteins (even in the enriched sample) may contain cysteines that can form disulfide bonds and interact with DBCO moieties¹⁰⁹. Therefore, prior to conjugation to DBCO-QD, 200 μL of enriched protein sample containing the 12-ADA-GBP (0.25 mg mL^{-1}) was incubated with 25 mM of iodoacetamide for 30 minutes at RT. Afterwards, the enriched and alkylated protein sample was added to 200 μL of 0.5 μM DBCO-QDs (500:1 linker-to-QD ratio). Control samples included 0.5 μM NH_2 -QDs reacted with enriched and alkylated 12-ADA-GBP (0.25 mg mL^{-1}) and 0.5 μM DBCO-QDs reacted with alkylated clarified lysate containing Myr-GBP (0.25 mg mL^{-1}). The mixtures were vortexed gently, covered with foil, and incubated at 4 $^\circ\text{C}$ on an end-to-end rotator overnight. After incubation, samples were filtered via 100 kDa MWCO columns for three washes at 14,000 rcf for 10 minutes each using 20 mM HEPES, pH 8.0 to remove excess/unbound protein. The filtered samples were resuspended in 100 μL of 20 mM HEPES, pH 8.0. A Pierce 660 protein assay was used to determine the total protein concentration on the QD surface and in the flow-through samples. The fluorescence intensity values (ex. 380 nm/ em. 590 nm) of the samples were compared to standard QD concentrations to determine QD concentration. Afterwards, Protein:QD molar ratios were calculated (based on molecular weight of 12-ADA-GBP from mass spectrometry analysis). After normalizing protein concentrations (samples with protein concentrations below 0.1 mg mL^{-1} were not adjusted), 10 μL of each sample was prepared and analyzed via SDS-PAGE (150 V for 50 minutes). Control lanes included normalized protein concentrations of enriched 12-ADA-GBP and clarified lysate containing Myr-GBP, as well as DBCO-QD and NH_2 -QD without protein. After imaging the gel for fluorescence via the Cy3 channel on the Azure c400, the gel was stained with Coomassie and imaged using visible light to visualize the protein. The fluorescent image and Coomassie-stained image were overlaid and analyzed to confirm SPAAC conjugation.

5.3 Results and Discussion

5.3.1 Enrichment of 12-ADA-GBP from lysate

SDS-PAGE analysis of flow-through, washes, and elution fractions from anion exchange filtration revealed that most of the protein was lost in the flow-through and W1 according to the

banding pattern at 32 kDa (Figure 5.1a). Some protein was found in the second elution fraction (0.2 M NaCl) but the remaining fractions had faint or very negligible presence of the protein. ImageJ analysis of the intensity ratio of the protein band and the lane revealed that W1 contained a cleaner, more enriched fraction of 12-ADA-GBP (Figure 5.1b).

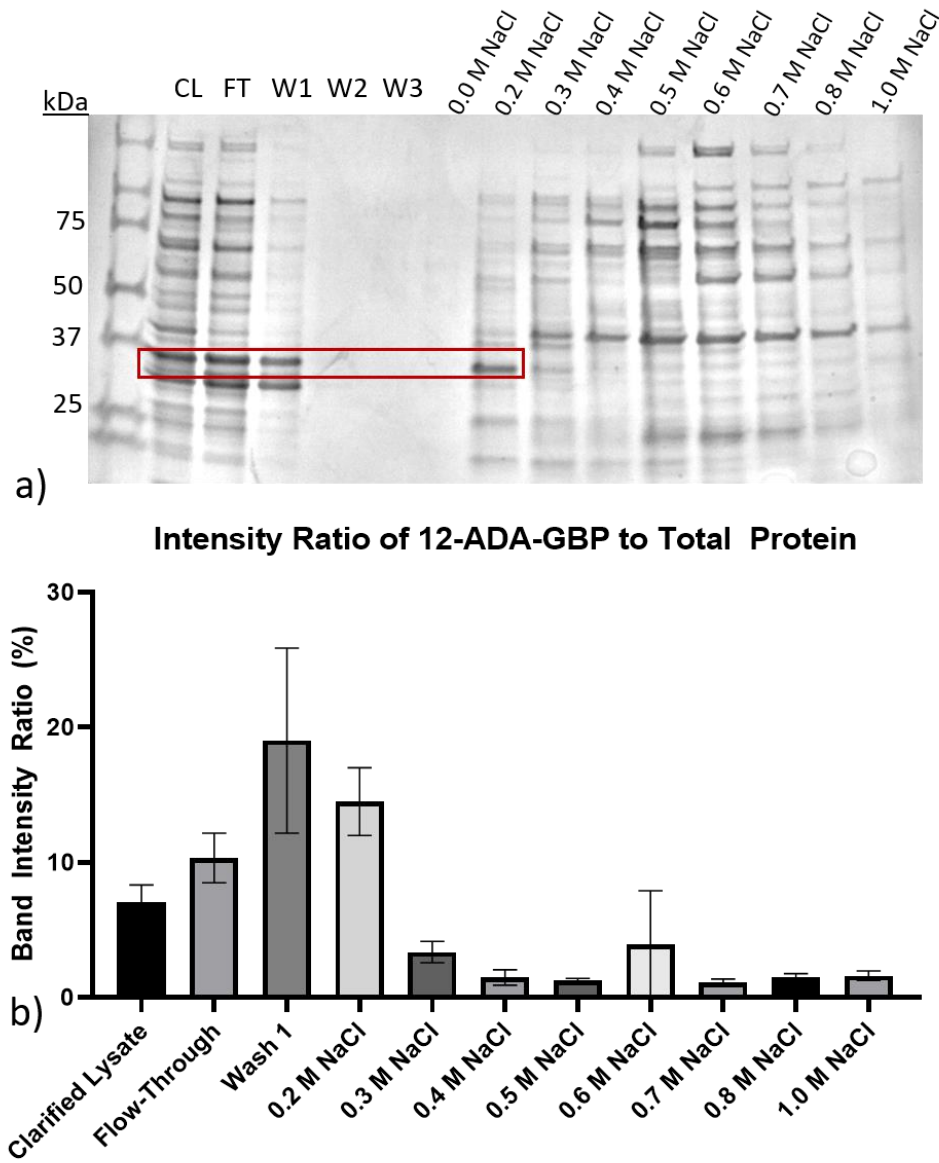


Figure 5.1. Anion exchange enrichment of 12-ADA-GBP from clarified lysate.

(a) Coomassie-stained gel of clarified lysate, flow-through, wash steps, and various elution fractions from the anion exchange filtration of the protein (32 kDa). (b) Intensity ratios of protein band and lane for each sample analyzed via ImageJ (n=3).

Click chemistry of the W1 sample with DBCO-TAMRA confirmed that 12-ADA-GBP was present in the sample (Figure D.1). Thus, prior to conjugation to DBCO-QDs, clarified lysate containing 12-ADA-GBP was filtered through anion exchange to minimize aggregation and adsorption to DBCO by non-specific proteins.

5.3.2 Mass-spectrometry analysis of expressed protein lysate

Mass spectrometry analysis of the clarified lysate sample confirmed that GBP was present in relatively high abundance, as indicated by the second highest peak of iBAQ scores (Figure 5.2b). Furthermore, the mass spectrometry results indicated that the actual size of the GBP protein in this sample was 35.7 kDa, which matches the banding pattern shown in Figure 5.2a. However, at a very similar size (35.3 kDa), another protein, Glyceraldehyde-3-phosphate dehydrogenase A (gapA), is present, although at a lower abundance (Table 5.1). The thick band directly underneath the GBP corresponds to the Malate dehydrogenase protein (32.3 kDa), which is the third most abundant protein in the sample, as indicated by iBAQ peaks. The most abundant protein in this sample is the Outer membrane protein F, visualized by the band directly above GBP at 39.3 kDa. These results confirm that the band indicated by the red arrow corresponds to a mixture of GBP as well as gapA protein, with GBP being the more abundant protein.

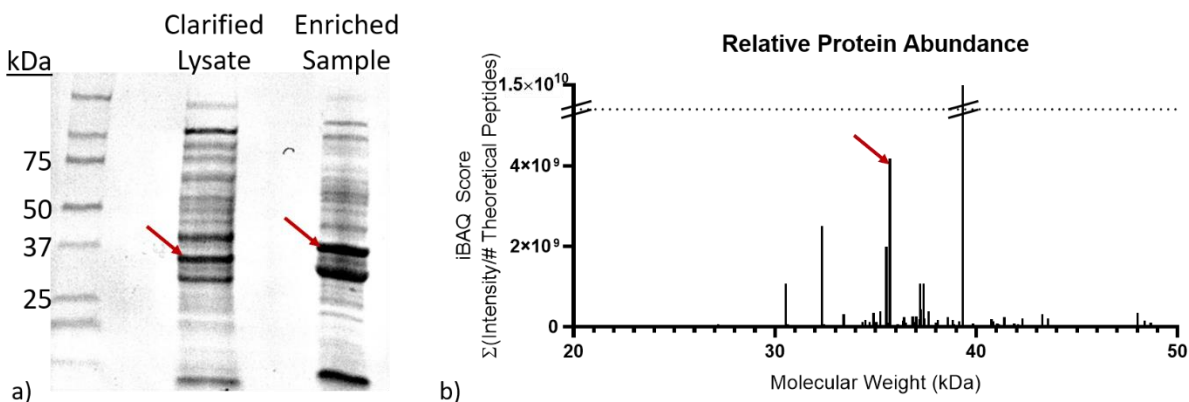


Figure 5.2. Mass spectrometry analysis of protein sample.

(a) Coomassie-stained gel of clarified lysate and enriched sample containing 12-ADA-GBP; (b) Relative protein abundance (represented by iBAQ scores, calculated by the sum of total intensity divided by the number of theoretical peptides for a protein) by molecular weight for clarified lysate sample. Second highest peak corresponds to GBP at approximately 35.7 kDa.

Table 5.1. Identity and size of proteins with highest abundance in overexpressed lysate.

Protein names	Gene names	MW [kDa]	iBAQ Score	MS/MS count
Outer membrane protein F	ompF	39.333	1.59E+10	1091
D-galactose-binding periplasmic protein	mglB	35.712	4.18E+09	365
Malate dehydrogenase	mdh	32.337	2.50E+09	187
Glyceraldehyde-3-phosphate dehydrogenase A	gapA	35.532	1.99E+09	288

5.3.3 Characterization of QD hydrodynamic size (nm) and polydispersity (PdI)

Average hydrodynamic diameter measurements of NH₂-QD were consistently in the range of 68 ± 7 nm, which is more than twice the reported size of these particles (30 nm). Analysis of buffer conditions revealed that higher pH levels (7-8) and inclusion of surfactant (Tween-20, 0.1%) reduced hydrodynamic diameter measurements, but not significantly (Figure 5.3). However, Tween-20 significantly reduced fluorescent intensity of the QDs (Figure D.4). The polydispersity of the QDs was lower with pH 8 and with the inclusion of 0.1% Tween, but this was not consistent at different temperatures. Furthermore, it was observed that after 24-48 hours, the fluorescence intensity is reduced when QDs are stored at higher temperatures (25-37 °C) instead of at 4 °C. Thus, for reduced aggregation effects and preserved fluorescence intensity, buffer conditions for GBP-QD conjugation included higher pH (7-8) levels and reactions were performed at 4 °C.

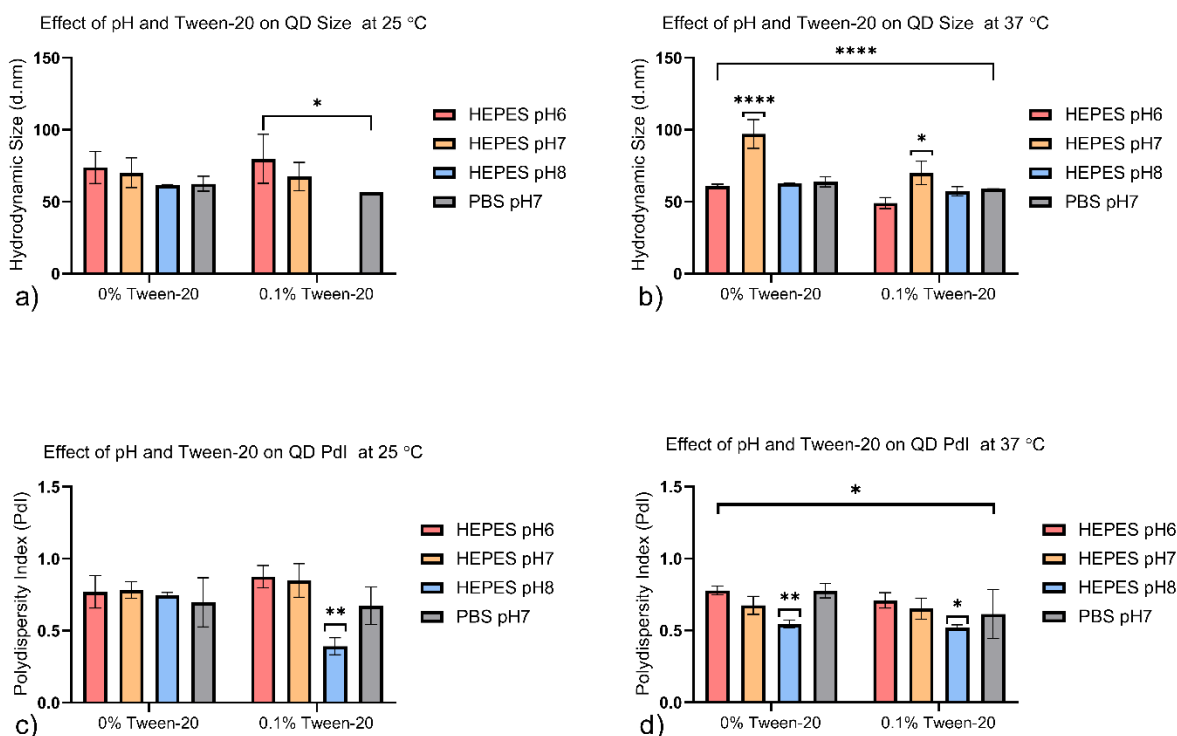


Figure 5.3. Hydrodynamic diameter and polydispersity index (PdI) measurements of QDs in various buffer conditions.

(a) Average hydrodynamic diameter measurements of NH₂-QDs in buffers of pH 6-8, with and without 0.1% Tween-20 incubated at 25 °C for 24 hours (n=3). No significant difference observed in QD size between groups with Tween-20 and without Tween-20. Higher pH levels in samples with Tween-20 reported lower average diameters. Average size measurement for QDs in HEPES pH 8 with 0.1% Tween-20 was excluded due to outlier values above 300 nm; (b) average hydrodynamic diameter measurements of NH₂-QDs in buffers of pH 6-8 with and without 0.1% Tween-20 incubated at 37 °C for 24 hours (n=3). The inclusion of Tween-20 (0.1%) significantly reduced average hydrodynamic diameter ($p < 0.0001$). Samples in pH 7 had significantly higher average hydrodynamic diameters ($p < 0.0001$ without Tween-20; $p < 0.05$ with Tween-20); (c) Average PdI measurements for same samples in (a) (n=3). No significant difference reported for samples incubated with Tween-20 vs. samples incubated without Tween-20; (d) Average PdI measurements for same samples in (b) (n=3). Samples incubated with Tween-20 had significantly lower PdI ($p < 0.05$).

5.3.4 Functionalization of QDs for azide reactivity

QDs conjugated with DBCO had a slightly lower fluorescence intensity than unfunctionalized NH₂-QDs, as observed in Figure 5.4. In addition, DBCO functionalization caused a slight downward shift in the agarose gel, indicating the presence of positive surface charges on the QD (Figure D.2). When reacted with 1.5x molar excess of azide-labeled Alexa-Fluor-647, successful SPAAC was observed with QDs functionalized with 100x and 500x molar excess of DBCO-sulfo-NHS linker (Figure 5.5). Analysis of the emission spectra revealed that at a molar ratio of 500:1 DBCO:QD, there were emission peaks observed for both QD and Alexa-Fluor-647, confirming that this ratio had the highest azide reactivity (Figure D.3). The ratio of 1000:1 did not display successful azide reactivity; this may be attributed to steric hindrance of excess linker that prevented successful conjugation to azide groups. For all future conjugations to enriched 12-ADA-GBP, DBCO-QD with a 500:1 linker:QD ratio was used.

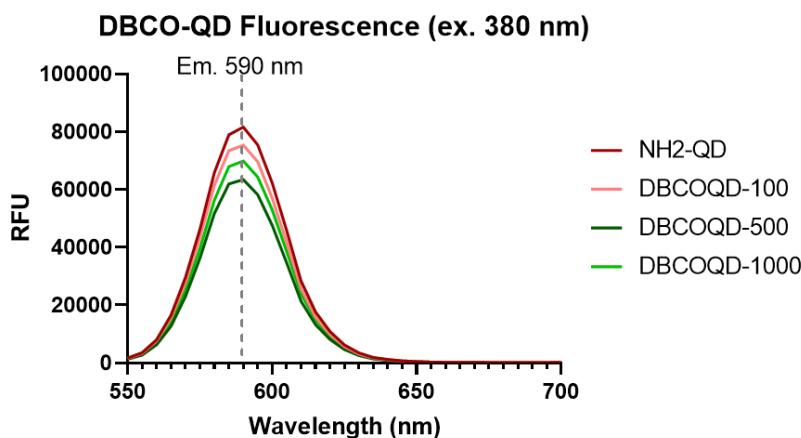


Figure 5.4. Fluorescence emission spectra of QD functionalized with DBCO (excitation 380 nm). NH₂-QDs refer to unfunctionalized amino-PEG-QDs; DBCOQD-100 – 100:1 ratio of linker to QD; DBCOQD-500 – 500:1 ratio of linker to QD; DBCOQD-1000 – 1000:1 ratio of linker to QD.

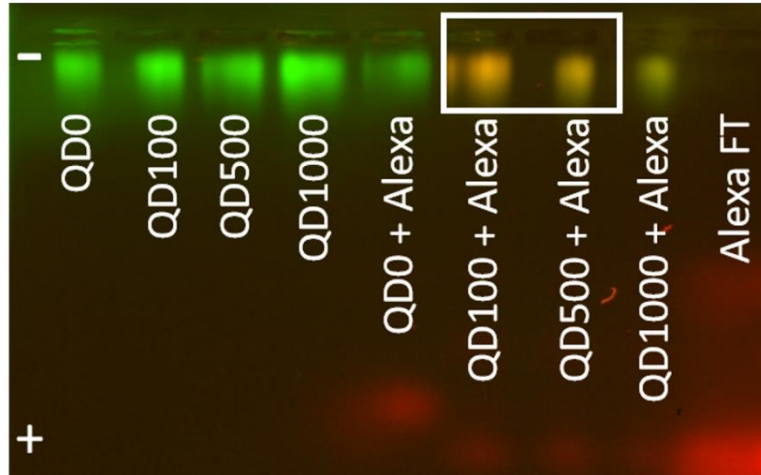


Figure 5.5. Agarose gel electrophoresis analysis of unbound QD and DBCO-QD (green) azide reactivity with Alexa-647 dye (red). QD0-1000 refers to ratio of DBCO to QD (QD0 = no DBCO; QD1000 = 1000:1 ratio). FT = filtrate sample containing only Alexa dye.

5.3.5 Conjugation of 12-ADA-GBP to DBCO-QDs via SPAAC

Enriched 12-ADA-GBP was successfully conjugated to DBCO-QD, as demonstrated by the overlap in Coomassie-stain and fluorescent banding in Figure 5.6. In lane A, which corresponds to the experimental sample containing enriched 12-ADA-GBP and DBCO-QD, a thick band at ~36 kDa was observed; this may represent either excess 12-ADA-GBP or non-specific protein such as gapA. In this sample, a QD concentration of 0.91 μM and a protein concentration of 0.14 mg mL^{-1} was measured. Based on the molar mass of GBP as quantified by mass spectrometry results (35.7 kDa), a molar concentration of 3.92 μM was calculated assuming only GBP made up the protein concentration. Thus, the molar ratio of total protein to QD was estimated to be 4:1. Although all SPAAC reactions underwent extensive wash steps to remove unbound protein, some protein remained in the filtered sample and was only separated from QD with SDS-PAGE. This was only observed in lanes that contained DBCO-QD and protein (A & B), suggesting that the hydrophobic nature of the positively charged DBCO moiety contributed to non-specific protein adsorption to the QD surface, despite alkylation of non-specific cysteine groups with iodoacetamide. In lane C, which contained unfunctionalized NH_2 -QD reacted with enriched 12-ADA-GBP, no non-specific protein bands were observed. The only faint banding observed in the lane corresponded to enriched 12-ADA-GBP protein (36 kDa). Hence, it can be assumed that in addition to alkylation of cysteine groups in non-specific proteins, enrichment of the 12-ADA-GBP

sample is necessary prior to conjugation to DBCO-QD to avoid non-specific protein adsorption to positively charged DBCO moieties that can prevent successful azide-alkyne cycloaddition.

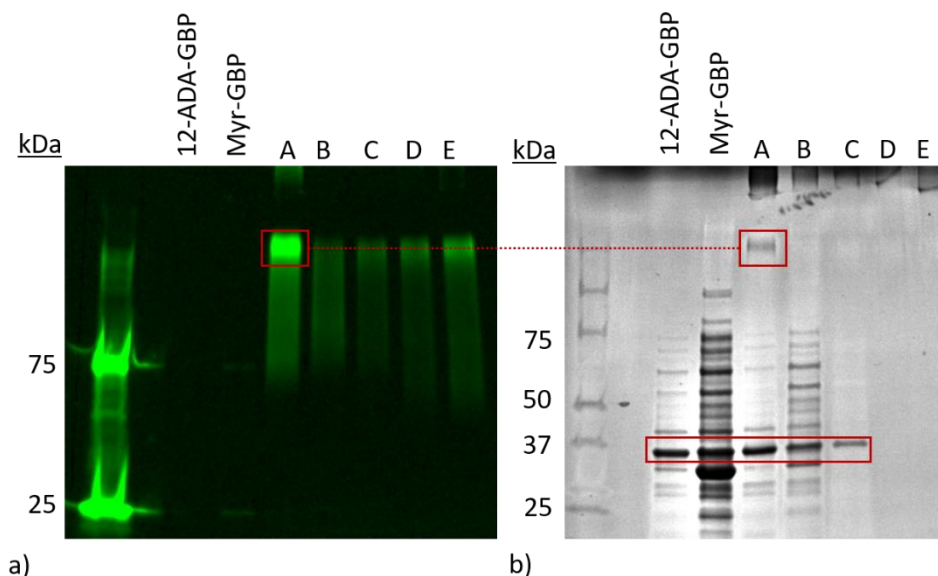


Figure 5.6. Confirmation of GBP-QD conjugation via SDS-PAGE analysis.

12-ADA-GBP and Myr-GBP lanes refer to enriched lysate containing overexpressed 12-ADA-GBP and clarified lysate containing overexpressed Myr-GBP, respectively. A = enriched 12-ADA-GBP reacted with DBCO-QD; B = clarified lysate containing Myr-GBP reacted with DBCO-QD; C = enriched 12-ADA-GBP reacted with NH₂-QD; D = DBCO-QD (500:1 linker to QD ratio); E = NH₂-QD. (a) Fluorescent SDS-PAGE gel imaged with Cy3 channel; (b) the same SDS-PAGE gel stained with Coomassie and imaged under visible light. The red connected rectangles between the fluorescent and Coomassie gel indicate the overlap representative of successfully conjugated GBP-QD. The same band in lane A is not visible in 12-ADA-GBP lane; indicating successful SPAAC conjugation. The red box on the lower half of the Coomassie-stained gel highlights the remaining protein at ~36 kDa indicative of GBP (36 kDa based on mass spec analysis of actual protein size).

5.4 Future Directions

SPAAC has been used to conjugate proteins to QD surfaces but published methods have varied in the type of linker, QD composition, and reaction conditions¹¹⁰. Unlike previously published methods, I sought to conjugate protein directly from enriched clarified lysate, which poses the added challenge of non-specific protein adsorption. There is a tradeoff between high conjugation efficiency and high protein yield, as purification can significantly reduce protein yield but will ultimately reduce non-specific adsorption. While surfactants such as Tween-20 have been previously used to limit aggregation effects, the addition of Tween-20 ultimately did not reduce

non-specific protein adsorption, as demonstrated in control experiments with BSA and DBCO-QD (Figure D.6).

Therefore, for enhanced conjugation efficiency in SPAAC reactions, one should implement a purification step prior to conjugation. This requires high starting concentrations of protein in lysate to counteract potential loss in protein yield. The RS1-His-GBP protein can be labeled with 12-ADA in the expression system and subsequently purified using the 6xHis tag. For all SPAAC reactions, alkylation of cysteine residues in non-specific proteins is required to prevent interaction with DBCO moieties. It is important to note that the maximum concentration of protein in a SPAAC reaction should be under 0.5 mg mL^{-1} , as higher protein concentrations (even if purified) also result in increased protein adsorption to DBCO-functionalized surfaces and can limit SPAAC conjugation efficiency. This also leads to significant aggregation, as demonstrated in hydrodynamic diameter measurements captured by the Zetasizer (Figure D.7). DBCO-QDs reacted with enriched 12-ADA-GBP had significantly reduced average diameters ($100.5 \pm 0.7 \text{ nm}$) compared to DBCO-QDs reacted with clarified lysate containing 12-ADA-GBP ($128.3 \pm 0.6 \text{ nm}$). Despite alkylation, enrichment, and extensive wash steps, there will still be aggregation observed in samples, as demonstrated by the significant size difference in unconjugated QDs vs conjugated QDs ($68.3 \pm 1.3 \text{ nm}$ vs. $100.5 \pm 0.7 \text{ nm}$), owing to hydrophobicity of exposed DBCO and consequently, protein adsorption. Therefore, for accurate size measurements of individual GBP-QD conjugates, transmission electron microscopy (TEM) should be used. TEM will also confirm protein attachment to QD (with negative staining using 2% uranyl acetate) and help to visualize aggregation effects.

Finally, while azide reactivity was proven for QDs functionalized with 100-500x molar excess of DBCO linker, alternative cyclooctyne linkers that offer enhanced solubility should be explored to further reduce adsorption, linker entanglement, and potential aggregation effects. If alternative cyclooctyne linkers for QDs do not reduce aggregation effects, a different fluorescent nanomaterial should be chosen for the biosensor so that CuAAC can be used in place of SPAAC. CuAAC is not suitable for QDs but bypasses the use of extremely hydrophobic linkers and can ultimately reduce the non-specific protein adsorption and aggregation issues. Therefore, immediate next steps should focus on conjugating GBP to an organic fluorophore with an emission spectrum similar to the QD used in this study, such as TAMRA. While organic fluorophores suffer from photobleaching and narrow excitation spectra, they do not require SPAAC conjugation as

most dyes are not adversely affected by copper-mediated click chemistry. If the small Stoke's shift of the organic dye causes direct excitation of the acceptor dyes, then a fluorescent nanomaterial with a larger Stoke's shift that is not negatively impacted by copper-mediated conjugation strategies should be used.

5.5 Conclusion

In this chapter, I have successfully demonstrated that azide-labeled protein from enriched clarified lysate can be selectively conjugated to QDs using SPAAC. I optimized reaction conditions by enriching the lysate sample through anion exchange filtration, alkylating cysteine groups in the enriched sample, functionalizing the NH₂-QDs with a 500x molar excess of DBCO-sulfo-NHS linker, and incorporating multiple wash steps to remove unbound protein. Characterization of QD stability also showed that SPAAC conjugation can be performed at temperature ranges of 4–37 °C, at pH ranges of 7-8 (Figure D.4). While I confirmed SPAAC conjugation of GBP to QD via SDS-PAGE, further analysis should be done to quantify conjugation efficiency, accurately measure the size of GBP-QD conjugates, and estimate GBP to QD ratio.

6. COMPETITIVE FRET-BASED DETECTION OF GLUCOSE USING GBP-QD SENSOR

6.1 Rationale

I sought to integrate the GBP-QD conjugate into a competitive fluorescent glucose biosensing assembly. In the past, FRET has been utilized as a sensing modality for glucose detection using dual labeled GBP. In successful applications, the donor molecule boosted the fluorescence emission of the acceptor molecule upon glucose binding and the ratiometric measurement of the two fluorescent peak intensities distinguished glucose concentrations in the millimolar range¹¹¹. However, this detection scheme was unable to resolve micromolar changes in glucose concentrations due to significantly compromised sensitivity of the protein's modified binding pocket that included an engineered cysteine residue. Because I already conjugated GBP to QDs through the N-terminus, avoiding the protein binding pocket, I decided to take advantage of the competitive binding of GBP to glucose and galactose to design a FRET system based on fluorescently labeled ligand binding. Using an acceptor molecule that can bind and dissociate from GBP would circumvent the issues related to the limited range of motion of the GBP binding pocket (observed in dual labeled GBP). GBP binds to galactose, albeit at a slightly lower affinity ($K_{D,galactose}=1.4 \mu\text{M}$ vs. $K_{D,glucose}=0.35$). Thus, sensor design should maintain high selectivity towards glucose, especially in samples with already low glucose concentrations, such as EBC. Since EBC contains negligible galactose levels, I developed a QD-based FRET sensor design in which galactose is harnessed as a competitively binding fluorescent ligand acceptor (Figure 6.1)^{34,35,39}. The QD emission spectrum should have reasonable overlap with the excitation spectrum of the ligand acceptor for FRET to occur upon GBP binding to the galactose ligand acceptor (and subsequently quench the fluorescence intensity of QD). QDs possess a wide Stoke's shift, which allows for excitation at low wavelengths (< 400 nm). A low excitation wavelength would then selectively excite QDs and not the ligand acceptor. Upon ligand acceptor binding to GBP-QD, the proximity would enable enhanced FRET quenching of QD fluorescence intensity. The addition of glucose to the system would effectively displace ligand acceptor due to the protein's higher affinity for glucose over galactose. Thus, the unquenched QD emission would be proportional to the concentration of glucose. While this has yet to be demonstrated in GBP, similar

mechanisms have been shown in maltose binding protein and sensors for 2,4,6-trinitrotoluene (TNT)¹¹².

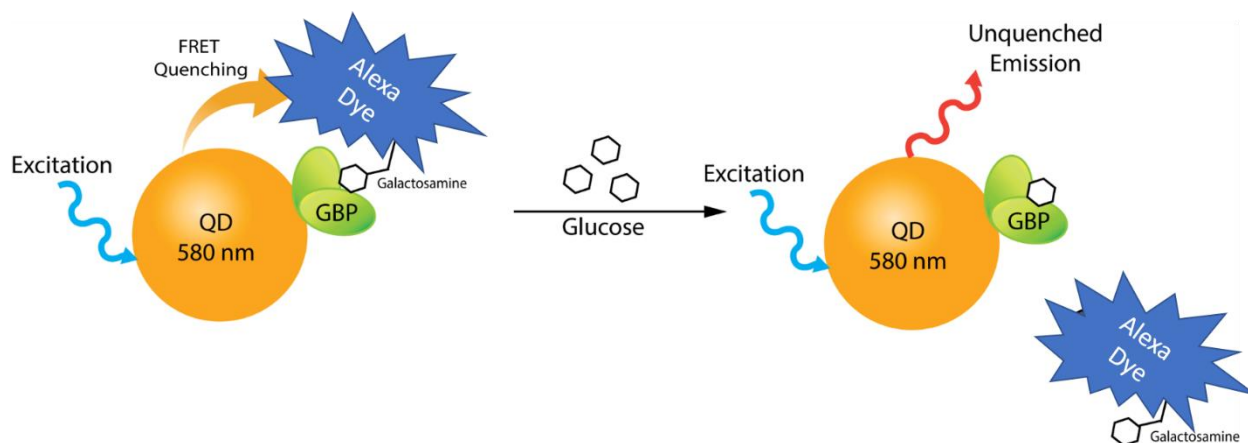


Figure 6.1. Proposed sensor schematic for FRET-based glucose detection system using GBP-QD conjugates and galactosamine-Alexa-633 acceptor.

6.2 Materials and Methods

6.2.1 Synthesis of custom ligand quenchers and fluorophores

Custom ligand acceptors were designed to include either galactosamine or glucosamine conjugated to black hole quencher (BHQ2) or Alexa-Fluor-633 (Alexa-633). The quencher was chosen because its absorbance spectra overlapped with the QD emission spectra and it did not inherently fluoresce at a different wavelength, making it easier to only detect QD emission. Alexa-633 was chosen as the alternate acceptor due to the spectral overlap of Alexa-633's excitation with the emission of the QDs. Compared to Alexa-633 and other organic fluorescent dyes,

For each ligand acceptor, versions with a PEG₆ linker were also designed. According to Borrok *et al.*, GBP preferentially binds to only the β -anomer forms of D-galactose and D-glucose, in which the hydroxy group on the anomeric (C1) carbon is pointing in the same direction as the terminal carbon (C6) (Figure 6.2a)¹¹³.

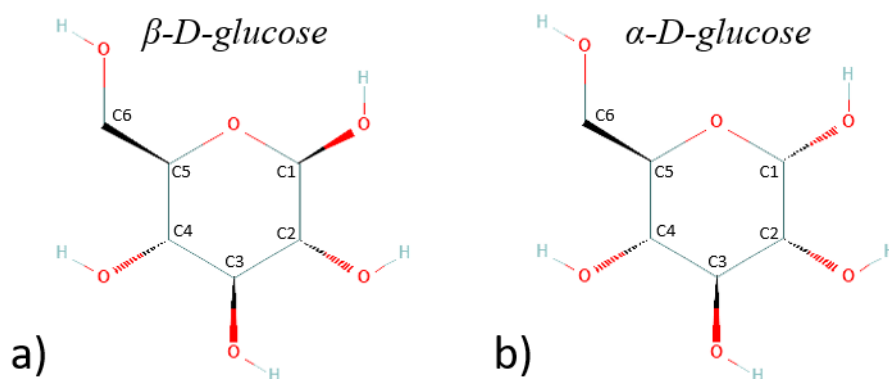


Figure 6.2. Structures of D-glucose anomers. (a) The beta anomer of D-glucose is the preferred substrate for GBP; (b) the alpha anomer of D-glucose.

Hence, the molecules were designed to avoid disturbance of the C1 carbon and have minimal steric hindrance with the binding pocket of GBP (Table 6.1). Complete structures of the four quencher and three fluorophore ligands can be found in Figure E.1-2. It was not possible to design the carbon structures using only the β -anomer, so the structures are a mix of both anomers.

Table 6.1. Ligand acceptor name, purity, and molecular weight (g/mol).

ID	Ligand Acceptor Name	Purity (NMR)	Molecular Weight (g/mol)
Target B	Galactosamine-PEG ₆ -Alexa633	70%	1234
Target C	Glucosamine-Alexa633	70%	940
Target D	Glucosamine-PEG ₆ -Alexa633	90%	1234
Quencher A	Galactosamine-BHQ-2	90%	667
Quencher B	Galactosamine-PEG ₄ -BHQ-2	90%	945
Quencher C	Glucosamine-BHQ-2	90%	667
Quencher D	Glucosamine-PEG ₄ -BHQ-2	90%	945

6.2.2 Calibration of QD-FRET with ligand acceptors

For the GBP-QD system to be sensitive to micromolar changes in glucose, it should be calibrated with the ligand acceptors to identify the highest molar ratio of ligand:QD that does not cause background (non-specific) FRET quenching of QD intensity. Initially, the quencher ligands were added in increasing molar ratios to the unbound QD and analyzed for QD emission intensity

using the Synergy H1 Hybrid Multi-Mode Reader (BioTek US, Winooski, VT, USA) at excitation/emission wavelengths of 380 nm and 590 nm, respectively. Ratios of 10⁻⁷:1 to 10⁻²:1 of quencher:QD were tested in a half area 96-well opaque microplate (QD concentration of 50 nM). Next, the Alexa-633 ligands were added in increasing molar ratios to unbound QD (50 nM) and analyzed for QD emission and Alexa-633 emission when excited at 380 nm (em. 590 nm for QD and em. 645 nm for Alexa-633). In addition, the emission spectra of QD and Alexa-633 at the excitation wavelength of 380 nm was also analyzed in 5 nm increments.

Based on the emission intensity of the QDs with increasing molar ratios of ligand:QD, a range of molar ratios for minimal background FRET was identified. For QD FRET using Alexa-633 ligands, the QD emission intensity was first normalized to peak intensity ratios between QD and Alexa-633 and then normalized according to the QD intensity in the absence of the acceptor (I_D) using the FRET efficiency equation (7), in which I_{DA} is QD intensity in the presence of the ligand acceptor (Alexa-633)¹¹⁴. Two-way ANOVA was performed to analyze the effects of the ligand type and molar ratio on the peak intensity ratio as well as FRET efficiency. A Dunnett's post-hoc multiple comparison test was performed to determine the extent of the significance compared to the control (QD without Alexa-633 ligand). The molar ratio ranges for Alexa-633 and quenchers were compared to determine a suitable ligand that would competitively bind to GBP.

$$E_{FRET} = 1 - \left(\frac{I_{DA}}{I_D} \right) \quad (7)$$

6.2.3 FRET efficiency of ligand acceptors on GBP-QD and unbound QD

After identifying the molar ratio range for minimal background FRET, 25 μ L of freshly prepared GBP-QD conjugates (normalized to 50 nM QD concentration) were plated (in half area 96 well opaque microplate) with 25 μ L of each type of Alexa-633 ligand in the appropriate molar ratio range, mixed, and analyzed for peak intensity ratio and FRET efficiency. As a control, the same molar ratios of unbound QD to Alexa-633 ligand were plated and analyzed.

The excitation wavelength of 380 nm was used for all measurements; QD fluorescence intensity was captured at 590 nm and Alexa-633 intensity was captured at 645 nm. For peak intensity ratio and FRET efficiency measurements, a one-way ANOVA with a post-hoc Dunnett's multiple comparison test was used to determine the effects of bound vs. unbound QD at various

molar ratios on the corresponding FRET signal. In theory, the GBP-QD should demonstrate a lower peak intensity ratio compared to unbound QD, and higher FRET efficiency compared to unbound QD due to increased proximity of the Alexa-633 from ligand binding to GBP.

6.2.4 Glucose-responsive FRET curves using GBP-QD ligand acceptor system

The ligand acceptors that demonstrated a significant impact on FRET efficiency when paired with GBP-QD were used to detect glucose in solution. As there was no difference in the FRET efficiency of GBP-QD when paired with targets B or C between the molar ratios of 0.5, 1, and 2, all three molar ratios were treated as individual replicates. In a full-area 96 well opaque microplate, 50 μ L of each GBP-QD-ligand solution (paired with targets B and C only) was plated. To each well, 50 μ L of D-glucose solution in glucose assay buffer (from the Abnova glucose assay kit) was added (final concentrations of 0.3, 1, and 7 μ M). This was repeated for unbound QD-ligand solutions. Control wells contained either 1) 50 μ L of only GBP-QD and 50 μ L of 20 mM HEPES (pH 7) or 2) 50 μ L of unbound-QD with 50 μ L of 20 mM HEPES (Table 6.2). Wells were briefly mixed and analyzed for fluorescence intensity of QD at excitation/emission of 380 nm/590 nm on the Synergy plate reader. FRET efficiency was calculated for all wells (using control wells as the basis for QD intensity measurements in absence of acceptor) and plotted against glucose concentration for GBP-QD-ligand and unbound QD-ligand systems for both ligand acceptors (targets B and C). A two-way ANOVA with a post-hoc Dunnett's multiple comparison test was performed to determine whether glucose concentration significantly impacted the FRET efficiency of GBP-QD-ligand compared to unbound QD-ligand. It was hypothesized that for the GBP-QD-ligand system, higher glucose concentrations would displace the ligand acceptor and ultimately decrease the FRET efficiency. Conversely, it was hypothesized that for the unbound QD-ligand system, the glucose concentrations would not affect the FRET efficiency, which would stay near baseline.

Table 6.2. GBP-QD ligand glucose detection system and control well components.

Sample Name	GBP-QD-B	GBP-QD-C	QD-B	QD-C	Control 1	Control 2
QD Type	GBP-QD	GBP-QD	Unbound-QD	Unbound-QD	GBP-QD	Unbound-QD
Ligand	Target B	Target C	Target B	Target C	n/a	n/a
Ligand:QD Ratio	0.5, 1, 2	0.5, 1, 2	0.5, 1, 2	0.5, 1, 2	0	0
[Glucose] (μM)*	0, 0.3, 1, 7	0, 0.3, 1, 7	0, 0.3, 1, 7	0, 0.3, 1, 7	0, 0.3, 1, 7	0, 0.3, 1, 7

**Refer to final concentrations of glucose in individual wells of microplate*

This experiment was repeated (twice, $N=2$) for a larger range of glucose concentrations for the GBP-QD and unbound QD system using target C alone. In a 96-well full area opaque (black) microplate, ten 50 μL replicates of GBP-QD with a 1:1 molar ratio of target C were plated. This was repeated for unbound QD samples on the same microplate. To each sample well containing either unbound or GBP-QD along with target C, 50 μL of D-glucose in glucose assay buffer was added to result in final glucose concentrations of 0.0, 0.1, 0.5, 1.0, 5.0, 10, 50, 100, 500, and 1000 μM . Additional control wells contained either 1) 50 μL of only GBP-QD and 50 μL of 20 mM HEPES (pH 7) or 2) 50 μL of unbound-QD with 50 μL of 20 mM HEPES. The plating scheme was repeated for another set of technical replicates in the same microplate. The samples were briefly mixed and subsequently analyzed for QD emission intensity as described in the previous experiment. FRET efficiency was calculated (using control wells as the basis for I_D values) for each sample and plotted against increasing glucose concentrations.

6.3 Results and Discussion

6.3.1 Calibration of QD FRET with acceptor ligands

The QD FRET calibration using unbound QD and the quencher ligands demonstrated a decrease in QD emission intensity with increasing molar ratio of quencher:QD. Although background quenching was reduced, it was done so at an extremely small molar ratio of quencher:QD (Figure 6.3). This was not for glucose sensing because there may not be enough ligand present for competitive binding to GBP.

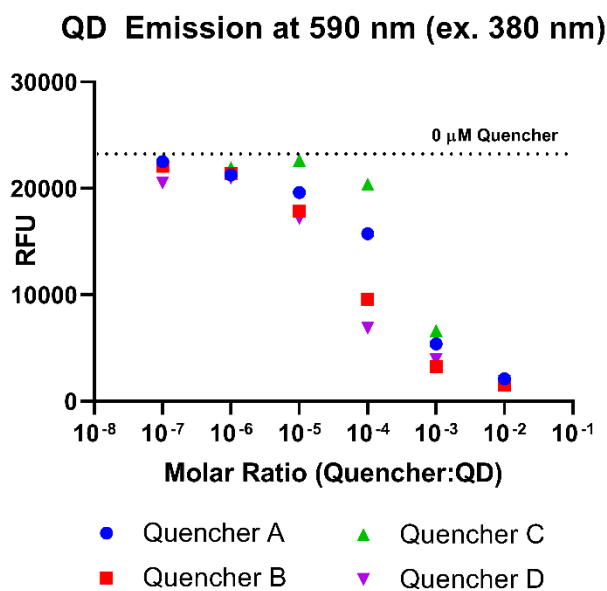


Figure 6.3. FRET quenching of unbound QD with increasing molar ratios of quencher:QD. Dashed line represents average fluorescence intensity of QD in absence of quencher.

Contrary to the quencher FRET results, at similar ratios of the Alexa-633 ligand to QD, there was hardly any quenching of the QDs (Figure 6.4a). A 5:1 ratio did not result in QD emission intensity quenching but there was a noticeable increase in Alexa-633 emission intensity. However, the increase in Alexa-633 was attributed to higher concentrations rather than FRET; this was confirmed by the fact that some Alexa-633 emission still occurs even at an excitation wavelength of 380 nm in the absence of QD (Figure 6.4b). The difference in emission intensity of Alexa-633 in the presence or absence of QD was not significant ($p > 0.05$).

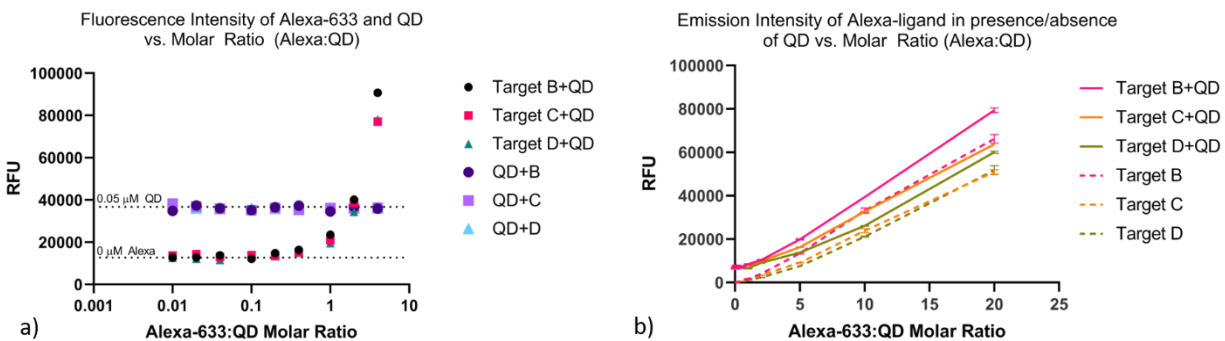


Figure 6.4. Alexa-633 and QD FRET calibration with intensity comparisons.

(a) Independent emission intensity measurements of QD and Alexa-633 ligand targets in presence of each other with increasing molar ratios of Alexa-633 (50 nM QD concentration). (b) Emission intensity measurements of Alexa-633 ligand targets in the presence of QD and in the absence of QD at the same concentrations (plotted as molar ratios to QD concentrations of 50 nM) (n=3).

Peak intensity ratio analysis of Alexa-633 and QD revealed that a minimum molar ratio of 1:1 was required for any significant difference in peak intensity ratios for all targets (Figure 6.5). Unlike the comparison of only QD emission intensity, this analysis also considered the Alexa-633 ligand emission intensity. For plots of peak intensity ratios and emission spectra of QD in presence of Alexa-633 at even higher molar ratios, refer to Figure E.5.

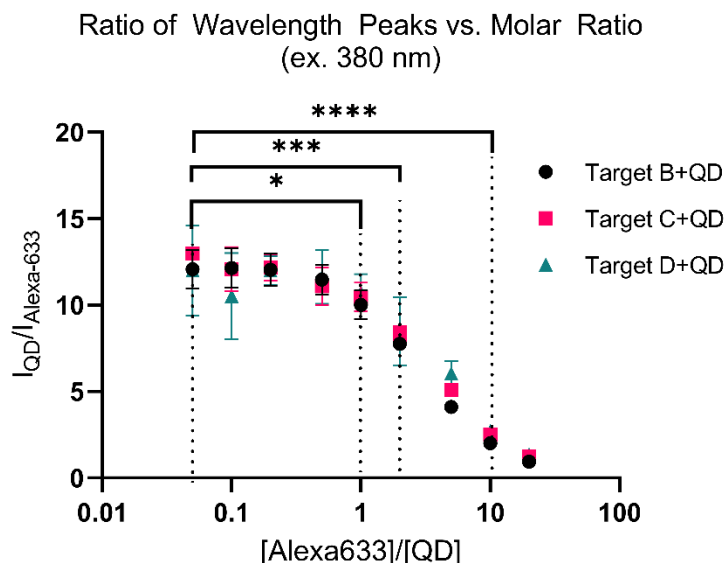


Figure 6.5. Peak intensity ratio of QD and Alexa-633 ligand with increasing molar ratios. A minimum molar ratio of 1:1 was required to generate a significant decrease in peak intensity ratio from the control (p=0.016, n=3).

While peak intensity ratios decreased with increasing molar ratios, it was unclear whether this was due to an increase in Alexa-633 ligand concentration or due to FRET. On the other hand, FRET efficiency analysis revealed that at higher molar ratios (90-200), there is a significant reduction in QD emission intensity (Figure 6.6b). At lower ratios, the FRET efficiency is negligible until a ratio of 10:1 (Figure 6.6a). Therefore, for both peak intensity ratios and FRET efficiency, a molar ratio range of 0.5-5 can be used to calibrate the GBP-QD-Alexa ligand system with minimum background FRET.

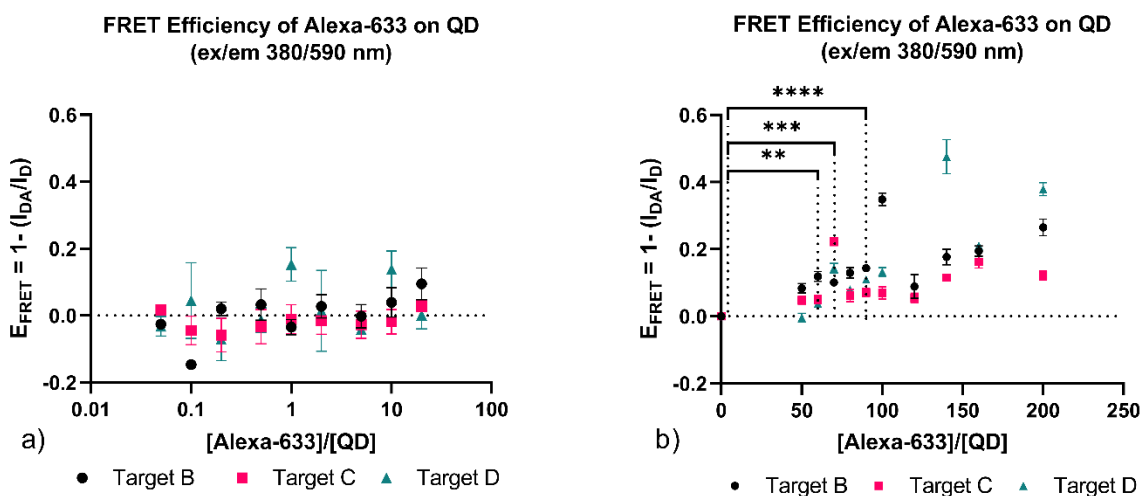


Figure 6.6. FRET efficiency of Alexa-633 ligand targets on unbound QDs at increasing molar ratios.

(a) FRET efficiency of lower molar ratios of Alexa-633 on QD emission intensity (0.05-20). No significant difference in FRET efficiency was observed in any molar ratio combination when compared to QD intensity in absence of ligand; this was confirmed via Dunnett's post-hoc multiple comparison ($p > 0.05$, $n = 3$). (b) FRET efficiency of higher molar ratios of Alexa-633 on QD emission intensity (50-200). A minimum molar ratio of 60:1 demonstrated significant increase in FRET efficiency from the control ($p = 0.005$, $n = 3$).

6.3.2 Comparing FRET signals of ligand acceptors on GBP-QD and unbound QD

Comparison of peak intensity ratios of Alexa-633 and QD for GBP-QD-ligand and unbound QD-ligand systems showed no difference. However, both systems showed significant reduction in intensity ratios with the addition of ligand at 0.5, 1, and 2x molar excess, for all ligand types (Targets B-D) (Figure 6.7).

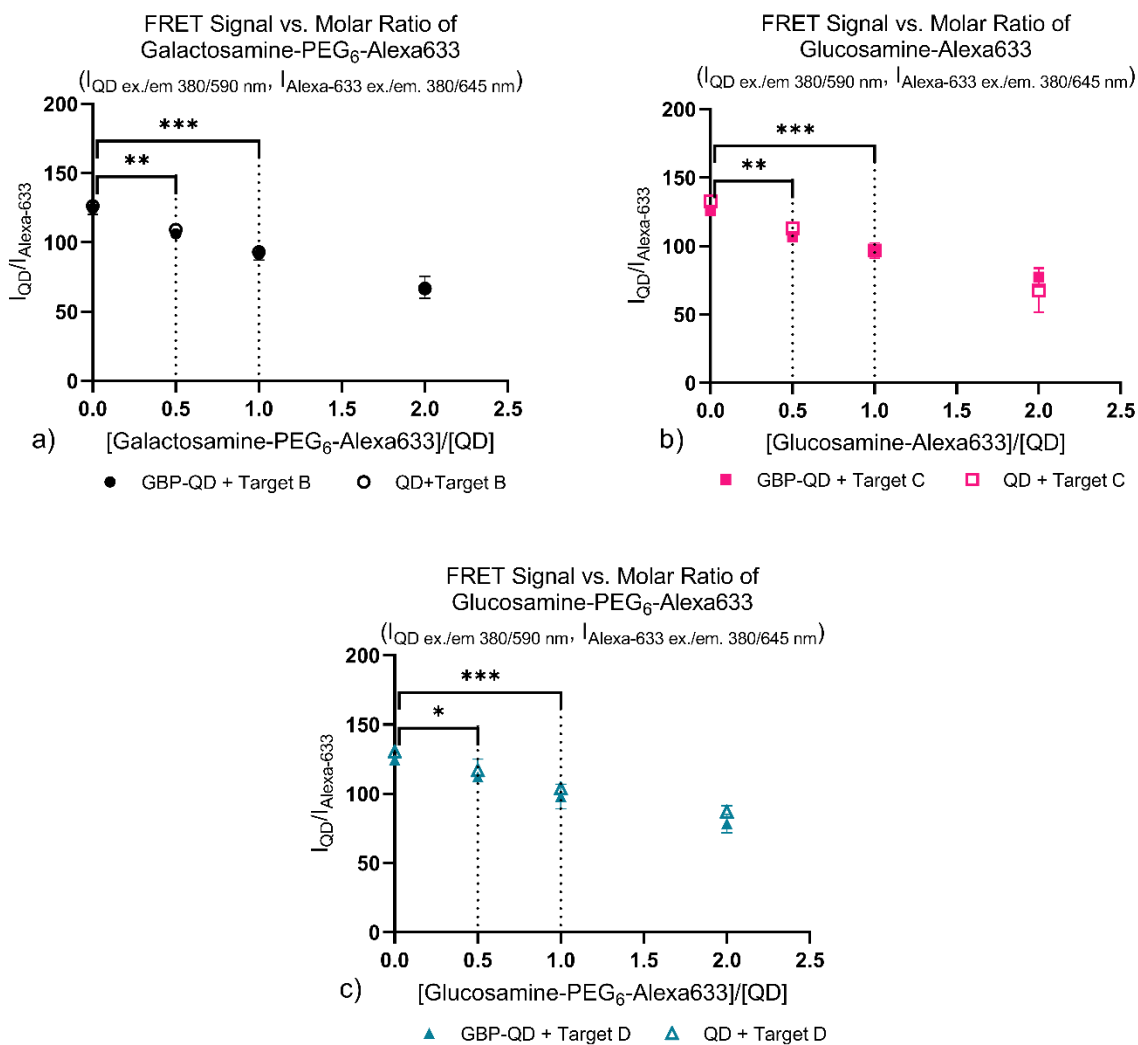


Figure 6.7. Comparison of peak intensity ratios for GBP-QD and unbound QD with increasing molar ratios of ligand acceptors.

(a) Peak intensity ratios of GBP-QD (black filled in circle) and unbound QD (open black circle) with 0.5, 1, and 2x molar excess of Target B ligand (galactosamine-PEG₆-Alexa-633) (n=2). Intensity of QD captured at excitation/emission of 380 nm/590 nm and intensity of Alexa-633 captured at excitation/emission of 380 nm/645 nm. FRET signal ($I_{QD}/I_{Alexa-633}$) significantly decreased with the addition of 0.5x molar excess of Target B (p=0.009) for both GBP-QD and unbound QD; (b) Peak intensity ratios of GBP-QD (pink filled in square) and unbound QD (pink open square) with 0.5, 1, and 2x molar excess of Target C ligand (glucosamine-Alexa-633) (n=2). FRET signal significantly decreased with the addition of 0.5x molar excess of Target C (p=0.005) for both GBP-QD and unbound QD; (c) Peak intensity ratios of GBP-QD (teal filled in triangle) and unbound-QD (teal open triangle) with 0.5, 1, and 2x molar excess of Target D ligand (glucosamine-PEG₆-Alexa-633) (n=2). FRET signal significantly decreased with the addition of 0.5x molar excess of Target D (p=0.010) for both GBP-QD and unbound QD.

There was a marked increase in FRET efficiency for GBP-QD in the presence of the ligand acceptors when compared to unbound QDs at the same molar ratios of Alexa-633:QD (0.5, 1, 2, 5) (Figure 6.8). This difference was not significant ($p=0.06$) for target B (galactosamine-PEG₆-Alexa-633) but was significant for target C ($p=0.0003$). The addition of target D to the GBP-QD and unbound QD systems did not result in any difference in FRET efficiency; the FRET efficiency was high even for unbound QD ($E_{\text{FRET}} = 0.08 \pm 0.13$) (Figure E.6). The average FRET efficiency for GBP-QD across all molar ratios was not significantly different ($p>0.05$); this was also true for unbound-QD. Thus, it can be assumed that the molar ratio range of 0.5-5 for Alexa-633:QD is suitable for detecting ligand binding to GBP.

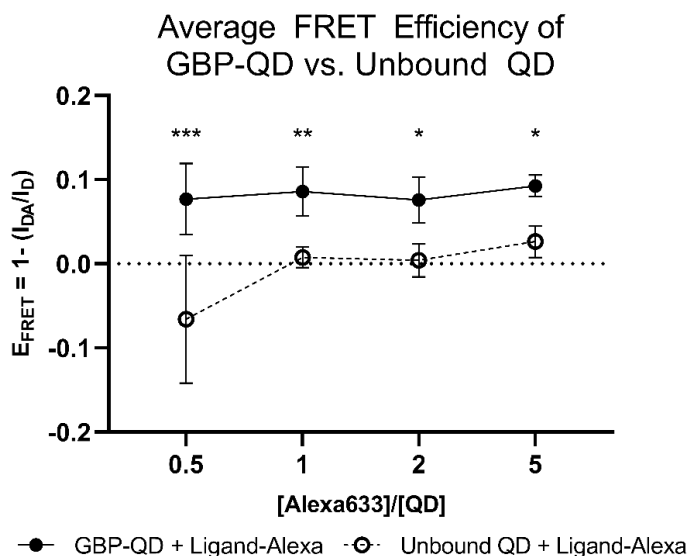


Figure 6.8. FRET efficiency of ligand acceptors on GBP-QD and unbound QD.

Data points indicate pooled average (across all ligand acceptors) FRET efficiency on GBP-QD (closed black circles) and unbound QD (open black circles) emission intensity at increasing molar ratios (0.5-5) of ligand:QD ($N=4$, $n=3$). The average FRET efficiency was greater for GBP-QD compared to unbound QD ($p<0.0001$ for ratio of 0.5, $p=0.006$ for ratio of 1, $p=0.015$ for ratio of 2, $p=0.032$ for ratio of 5).

6.3.3 Glucose-responsive FRET efficiency curves using GBP-QD ligand system

Because the addition of target D resulted in high FRET efficiency for both GBP-QD system and unbound QDs, only targets B and C were used to assess glucose detection. For ligand:QD ratios of 0.5-2, the FRET efficiency for GBP-QD remained consistently higher than that of unbound QD, for target B. The FRET efficiency of the GBP-QD-ligand (Target B) system was

significantly reduced in the presence of 7 μM glucose (Figure 6.9a). No changes in FRET efficiency was observed for the unbound-QD-ligand (Target B) system with the addition of glucose, except for a spike at 1 μM glucose. However, with 7 μM , the FRET efficiency dropped back to baseline; therefore, the spike in FRET efficiency may be attributed to mixing inconsistencies in the well.

There was no change in FRET efficiency observed for the GBP-QD-ligand (Target C) system in the presence of glucose (Figure 6.9b), as it remained consistently above 0.1. For the unbound-QD-ligand (Target C) system, the FRET efficiency was measured to be below zero in the absence of glucose, but significantly increased upon the addition of glucose. When glucose concentrations were increased, there was no significant change in the FRET efficiency, which averaged 0.089 ± 0.035 .

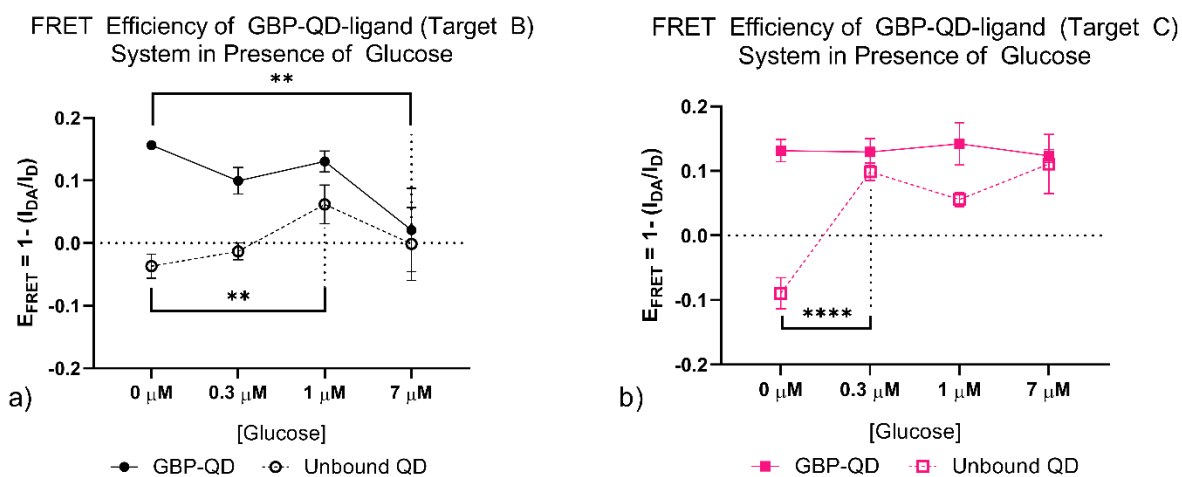


Figure 6.9. FRET efficiency of GBP-QD-ligand system in the presence of glucose (0, 0.3, 1, 7 μM) (n=3).

(a) FRET efficiency of GBP-QD-target B system (using ligand:QD ratios of 0.5-2) compared to unbound QD-target B system in the presence of glucose (n=3). GBP-QD-target B FRET efficiency significantly reduced in the presence of 7 μM ($p=0.0007$). Unbound QD-Target B FRET efficiency spiked in the presence of 1 μM glucose ($p=0.0099$). Significantly higher FRET efficiency was observed for GBP-QD vs. unbound QD ($p<0.0001$). (b) FRET efficiency of GBP-QD-target C system (ligand:QD ratios of 0.5-2) compared to unbound QD-target C in presence of glucose (n=3). No change in FRET efficiency for GBP-QD-target C system with increasing glucose concentrations; significant increase in unbound QD-target C with the addition of glucose ($p<0.0001$).

Upon further analysis of the GBP-QD-ligand (Target C) system in a larger range of glucose concentrations, the FRET efficiency slightly decreased (Figure 6.10) but the difference was not significant. In line with the original hypothesis, the FRET efficiency of the unbound-QD-ligand (Target C) system remained significantly lower than that of the GBP-bound system ($p=0.0012$). Across both QD-ligand systems, the FRET efficiency measurements were highly variable, as illustrated by the standard deviation bars. Furthermore, the FRET efficiency measurements were consistently negative; this may be attributed to a lower QD emission intensity in the GBP-QD/unbound QD sample in absence of the ligand.

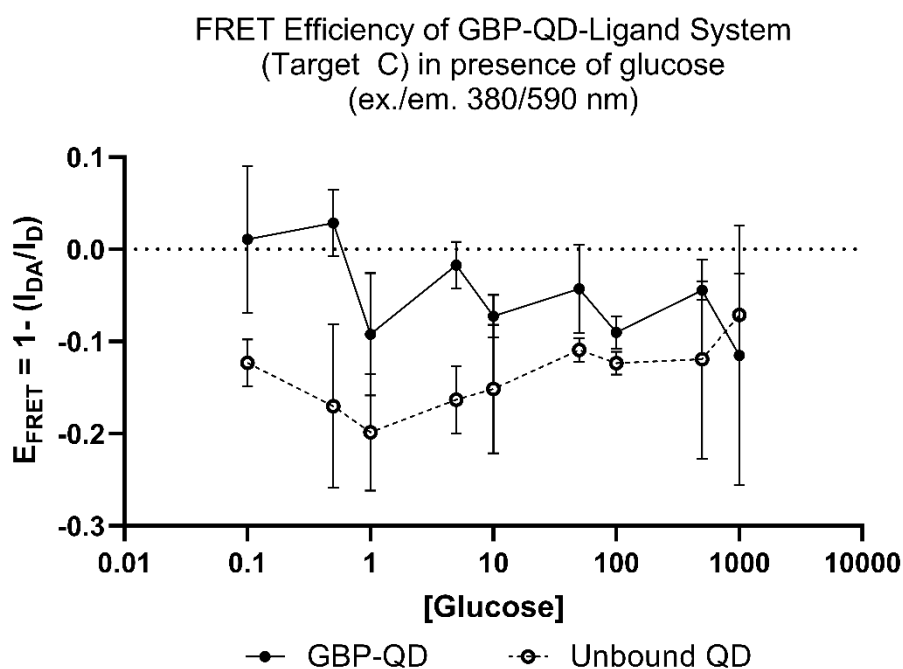


Figure 6.10. FRET efficiency of GBP-QD-ligand (Target C) system in presence of glucose (0.1-1000 μM) (N=2, n=2).

GBP-QD-ligand FRET efficiency (closed circles) was significantly higher than unbound QD-ligand FRET efficiency (open circles) ($p=0.0012$). Difference in FRET efficiency across glucose concentrations was not significant ($p>0.05$).

6.4 Future Directions

6.4.1 Characterization of ligand binding to GBP

FRET efficiency measurements in my preliminary studies are indicative of potential ligand binding to GBP, based upon comparison with unbound QDs. However, quantitative characterization of GBP binding kinetics is needed to confirm this. To this end, several strategies exist to provide quantifiable metrics of protein-ligand interactions, such as the diffusion constant and dissociation constant. Of interest is fluorescence correlation spectroscopy (FCS), which can quantify the mobility of fluorescently labeled ligands (in the presence or absence of their binding partners) in real-time¹¹⁵. Typically, a confocal detection volume, or a pinhole about 0.25-0.5 fl in diameter, is created by focusing a laser to a diffraction limited spot using a confocal microscope with a high numerical aperture. In this volume, the fluorescently labeled ligands exhibit Brownian motion and thus diffuse through the region and produce time-dependent fluctuations in intensity. The mean fluorescence intensity time series of particles is then statistically correlated with itself to generate an autocorrelation function $G(\tau)$, which can quantify the average dwell time, τ_D of the fluorescent particles in the confocal volume. Consequently, the diffusion coefficient, D , can also be derived, and provide quantifiable information about ligand binding. Each of the target ligand acceptors can be analyzed via FCS in the presence of GBP to quantify the diffusion coefficient and select the target to which GBP most effectively binds.

Alternatively, techniques such as bio-layer interferometry (BLI) or isothermal titration calorimetry (ITC) may be utilized for direct estimation of dissociation constant (K_D) for the GBP-ligand system and GBP binding to glucose and galactose¹¹⁶. Of the two, BLI is optimal as it allows for characterization of kinetic rates using ligand acceptors, ligand quenchers, and natural substrates for GBP at low concentrations. However, a drawback to BLI is the requirement for protein immobilization onto the sensor array. To address this, 12-ADA-GBP can be clicked to a biotin linker and immobilized onto streptavidin-coated BLI sensor arrays. After GBP-ligand binding is confirmed through quantifiable characterization techniques, the number of ligand binding pockets per GBP-QD system can be estimated via TEM. GBP-QDs should be negatively stained and fixed onto copper grids prior to TEM characterization to visualize protein distribution on QD surface. The average total protein:QD ratio can be used to further characterize the binding kinetics for the GBP-QD-ligand assembly.

6.4.2 In vitro evaluation of competitive FRET biosensor response

Several performance metrics should be evaluated to characterize the GBP-QD-ligand system's glucose detection performance. According to the Clinical and Laboratory Standards Institute (CLSI) POCT5-A: Approved Guideline, the accuracy, sensitivity, specificity, device stability, calibration, lag time, and trueness of measurement/device traceability are recommended for evaluation of a biosensor. Furthermore, the International Organization for Standardization (ISO) 15197:2003 guidelines recommend evaluating the repeatability, intermediate precision, and analytical accuracy of biosensors¹¹⁷. While the biosensor assembly has yet to be translated into a device, several of these key characteristics can be applied for *in vitro* evaluation.

Although FRET efficiency measurements were used in this study to quantify GBP-QD-ligand binding, the spectral fluorescence distributions should be characterized using appropriate emission filters to generate a thorough illustration of FRET biosensor response to glucose. To this end, preliminary data involving unbound QD and the ligand acceptors illustrate the change in fluorescence spectra with increasing molar ratios of ligand:QD (Figure E.3-4). Furthermore, the calibration quality of the sensor should be improved upon to identify a dynamic range of acceptor:GBP-QD molar ratios that is sensitive to glucose. The results of this study indicated a range of 0.5-5, but a larger sample size of GBP-QD conjugates and FCS-characterized ligand acceptors should be used to confirm this range.

Sensitivity, specificity, and limit of detection should be analyzed for the GBP-QD-ligand system for a wide range of glucose concentrations in the presence of off-target sugar molecules (fructose, maltose, sucrose). Characterization of FRET efficiency, spectral fluorescence distribution, and peak wavelength ratios should be taken into consideration to identify the optimal metric for biosensor signal.

Lastly, the kinetic response, reversibility, and stability of the biosensor should be characterized to determine whether it can be used for long-term use. For kinetic response, the variation in fluorescence signal with time upon step changes in glucose concentrations (increasing and decreasing) should be monitored. The ability of the biosensor to respond to both increases and decreases in glucose concentration determines its reversibility. For step decreases, the sensor should be calibrated with higher concentrations of ligand acceptor to regenerate the FRET-based quenching. For stability, the long-term changes in maximum fluorescence intensity should be evaluated. Preliminary studies characterizing QD stability in various buffer conditions over a

period of 48 hours demonstrated fluorescence stability at higher pH ranges (7-8) when stored at 4 °C. Future studies should focus on evaluating GBP-QD-ligand spectral fluorescence over a longer duration.

Laboratory-grade small molecule detection systems such as liquid chromatography (LC) and high-performance anion exchange chromatograph-pulsed amperometric detection (HPAEC-PAD) are considered the gold standard for the separation of low concentration carbohydrate solutions, including exhaled breath glucose. Therefore, the level of agreement between the biosensor-measured glucose concentration and its true concentration as deemed by HPAEC-PAD or LC should be used to characterize the analytical accuracy of the biosensor. Difference plots and Clarke's error grid analysis (EGA) should be generated to depict system accuracy and deviation-related errors, respectively¹¹⁷.

6.5 Conclusion

In this chapter, I harnessed the competitive binding of GBP to glucose and galactose to design a FRET-based glucose detection system utilizing the GBP-QD. Ligand acceptors were designed to bind to GBP-QD and subsequently be displaced upon the introduction of glucose into the assembly. I characterized the molar ratio range of ligand:QD that was sensitive to ligand binding and demonstrated that FRET efficiency is a reliable metric to evaluate biosensor response. Several opportunities exist to optimize the GBP-QD and ligand combination for sensitive glucose detection, such as characterizing GBP-ligand binding via FCS, and estimating the total number of ligand binding pockets per QD via TEM. However, alternate fluorescent nanomaterials should be evaluated in the case that QDs prove to be challenging for accurate characterization. Future work should model the binding kinetics of the system prior to evaluating sensor performance *in vitro*. After characterization of the system's binding and dissociation capabilities, specific metrics should be used to validate sensor performance, including sensitivity, limit of detection, and kinetic response. This competitive FRET-based biosensor will ultimately enable a non-enzymatic and stable method for sub-micromolar glucose quantification in non-invasive sample matrices such as EBC.

7. CONCLUSION

This dissertation provided an integrated approach to addressing the challenges associated with non-invasive glucose detection exhaled breath condensate. Advances in EBC collection and glucose sensing can enable convenient, non-invasive methods for patients to detect and monitor their glucose levels.

For accurate and reliable platforms for EBC glucose detection, collection methods must be standardized and account for the highly variable nature of glucose dilution from the respiratory fluid to the condensing device. In Chapter 2, I demonstrated that selective collection of respiratory zone EBC using a temperature-based threshold has the potential to limit glucose concentration variability when paired with an effective collection platform, such as the R-Tube. Stricter thresholds may ultimately enrich the glucose concentration in collected condensates due to elimination of additional dilution factors arising from dead space air. In Chapter 3, I assessed the relationship between blood and EBC glucose for normoglycemic and type 2 diabetic subjects through OGTT studies involving the selective condenser. Characterization of EBC glucose with respect to changes in blood glucose shed light on how airway glucose homeostasis rates are reflected in EBC. Opportunities exist to analyze the homeostasis of blood and EBC glucose (from condensates collected selectively and non-selectively) among a larger pool of normoglycemic and diabetic subjects. Additional studies should examine this relationship in subjects with lung inflammation. Ultimately, this selective condenser enables the standardized non-invasive collection of key lower-respiratory analytes and can serve as an important screening platform for lung-related comorbidities.

To address the need for a highly sensitive biosensor for sub-micromolar glucose detection at the point-of-care, I engineered GBP and harnessed its competitive binding properties in a fluorescent glucose biosensor utilizing QDs in Chapters 4-6. The strategies employed for selective conjugation and FRET-based measurements enable streamlined biosensor development with the potential for highly sensitive glucose detection at the sub-micromolar level. To move EBC glucose detection beyond a research tool and into patient-centered point-of-care applications, biosensor integration into an appropriate condensing device will be critical. Long-term stability, reliability, and robustness of the integrated sensor will be required and comparison to gold-standard blood glucose detection is needed to ensure clinical sensitivity and specificity¹.

APPENDIX A. SUPPLEMENT TO CHAPTER 2

Table A.1. Subject details and capnography data signals used to calculate time ratios representative of dead space air to total exhaled volume.

Subject ID	Age (years)	Weight (kg)	Spontaneous Breathing?	Other Ailments?	Signal Quality	T _s (s)	T _i (s)	T _e (s)	Time Ratio
0352_B	53	65	Yes	Yes	Medium	0.3067	1.317	2.443	47.30%
0338_A	64	65	Yes	No	Good	107.3	108.8	111.8	33.30%
0323_C	50	50	Yes	No	Medium	105.2	106.6	111.1	23.70%
0316_C	55	60	Yes	Yes	Medium	5.813	7.05	9.48	33.70%
0151_B	13	37.6	Yes	Yes	Medium	109.1	110.2	113.1	27.50%
0122_A	15	71.4	Yes	No	Poor	109.9	111.9	115	39.20%
0005_A	1	12.8	Yes	No	Poor	101.3	102.2	109.1	11.50%
0128_A	N/A	N/A	Yes	No	Medium	103.6	105.3	111.6	21.30%
0365_B	74	71	Yes	No	Medium	7.857	9.693	13.56	32.20%
0022_D	N/A	N/A	Yes	Yes (Regular Ventilation)	Medium	0.033	1.227	6.91	17.40%
0009_L	4	18.2	Yes	N/A	N/A	17	17.94	19.52	37.30%
0015_L	2	11.6	Yes	N/A	N/A	0.3021	0.9514	1.597	50.10%
0028_L	8	23.9	Yes	N/A	N/A	11.06	12.05	15.65	21.60%
0032_L	N/A	25.9	Yes	N/A	N/A	8.181	9.045	12.81	18.70%
0035_L	N/A	N/A	Yes	N/A	N/A	6.434	7.142	8.052	43.80%
0038_L	3	11.5	Yes	N/A	N/A	9.503	10.55	11.99	42.10%

Note: Adapted from “CapnoBase: Signal database and tools to collect, share, and annotate respiratory signals”, by Karlen, W, Turner, M., Cooke, E., Dumont, G. A., and Ansermino, J. M., in *Annual Meeting for the Society of Technology in Anesthesia (STA)*, West Palm Beach: 2010. p. 25. www.capnibase.org



Figure A.1. Condensation surface for droplets in original prototype of selective condenser.

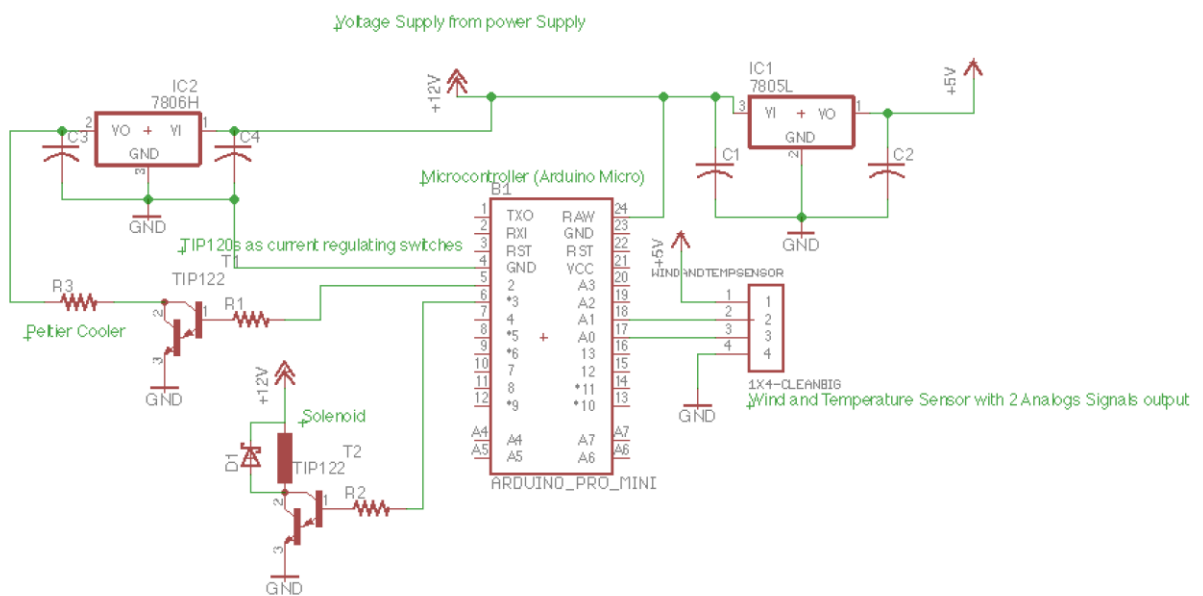


Figure A.2. Printed circuit board (PCB) schematic to integrate wind and temperature sensor, Arduino microcontroller, solenoid valve, and Peltier cooler.

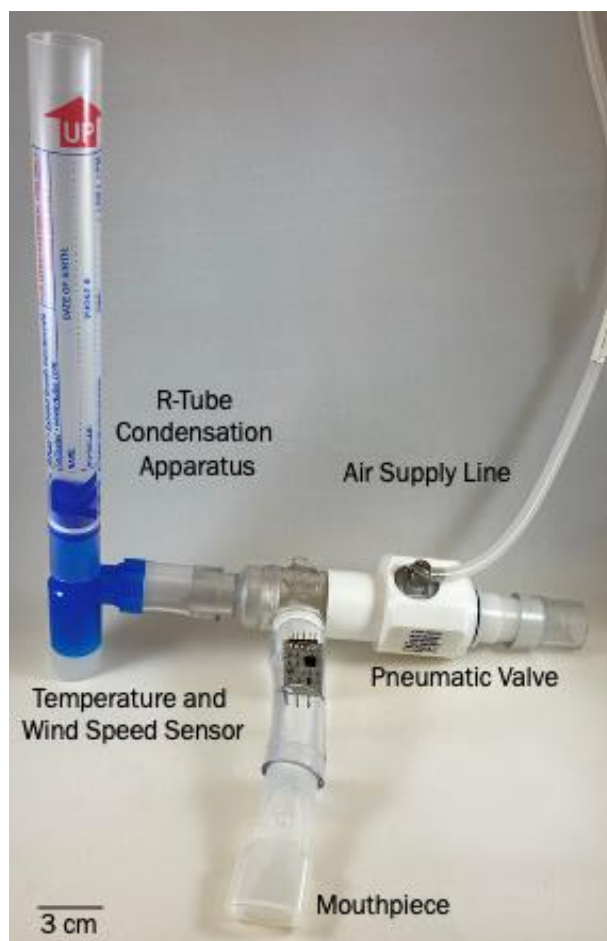


Figure A.3. Selective EBC condenser fitted with R-Tube collection platform (connected to pneumatic balloon T-valve).

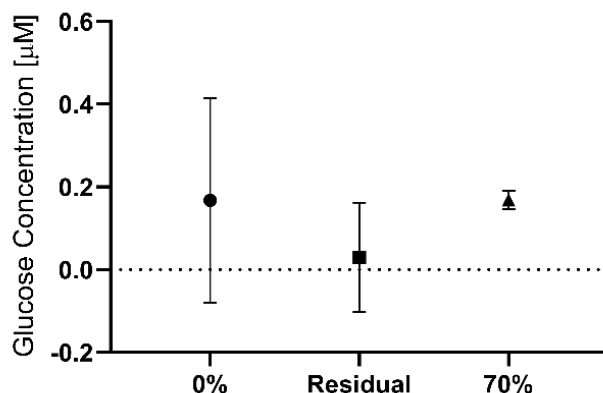


Figure A.4. Average glucose concentrations in samples collected from R-Tube (n=3).

The reusability of the R-Tube following cleaning with 70% ethanol was verified. Three trials for capturing EBC at 0% and 70% temperature threshold levels were performed. Between each run,

the R-tube and breathing apparatus were cleaned using a 70% ethanol rinse followed by a distilled water rinse. A subsequent distilled water rinse was collected and measured for glucose residue along with the 0% and 70% threshold EBC samples. The average glucose concentration following the cleaning procedure is lower than the average EBC glucose concentrations at both the 0% and 70% threshold levels. The high variability in the 0% threshold sample may be attributed to the variable dilution factors introduced by the inclusion of dead space air.

Furthermore, the one outlier in the residual glucose samples may have been due to pipetting errors and efficient mixing of the glucose assay reagents. However, this indicates that the cleaning method employed between runs using the R-tube is suitable and introduces very little residual glucose in the subsequent EBC samples.

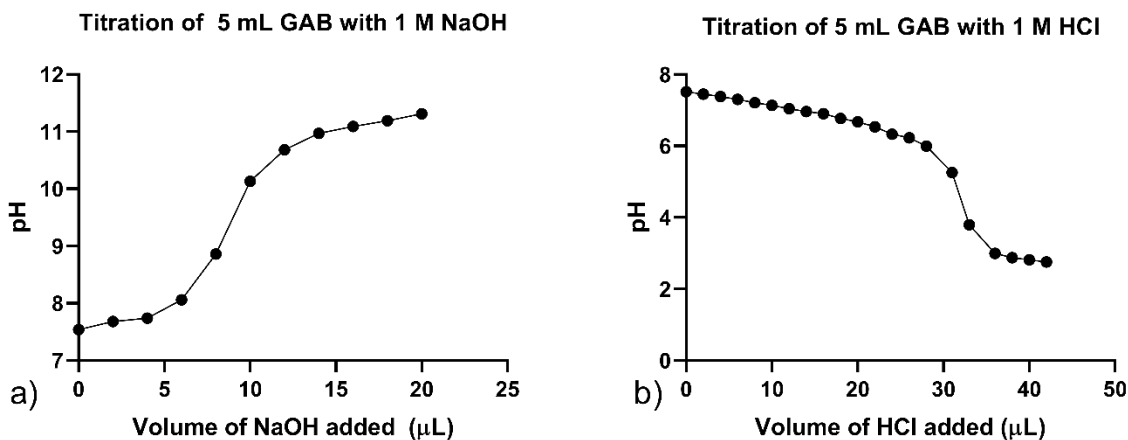


Figure A.5. Titration curves of the glucose assay buffer (GAB) from the Abnova Glucose Assay Kit using (a) 1 M NaOH and (b) 1 M HCl.

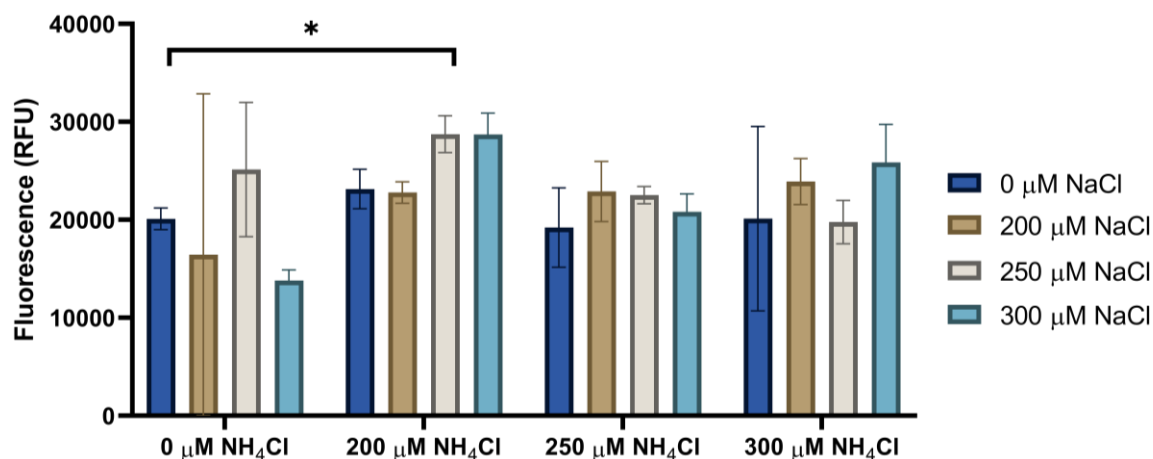


Figure A.6. Combined effects of both NaCl and NH₄Cl on the reported fluorescence intensity of a 0.5 μM glucose solution (n=3).

With the potential of higher ammonia content in selectively collected EBC, we also sought to characterize the effects of salt and ammonia ions on the stability of the glucose assay as well. The total average ionic concentration in an EBC sample is 497 ± 68 (mean \pm SD μM. The most prominent ions found in EBC samples are salts and ammonia. Of this, 229 ± 43 μM is NH₄⁺ and the Na⁺ concentration is averaged at 242 ± 43 μM¹¹⁸. The stability of the assay was tested in presence of a combination of salt (NaCl) and ammonia (NH₄Cl). Serial dilutions were done with MilliQ water to obtain 200 μM, 250 μM and 300 μM of each NaCl and NH₄Cl. Glucose concentration range found in the exhaled breath condensate sample for a healthy subject was between 0.20 μM 1.20 μM¹¹⁹. Hence, 0.50 μM glucose solutions were made using D-glucose (MW 180.15 g/mol) and MilliQ water. Using the glucose assay kit (Abnova, Taipei, Taiwan), each solution was assayed in triplicate volumes of 50 μL and relative fluorescence intensity values were captured using an excitation/emission wavelength pair of 540 nm and 590 nm. The results upon mixing NaCl and NH₄Cl into a glucose-containing sample demonstrate that there is no significant difference in the reported fluorescence intensities over varying concentrations of NaCl in the presence of ammonia. However, the same does not hold true for NH₄Cl in the presence of NaCl. The results obtained from two-way ANOVA followed by a post-hoc Dunnett's multiple comparison test show a p-value of 0.01 and hence a significant difference between the control (0 μM of NH₄Cl) and 200 μM of NH₄Cl. Since no trend is observed to suggest that a higher concentration of NH₄Cl is correlated with changes in the reported fluorescence intensity of the assay for a given concentration of glucose, the effect observed can be attributed to sources of error due to pipetting or inconsistent auto-gain adjustments between the measurements.

APPENDIX B. SUPPLEMENT TO CHAPTER 3

Table B.1. Inclusion and exclusion criteria for OGTT pilot study subject selection.

Inclusion Criteria	Exclusion Criteria
Age 20-75 years	Active or chronic systemic illness, not including type 2 diabetes
Lean (BMI <25 kg/m ²) non-diabetic	Active malignancy
Obese (BMI >30 kg/m ²) diabetic	Active psychiatric disease
Type 2 diabetes, defined by typical obesity-associated DM with age of onset over 20, without evidence of rare forms	Smokers
Fluent in English	Current pregnancy (female participants)

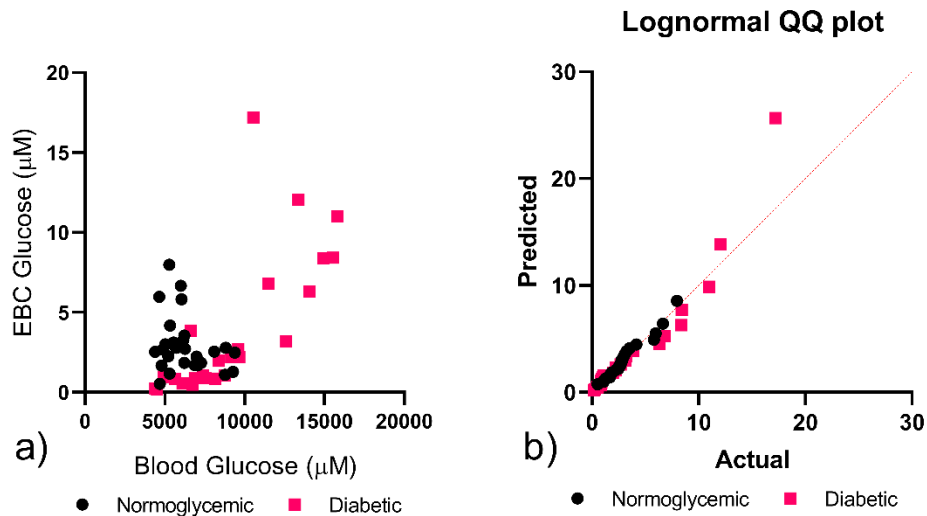


Figure B.1. Assessing normality of EBC and blood glucose relationship for all data points (normoglycemic- N=2, n=19; diabetic – N=2, n=24).

EBC glucose was plotted against blood glucose profiles for both diabetic and normoglycemic subjects (a) and assessed for normality with a lognormal QQ plot (b). This suggests that the data is normally distributed after a logarithmic transformation (did not pass Shapiro-Wilk’s normality test with un-transformed values).

APPENDIX C: SUPPLEMENT TO CHAPTER 4

Table C.1. Deep Vent high fidelity polymerase chain reaction protocol for wt-mglB.

Deep Vent PCR Protocol - WT

Reaction Volume	25	50
Reagent	Volume(μ L)	
ThermoPol Reaction Buffer (10X)	2.5	5
dNTP Solution Mix (10 mM)	0.5	1
Upstream Primer (10 μ M)	1	2
Downstream Primer (10 μ M)	1	2
DNA (50 ng/ μ L)	1	2
Deep Vent DNA Polymerase	0.25	0.5
DMSO (100 mM)	0.5	1
Nuclease-free water	18.25	36.5
Total Volume	25	50

Heating Protocol

	Condition	Temperature	Time
	Initial Denature	95	2 min
Cycles = 32	Denature	95	30 sec
	Annealing	51	1 min
	Extension	72	1 min
	Final Extension	72	5 min
	Store	4	∞

Table C.2. Primer designs for engineering mglB with NMT recognition sequence.

Primer ID	Description	Sequence	Length (bp)	TM (°C)	GC %	Notes
DT005F	GBP-Fwd Nco1RS1mglB	GGAGGCCATGGGTAACGAAGCGTC TTACCCGCTGatgAATAAGAAGGTG TTAAC	54	69.2	50	Forward Primer for RS1- mglB
DB-002F	GBP-Fwd Nco1RS2mglB	GGAGGCCATGGGTCTGTTCGCGTCT AAAatgAATAAGAAGGTGTTAAC	48	66.8	45.8	Forward Primer for RS2- mglB
DB-001F	GBP-Fwd Nco1RS1- His-mglB	GGAGGCCATGGGCGTCTTACCCGC TGCATCACCATCACCATCACatgAAT AAGAAGGTG	59	71.8	54.2	Forward Primer for RS1- His-mglB
DT006F	GBP-Fwd Nco1RS2- His-mglB	GGAGGCCATGGGTCTGTTCGCGTCT AAAGGTGGGCATCACCATCACCAT CACatgAATAAGAAGGTGTTAAC	76	71.3	50	Forward Primer for RS2- His-mglB
DT007F	GBP- FwdNco1mglB	GGAGGCCATGGatgAATAAGAAGGT GTTAAC	31	60.4	45.2	Forward Primer for wt- mglB
DT005R	GBP-Rev NdeImglB	GCTCCTCATATGTTATTTCTTGCTG AATTCAGC	33	59.4	39.4	Reverse primer for mglB
DT013F	GBP-Fwd pET15b	CGATCCCGCGAAATTAATACG	21	53.9	47.6	Backbone of pET15b vector ~80-90bp away from Nco1 Restriction site
DT013R	GBP-Rev pET15b	CCTCCTTTCAGCAAAAAACCC	21	54.7	47.6	Backbone of pET15b vector ~100 bp away from Nde1 Restriction Site

Table C.3. Deep Vent high fidelity PCR protocol for RS1 and RS2-mglB.

Deep Vent PCR Protocol - RS1 and RS2

Reaction Volume	25	50
Reagent	Volume(μL)	
ThermoPol Reaction Buffer (10X)	2.5	5
dNTP Solution Mix (10 mM)	0.5	1
Upstream Primer (10 μ M)	1	2
Downstream Primer (10 μ M)	1	2
DNA (50 ng/ μ L)	1	2
Deep Vent DNA Polymerase	0.25	0.5
DMSO (100 mM)	.5	1
Nuclease-free water	18.25	36.5
Total Volume	25	50

Heating Protocol

	Condition	Temperature	Time
	Initial Denature	95	2 min
Cycles = 32	Denature	95	30 sec
	Annealing	41	1 min
	Extension	72	1:30 min
	Final Extension	72	5 min
	Store	4	∞

Table C.4. DNA double-digest protocols for pET15b and RS1-mglB.

Component	Volume
DNA	Entire volume of PCR cleanup (31 or 16 μ L)
10x NEB buffer 3.1	Either 3.7 or 2 μ L (1x dilution)
NcoI-HF	1.0 μ L
NdeI	1.0 μ L
Nuclease-free Water	Either 0.3 or 0 μ L (to total of either 37 or 20 μ L)

Table C.5. Plasmid/gene ligation protocols for experimental and control samples.

Reaction	Insert (μ L)	Vector (μ L)	T4 Ligase (μ L)	Buffer (μ L)	Water(μ L)	Notes
L1	1.2	2	1	5	0.8	3:1 Molar Ratio
L2	1	1	1	5	2	5:1 Molar Ratio
C1	--	1 (uncut)	--	5	4	Transformation Control
C2	--	1 (cut)	--	5	4	Digestion Control
C3	--	1 (cut)	1	5	3	Re-ligation Control
C4	--	--	1	5	4	Negative Control

Note: Example for 10 μ L ligation reactions (10.5 ng/ μ L of mglB PCR clean-up and 11.9 ng/ μ L of pGEM T-Easy vector).

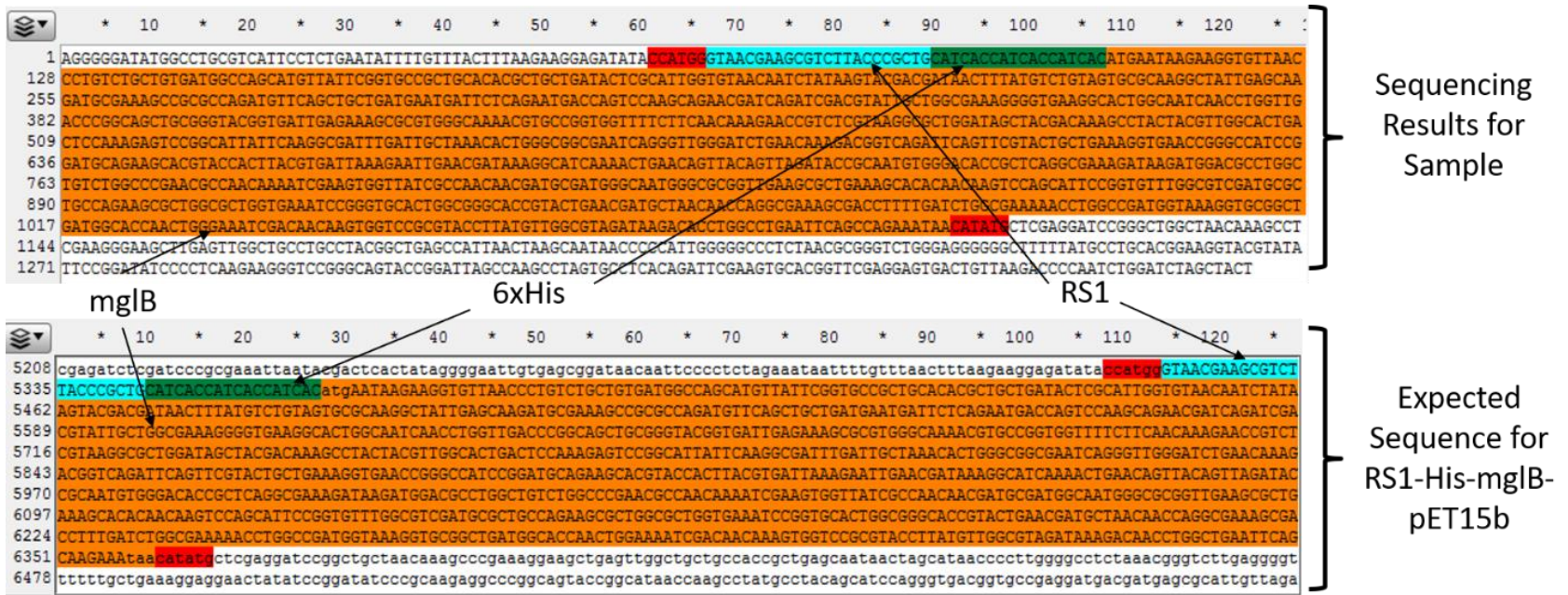


Figure C.1. Sequencing results confirming successful cloning of RS1-His-mgIB into pET15b vector.

APPENDIX D. SUPPLEMENT TO CHAPTER 5

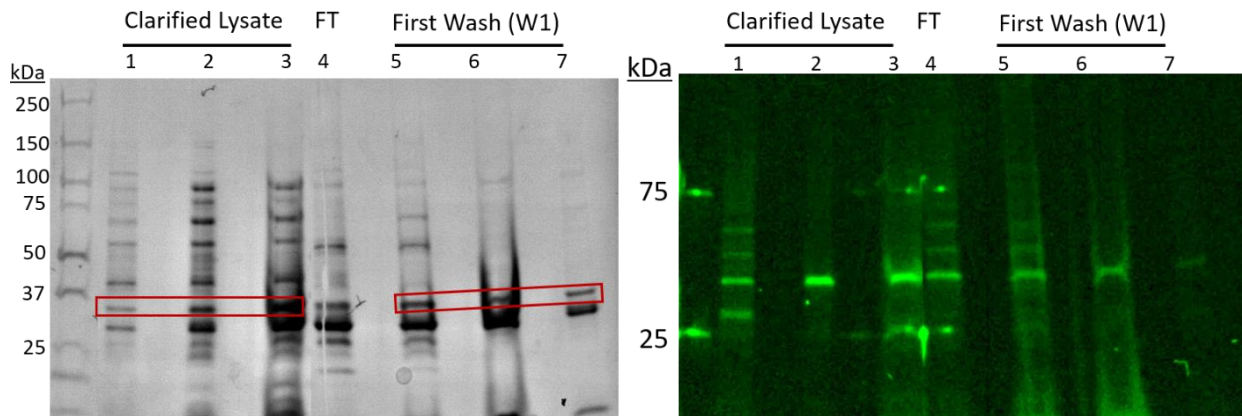


Figure D.1. Confirmation of 12-ADA-GBP presence in enriched (first wash) samples.

Coomassie-stained gel revealing protein distribution of clarified lysate vs. enriched (first wash) sample containing overexpressed 12-ADA-GBP; Fluorescent image of the same gel (imaged under Cy3 channel of c400 Azure gel analyzer) verifying presence of 12-ADA-GBP via SPAAC conjugation to DBCO-TAMRA in clarified lysate and enriched samples.

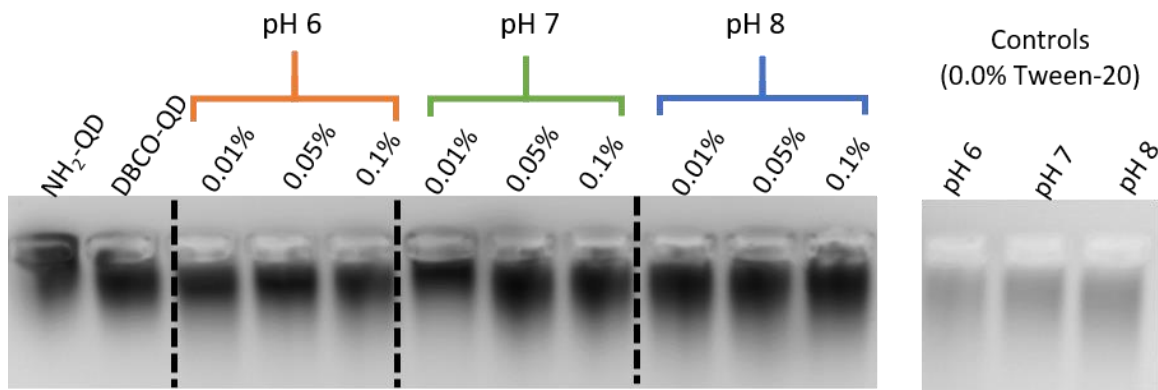


Figure D.2. Gel electrophoresis of DBCO-QDs in pH 6-8, 0.0-0.1% Tween-20.

Greater QD smearing further down the gel indicates positive surface charges (from DBCO incorporation), which may increase non-specific protein adsorption. Left-most lane included NH_2 -QD as a control to compare DBCO incorporation.

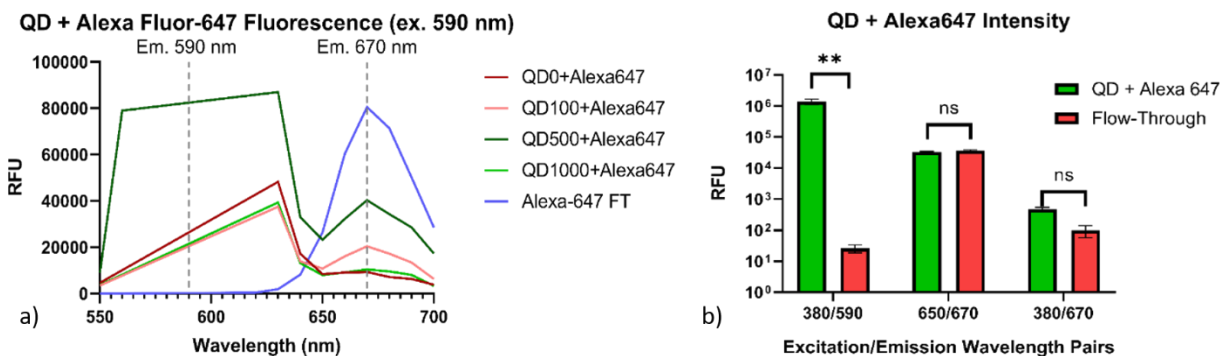


Figure D.3. Fluorescence spectra and emission intensity of DBCO-QDs clicked (via SPAAC) with Azide-Alexa-Fluor-647.

(a) Fluorescence emission spectra (excitation wavelength of 590 nm) of DBCO-QD (with linker:QD ratios of 0:1, 100:1, 500:1, and 1000:1) clicked (via SPAAC) to Azide-Alexa-Fluor-647. Fluorescence spectra of Alexa dye alone shows emission peak at 670 nm. QD500 demonstrated highest azide reactivity with second highest Alexa emission peak. (b) Fluorescence intensity of QD/Alexa-Fluor-647 conjugates at various wavelength pairs; samples were compared to flow-through containing excess Alexa-Fluor-647 dye. Fluorescence intensity of Alexa (em. 670 nm) was higher in conjugate sample compared to flow-through when excited at QD excitation wavelength (380 nm), indicating FRET due to covalent binding; difference was not significant.

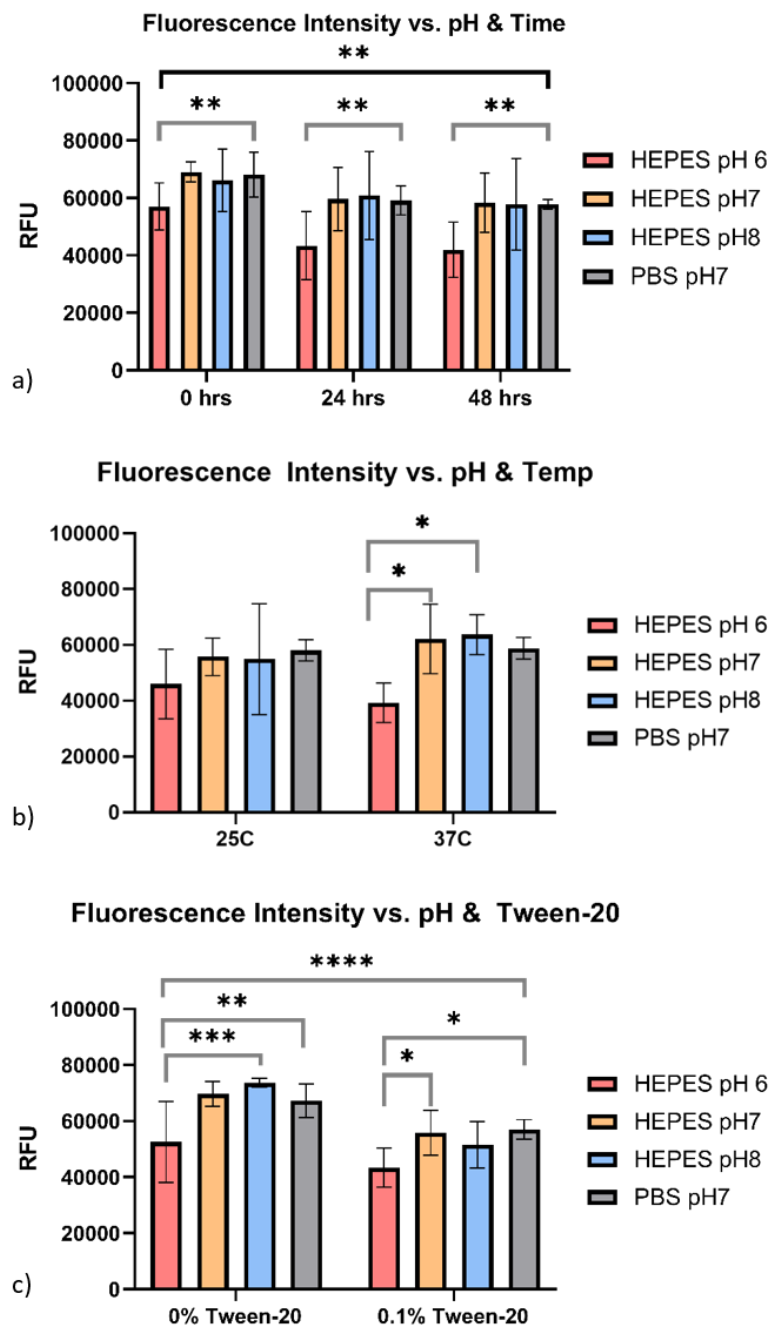


Figure D.4. QD fluorescence intensity under various buffer conditions.

(a) QD fluorescence intensity significantly decreased over time when stored at room temperature, regardless of buffer pH. Lower pH (6) significantly decreases fluorescence intensity. (b) Temperature does not affect fluorescence intensity of QDs. (c) Tween-20 significantly reduces QD fluorescence intensity. Across all experiments, higher pH (7-8) retained fluorescence intensity.

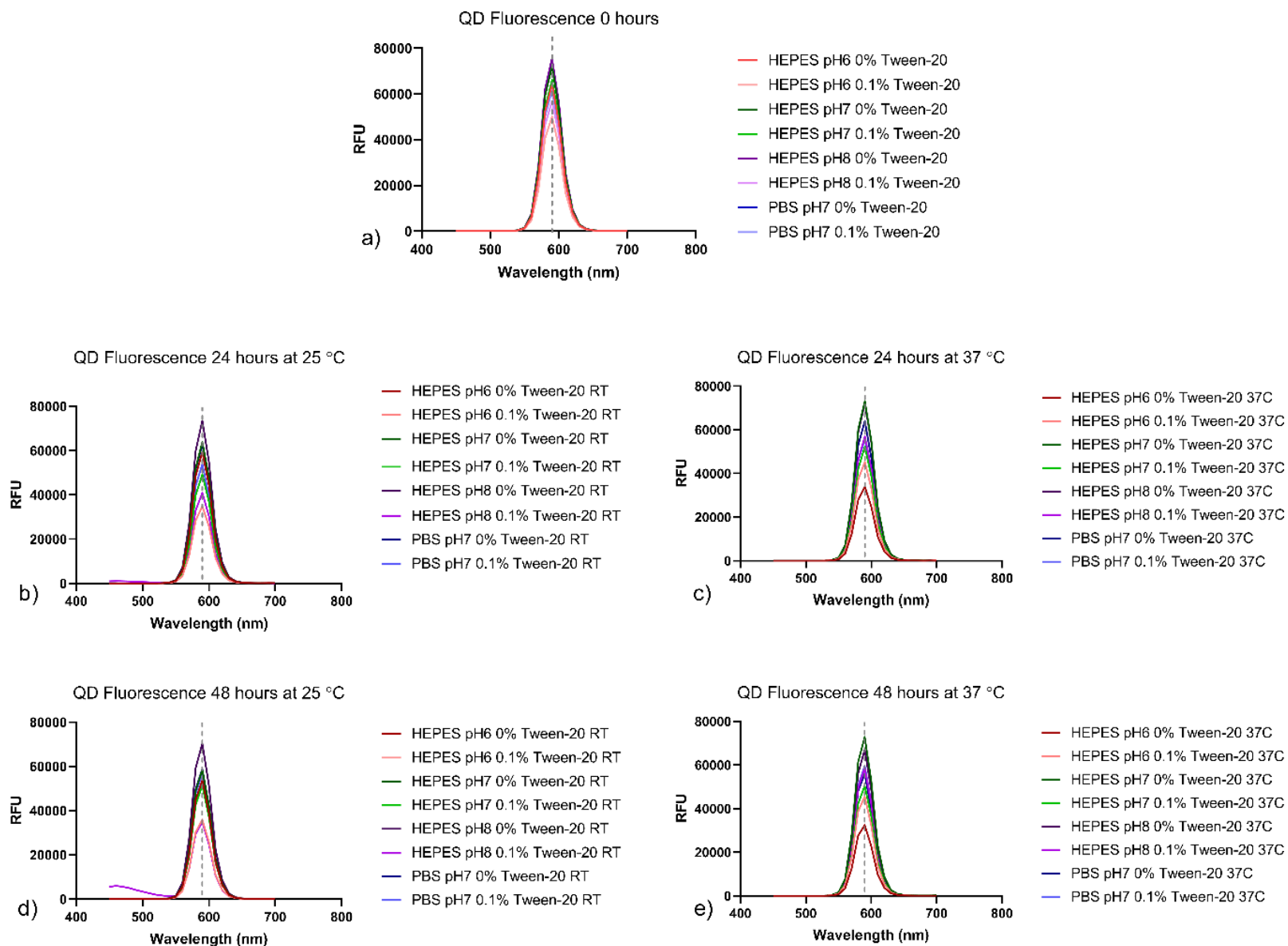


Figure D.5. QD fluorescence emission spectra under various buffer conditions over time.

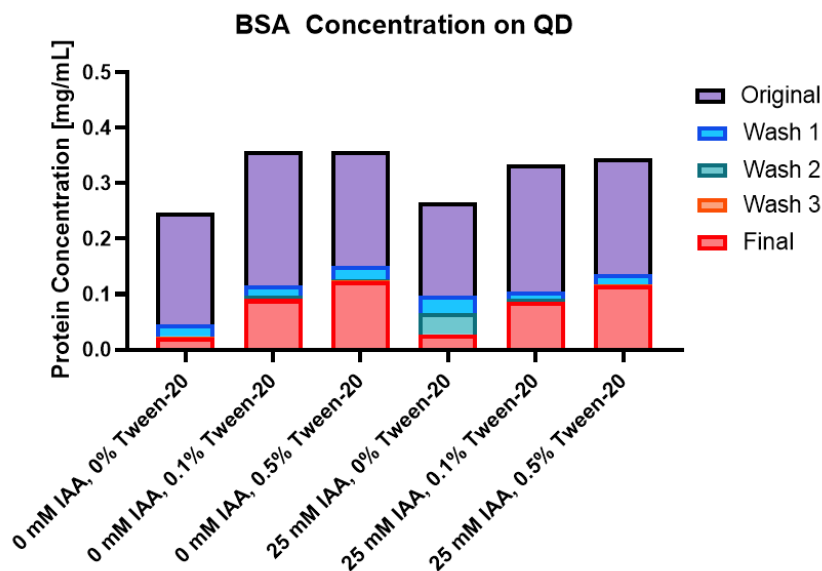


Figure D.6. Protein concentration (BSA) on DBCO-QDs after filtration steps (washes 1-3) and comparison of original and final (reconstituted) concentrations.

BSA (0.2 mg/mL) was incubated with DBCO-QDs under varying buffer conditions (20 mM HEPES, pH 7, +/- iodoacetamide (IAA), +/- Tween-20 (0.0%, 0.1%, 0.5%)) and filtered through 100 kDa MWCO Amicon Ultra 0.5 mL centrifugal filtration columns with 20 mM HEPES, pH 7 (three washes). Final, filtered sample was reconstituted to original QD concentration and protein concentrations were compared to original (starting) sample prior to filtration. Incubation with IAA in the absence of Tween-20 significantly reduced non-specific protein adsorption to DBCO-QDs.

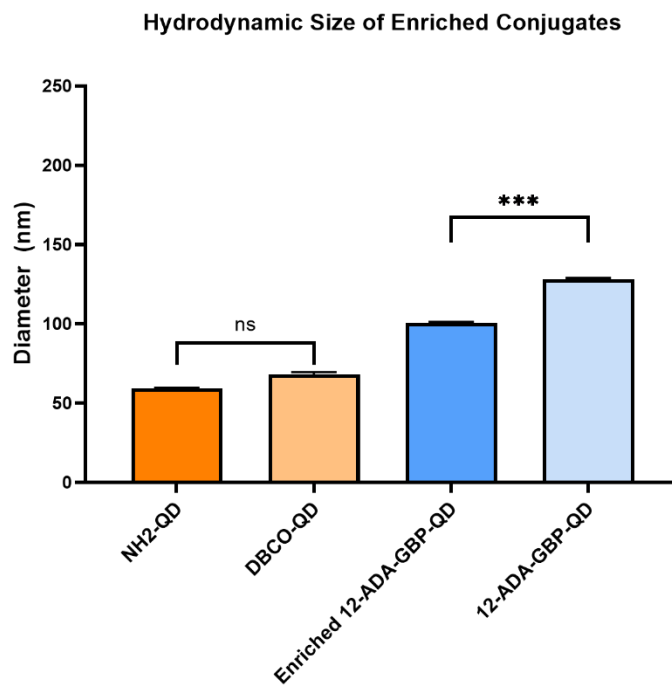


Figure D.7. Hydrodynamic diameter (nm) of GBP-QD conjugates compared to unfunctionalized QDs.

The average size of GBP-bound QDs was significantly higher than that of NH₂-QD and DBCO-QD; however, enrichment significantly reduced the size of the conjugate.

APPENDIX E. SUPPLEMENT TO CHAPTER 6

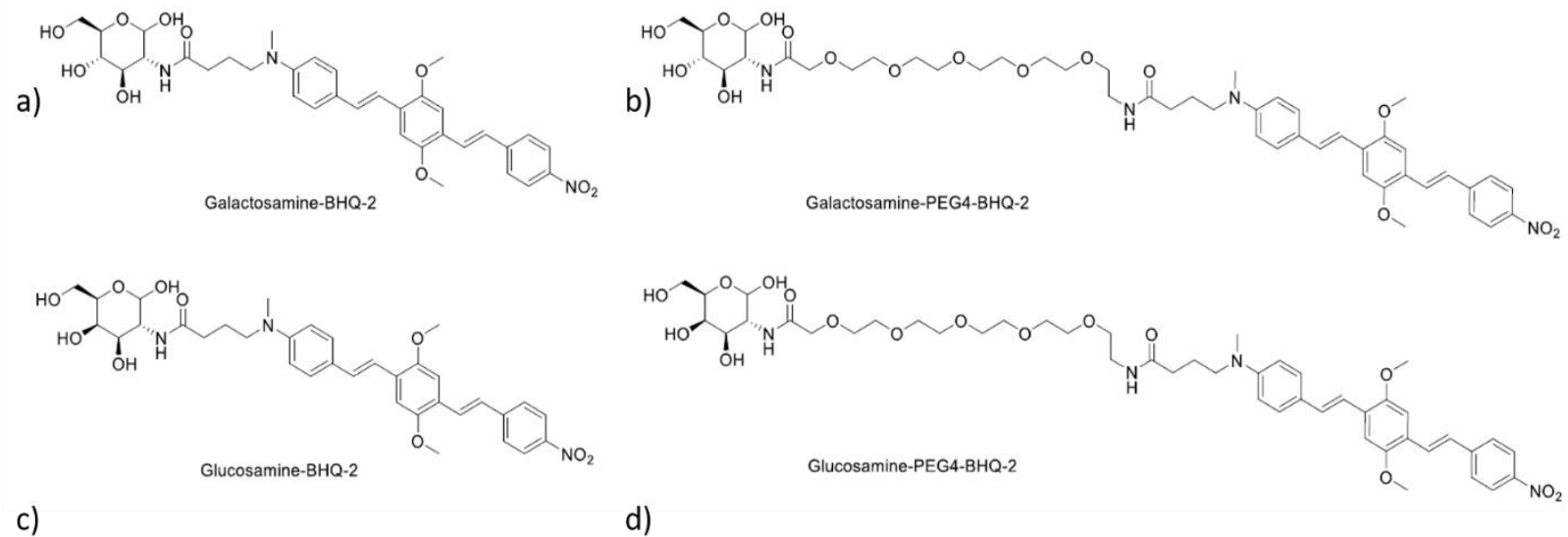


Figure E.1. Molecular structure of ligand quenchers.

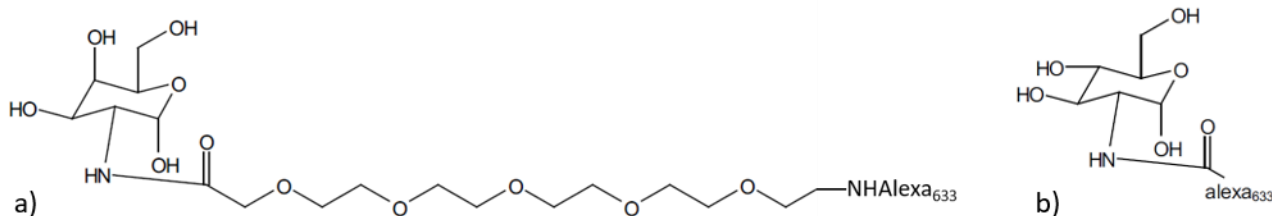


Figure E.2. Molecular conjugation structure of ligand acceptor molecules. (a) structure of glucosamine-PEG₆-Alexa-Fluor-633 (Target D); (b) structure of galactosamine-Alexa-Fluor-633 (Target A, not synthesized).

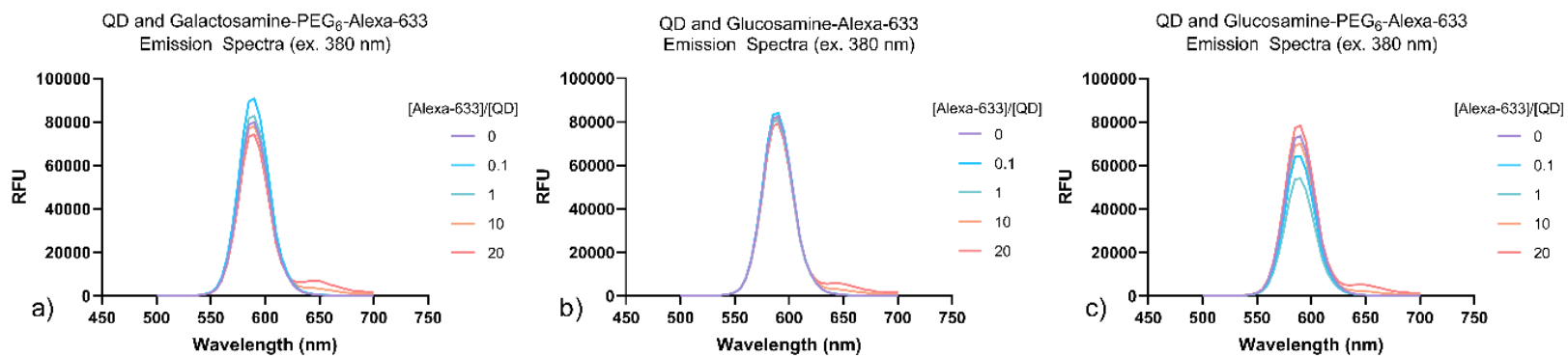


Figure E.3. Fluorescence emission spectra of NH₂-QD and ligand-Alexa-633 molecules (targets B-D) at increasing molar ratios of Alexa-633:QD (0, 0.1, 10, 20) Excitation wavelength of 380 nm; QD emission at 590 nm; Alexa-633 emission at 645 nm.

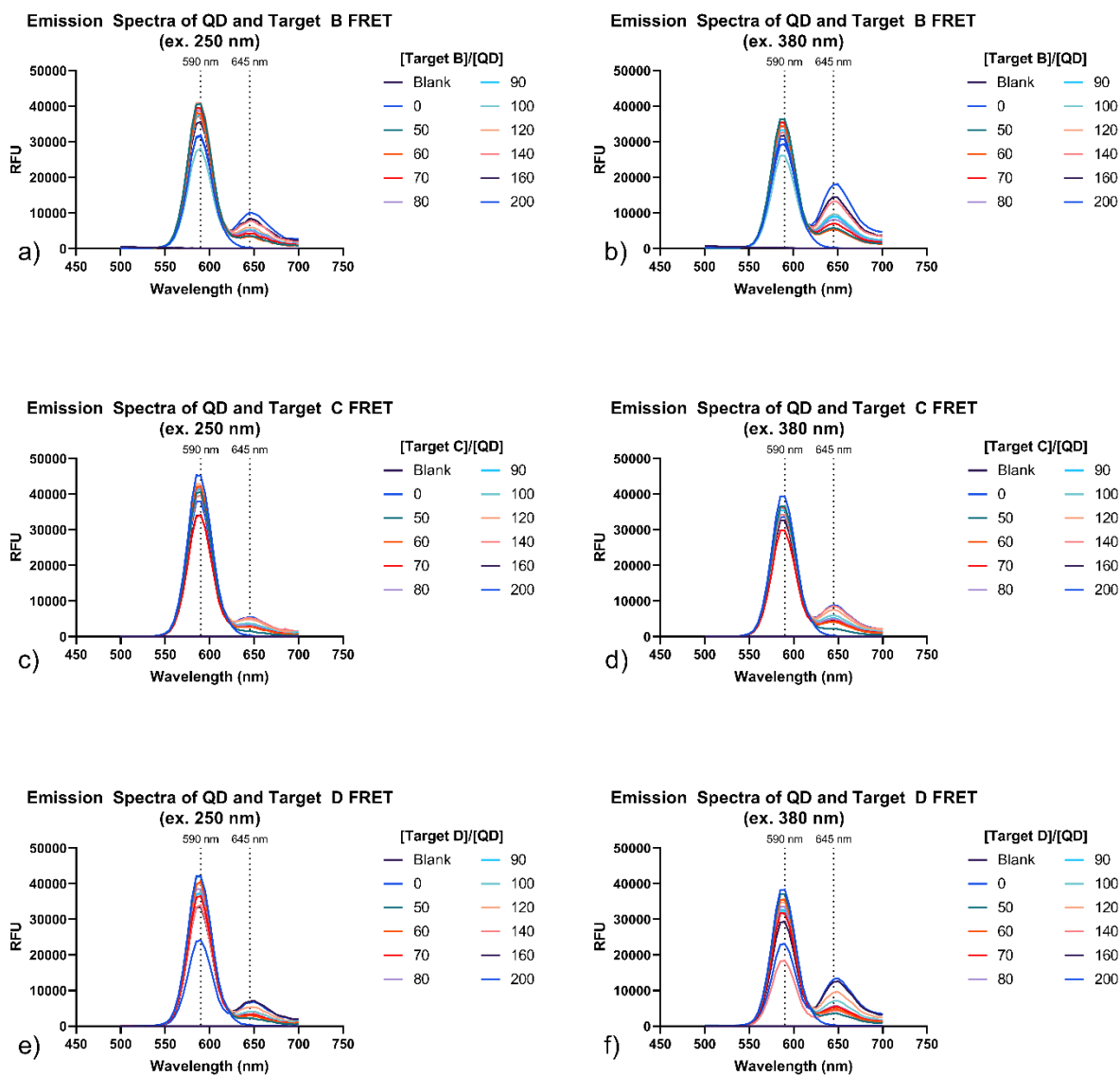


Figure E.4. Fluorescence emission spectra of NH₂-QD and ligand-Alexa-33 molecules (target B-D) at increasing molar ratios of Alexa-633:QD (0, 50-200). QD peak emission measured at 590 nm; Alexa-633 peak emission measured at 645 nm.

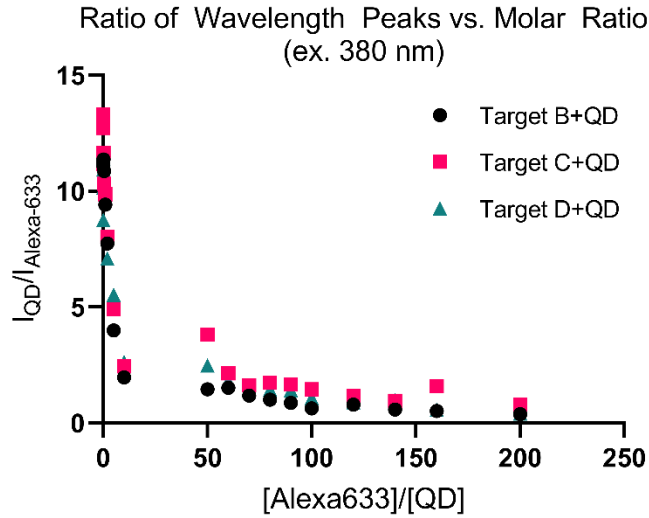


Figure E.5. Ratio of peak wavelength of QD (590 nm emission) to peak wavelength of ligand-Alexa-633 (645 nm emission, targets B-D) at increasing molar ratios of Alexa-633:QD (n=1).

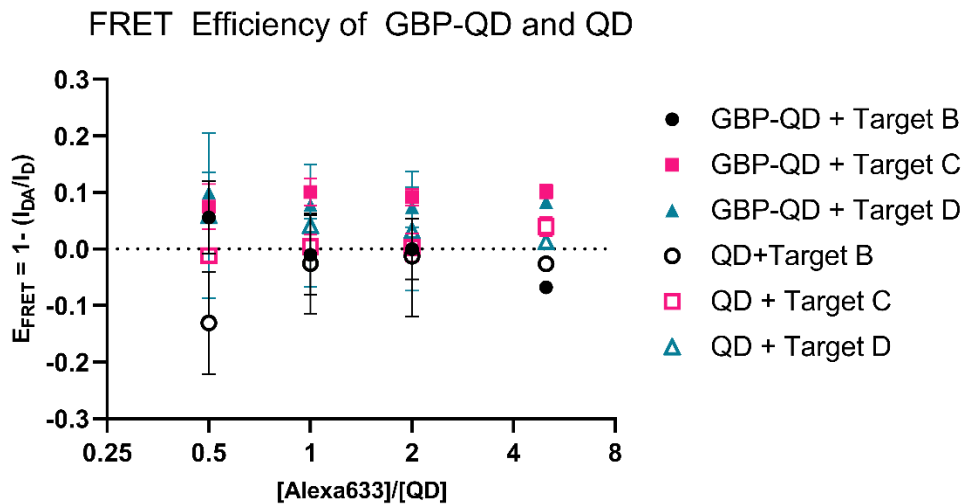


Figure E.6. FRET efficiency of individual ligand acceptors (Targets B-D) on both GBP-QD (closed symbols) and unbound QD (open symbols) at molar ratios (Alexa-633:QD) of 0.5, 1, 2, and 5 (n=4 for 0.5-2, n=1 for 5).

REFERENCES

1. Tankasala D, Linnes JC. Noninvasive glucose detection in exhaled breath condensate. *Translational Research*. 2019;213:1-22. doi:10.1016/j.trsl.2019.05.006
2. American Diabetes A. Diagnosis and Classification of Diabetes Mellitus. *Diabetes Care*. 2010;33(Suppl 1):S62-S69. doi:10.2337/dc10-S062
3. Services USD of H and H, ed. National Diabetes Statistics Report: Estimates of Diabetes and its Burden in the United States. Published online 2014.
4. Havas S. Educational guidelines for achieving tight control and minimizing complications of type 1 diabetes. *American family physician*. 1999;60(7):1985-1992,1997-1998.
5. Kovalaske MA, Gandhi GY. Glycemic Control in the Medical Intensive Care Unit. *Journal of Diabetes Science and Technology*. 2009;3(6):1330-1341.
6. Burge MR. Lack of Compliance With Home Blood Glucose Monitoring Predicts Hospitalization in Diabetes. *Diabetes Care*. 2001;24(8):1502 LP - 1503. doi:10.2337/diacare.24.8.1502
7. Canivell S, Gomis R. Diagnosis and classification of autoimmune diabetes mellitus. *Autoimmunity Reviews*. 2017;13(4-5):403-407. doi:10.1016/j.autrev.2014.01.020
8. Ontario HQ. Continuous Monitoring of Glucose for Type 1 Diabetes: A Health Technology Assessment. *Ontario health technology assessment series*. 2018;18(2):1-160.
9. American Diabetes A. Standards of Medical Care in Diabetes—2010. *Diabetes Care*. 2010;33(Suppl 1):S11-S61. doi:10.2337/dc10-S011
10. Ferrante do Amaral CE, Wolf B. Current development in non-invasive glucose monitoring. *Medical Engineering & Physics*. 2008;30(5):541-549. doi:http://dx.doi.org/10.1016/j.medengphy.2007.06.003
11. Vaddiraju S, Burgess DJ, Tomazos I, Jain FC, Papadimitrakopoulos F. Technologies for Continuous Glucose Monitoring: Current Problems and Future Promises. *Journal of Diabetes Science and Technology*. 2010;4(6):1540-1562.
12. Liakat S, Bors KA, Huang T-Y, Michel APM, Zanghi E, Gmachl CF. In vitro measurements of physiological glucose concentrations in biological fluids using mid-infrared light. *Biomedical Optics Express*. 2013;4(7):1083-1090. doi:10.1364/BOE.4.001083
13. Fogh-Andersen N, Altura BM, Altura BT, Siggaard-Andersen O. Composition of interstitial fluid. *Clinical Chemistry*. 1995;41(10):1522-1525.

14. Reim M, Lax F, Lichte H, Turss R. Steady State Levels of Glucose in the Different Layers of the Cornea, Aqueous Humor, Blood and Tears *in vivo*. *Ophthalmologica*. 1967;154(1):39-50.
15. Gupta S, Sandhu SV, Bansal H, Sharma D. Comparison of Salivary and Serum Glucose Levels in Diabetic Patients. *Journal of Diabetes Science and Technology*. 2015;9(1):91-96. doi:10.1177/1932296814552673
16. Baker EH, Clark N, Brennan AL, et al. Hyperglycemia and cystic fibrosis alter respiratory fluid glucose concentrations estimated by breath condensate analysis. *Journal of Applied Physiology*. 2007;102(5):1969-1975.
17. Mascarenhas P, Fatela B, Barahona I. Effect of Diabetes Mellitus Type 2 on Salivary Glucose – A Systematic Review and Meta-Analysis of Observational Studies. *PLoS ONE*. 2014;9(7):e101706. doi:10.1371/journal.pone.0101706
18. McNichols RJ, Cote GL. Optical glucose sensing in biological fluids: an overview. *Journal of Biomedical Optics*. 2000;5(1):5-16. doi:10.1117/1.429962
19. Tierney MJ, Tamada JA, Potts RO, et al. The GlucoWatch® biographer: a frequent, automatic and noninvasive glucose monitor. *Annals of Medicine*. 2000;32(9):632-641. doi:10.3109/07853890009002034
20. de Prost N, Saumon G. Glucose transport in the lung and its role in liquid movement. *Respiratory Physiology & Neurobiology*. 2007;159(3):331-337. doi:https://doi.org/10.1016/j.resp.2007.02.014
21. Franciosi L, Govorukhina N, ten Hacken N, Postma D, Bischoff R. Proteomics of Epithelial Lining Fluid Obtained by Bronchoscopic Microprobe Sampling BT - Nanoproteomics: Methods and Protocols. In: Toms SA, Weil RJ, eds. Humana Press; 2011:17-28. doi:10.1007/978-1-61779-319-6_2
22. Oliveira TL, Candeia-Medeiros Nřy, Cavalcante-Araęjo PM, et al. SGLT1 activity in lung alveolar cells of diabetic rats modulates airway surface liquid glucose concentration and bacterial proliferation. *Scientific reports*. 2016;6(1). doi:10.1038/srep21752
23. Bicer EM. Compositional characterisation of human respiratory tract lining fluids for the design of disease specific simulants. Published online 2014:428.
24. Philips BJ, Meguer J-X, Redman J, Baker EH. Factors determining the appearance of glucose in upper and lower respiratory tract secretions. *Intensive Care Medicine*. 2003;29(12):2204-2210. doi:10.1007/s00134-003-1961-2
25. Baker EH, Baines DL. Airway Glucose Homeostasis: A New Target in the Prevention and Treatment of Pulmonary Infection. *CHEST*. 2018;153(2):507-514. doi:10.1016/j.chest.2017.05.031

26. Kalsi KK, Baker EH, Fraser O, et al. Glucose homeostasis across human airway epithelial cell monolayers: role of diffusion, transport and metabolism. *Pflugers Arch - Eur J Physiol*. 2009;457(5):1061-1070. doi:10.1007/s00424-008-0576-4
27. Baker EH, Janaway CH, Philips BJ, et al. Hyperglycaemia is associated with poor outcomes in patients admitted to hospital with acute exacerbations of chronic obstructive pulmonary disease. *Thorax*. 2006;61(4):284-289. doi:10.1136/thx.2005.051029
28. Pezzulo AA, Gutiérrez J, Duschner KS, et al. Glucose Depletion in the Airway Surface Liquid Is Essential for Sterility of the Airways. Rojas M, ed. *PLoS ONE*. 2011;6(1):e16166. doi:10.1371/journal.pone.0016166
29. Hunt J. Exhaled breath condensate: An evolving tool for noninvasive evaluation of lung disease. *Journal of Allergy and Clinical Immunology*. 2002;110(1):28-34. doi:10.1067/mai.2002.124966
30. Baker EH, Clark N, Brennan AL, et al. Hyperglycemia and cystic fibrosis alter respiratory fluid glucose concentrations estimated by breath condensate analysis. *Journal of Applied Physiology*. 2007;102(5):1969-1975.
31. Rosias PP, Robroeks CM, Niemarkt HJ, et al. Breath condenser coatings affect measurement of biomarkers in exhaled breath condensate. *European Respiratory Journal*. 2006;28(5):1036-1041. doi:10.1183/09031936.06.00110305
32. Fronius M, Clauss W, Althaus M. Why Do We have to Move Fluid to be Able to Breathe? . *Frontiers in Physiology* . 2012;3:146.
33. Gessner C, Kuhn H, Seyfarth HJ, et al. Factors influencing breath condensate volume. *Pneumologie*. 2001;55(9):414-419. doi:10.1055/s-2001-16947
34. Effros RM, Biller J, Foss B, et al. A Simple Method for Estimating Respiratory Solute Dilution in Exhaled Breath Condensates. *American Journal of Respiratory and Critical Care Medicine*. 2003;168(12):1500-1505. doi:10.1164/rccm.200307-9200C
35. Effros RM, Hoagland KW, Bosbous M, et al. Dilution of Respiratory Solutes in Exhaled Condensates. *American Journal of Respiratory and Critical Care Medicine*. 2002;165(5):663-669. doi:10.1164/ajrccm.165.5.2101018
36. Dodig S, Čepelak I. Exhaled breath condensate – from an analytical point of view. *Biochemia Medica*. 2013;23(3):281-295. doi:10.11613/BM.2013.034
37. Minh TDC, Oliver SR, Ngo J, et al. Noninvasive measurement of plasma glucose from exhaled breath in healthy and type 1 diabetic subjects. *American Journal of Physiology - Endocrinology and Metabolism*. 2011;300(6):E1166-E1175.

38. Monge ME, Pérez JJ, Dwivedi P, et al. Ion mobility and liquid chromatography/mass spectrometry strategies for exhaled breath condensate glucose quantitation in cystic fibrosis studies. *Rapid Communications in Mass Spectrometry*. 2013;27(20):2263-2271. doi:10.1002/rcm.6683
39. E.M. K, A.S. L, A.S. T, P.K. B. Exhaled Breath Condensate: Technical and Diagnostic Aspects. *Scientific World Journal*. 2015;2015. doi:10.1155/2015/435160
40. Roberts K, Jaffe A, Verge C, Thomas PS. Noninvasive monitoring of glucose levels: is exhaled breath the answer? *Journal of diabetes science and technology*. 2012;6(3):659-664. doi:10.1177/193229681200600322
41. Gläser S, Krüger S, Merkel M, Bramlage P, Herth FJF. Chronic Obstructive Pulmonary Disease and Diabetes Mellitus: A Systematic Review of the Literature. *Respiration*. 2015;89(3):253-264. doi:10.1159/000369863
42. Mallia P, Webber J, Gill SK, et al. Role of airway glucose in bacterial infections in patients with chronic obstructive pulmonary disease. *Journal of Allergy and Clinical Immunology*. 2018;142(3):815-823.e6. doi:https://doi.org/10.1016/j.jaci.2017.10.017
43. Hunt J. Exhaled Breath Condensate—an overview. *Immunology and allergy clinics of North America*. 2007;27(4):587-v. doi:10.1016/j.iac.2007.09.001
44. Gessner C, Kuhn H, Seyfarth HJ, et al. Factors influencing breath condensate volume. *Pneumologie*. 2001;55(9):414-419. doi:10.1055/s-2001-16947
45. Soyer OU, Dizdar EA, Keskin O, Lilly C, Kalayci O. Comparison of two methods for exhaled breath condensate collection. *Allergy*. 2006;61(8):1016-1018. doi:10.1111/j.1398-9995.2006.01064.x
46. Hedenstierna G, Sandhagen B. Assessing dead space. A meaningful variable? *Minerva Anestesiologica*. 2006;72(6):521-528.
47. ECoScreen and ECoCheck - FILT. Accessed April 29, 2020. http://www.filt.de/ecoscreen_ecocheck.html?&L=1
48. Mohan AP, Rundell AE, Park K, Ziaie B, Wodicka GR. Establishing a Functional Relationship Between the Glucose Concentrations in Exhaled Breath Condensates and Blood. 2010;9.
49. Hamilton II M. Standardizing the Collection and Measurement of Glucose in Exhaled Breath and Its Relationship To Blood Glucose Concentrations. *Master's Thesis*. Published online 2014. doi:3402307
50. Forbat LN, Collins RE, Maskell GK, Sönksen PH. Glucose concentrations in parotid fluid and venous blood of patients attending a diabetic clinic. *Journal of the Royal Society of Medicine*. 1981;74(10):725-728.

51. López ME, Colloca ME, Páez RG, Schallmach JN, Koss MA, Chervonagura A. Salivary characteristics of diabetic children . *Brazilian Dental Journal* . 2003;14:26-31.
52. Jurysta C, Bulur N, Oguzhan B, et al. Salivary Glucose Concentration and Excretion in Normal and Diabetic Subjects. *Journal of Biomedicine and Biotechnology*. 2009;2009:430426. doi:10.1155/2009/430426
53. Mutlu GM, Garey KW, Robbins RA, Danziger LH, Rubinstein I. Pulmonary Perspective Collection and Analysis of Exhaled Breath Condensate in Humans. *Am J Respir Crit Care Med*. 2001;164:731-737. doi:10.1164/ajrccm.164.5.2101032
54. Yoo E-H, Lee S-Y. Glucose Biosensors: An Overview of Use in Clinical Practice. *Sensors (Basel, Switzerland)*. 2010;10(5):4558-4576. doi:10.3390/s100504558
55. Bhalla N, Jolly P, Formisano N, Estrela P. Introduction to biosensors. *Essays In Biochemistry*. 2016;60(1):1-8.
56. Chambers JP, Arulanandam BP, Matta LL, Weis A, Valdes JJ. Biosensor Recognition Elements. *Curr Issus Mol Biol*. 2008;10(1-2):1-12.
57. Kim J, Campbell AS, Wang J. Wearable non-invasive epidermal glucose sensors: A review. *Talanta*. 2018;177:163-170. doi:https://doi.org/10.1016/j.talanta.2017.08.077
58. Soni A, Jha SK. Smartphone based non-invasive salivary glucose biosensor. *Analytica Chimica Acta*. 2017;996:54-63. doi:https://doi.org/10.1016/j.aca.2017.10.003
59. Dominguez RB, Orozco MA, Chávez G, Márquez-Lucero A. The Evaluation of a Low-Cost Colorimeter for Glucose Detection in Salivary Samples. *Sensors (Basel, Switzerland)*. 2017;17(11):2495. doi:10.3390/s17112495
60. Liu C, Sheng Y, Sun Y, et al. A glucose oxidase-coupled DNAzyme sensor for glucose detection in tears and saliva. *Biosensors and Bioelectronics*. 2015;70:455-461. doi:https://doi.org/10.1016/j.bios.2015.03.070
61. Bankar SB, Bule M V, Singhal RS, Ananthanarayan L. Glucose oxidase — An overview. *Biotechnology Advances*. 2009;27(4):489-501. doi:https://doi.org/10.1016/j.biotechadv.2009.04.003
62. Degani Y, Heller A. Electrical communication between redox centers of glucose oxidase and electrodes via electrostatically and covalently bound redox polymers. *Journal of the American Chemical Society*. 1989;111(6):2357-2358. doi:10.1021/ja00188a091
63. Degani Y, Heller A. Direct electrical communication between chemically modified enzymes and metal electrodes. I. Electron transfer from glucose oxidase to metal electrodes via electron relays, bound covalently to the enzyme. *The Journal of Physical Chemistry*. 1987;91(6):1285-1289. doi:10.1021/j100290a001

64. Ferri S, Kojima K, Sode K. Review of Glucose Oxidases and Glucose Dehydrogenases: A Bird's Eye View of Glucose Sensing Enzymes. *Journal of Diabetes Science and Technology*. 2011;5(5):1068-1076.
65. Oliver NS, Toumazou C, Cass AEG, Johnston DG. Glucose sensors: a review of current and emerging technology. *Diabetic Medicine*. 2009;26(3):197-210. doi:10.1111/j.1464-5491.2008.02642.x
66. Wang J. Electrochemical Glucose Biosensors. *Chemical Reviews*. 2008;108(2):814-825. doi:10.1021/cr068123a
67. Clark LC, Lyons C. Electrode systems for continuous monitoring in cardiovascular surgery. *Annals of the New York Academy of Sciences*. 1962;102(1):29-45. doi:10.1111/j.1749-6632.1962.tb13623.x
68. Wang J, Liu J, Chen L, Lu F. Highly Selective Membrane-Free, Mediator-Free Glucose Biosensor. *Analytical Chemistry*. 1994;66(21):3600-3603. doi:10.1021/ac00093a011
69. Ferri S, Kojima K, Sode K. Review of Glucose Oxidases and Glucose Dehydrogenases: A Bird's Eye View of Glucose Sensing Enzymes. *Journal of Diabetes Science and Technology*. 2011;5(5):1068-1076.
70. Tolosa L, Rao G. The Glucose Binding Protein as Glucose Sensor. In: Geddes CD, Lakowicz JR, eds. *Glucose Sensing*. Springer US; 2006:323-331. doi:10.1007/0-387-33015-1_13
71. Holland JT, Harper JC, Dolan PL, et al. Rational Redesign of Glucose Oxidase for Improved Catalytic Function and Stability. *PLoS One*. 2012;7(6). doi:10.1371/journal.pone.0037924
72. Kang BS, Wang HT, Ren F, et al. Enzymatic glucose detection using ZnO nanorods on the gate region of AlGaIn/GaN high electron mobility transistors. *Applied Physics Letters*. 2007;91(25):252103. doi:10.1063/1.2825574
73. Chu BH, Kang BS, Hung SC, et al. Aluminum gallium nitride (GaIn)/GaN high electron mobility transistor-based sensors for glucose detection in exhaled breath condensate. *Journal of diabetes science and technology*. 2010;4(1):171-179. doi:10.1177/193229681000400122
74. Xiong Y, Zhang Y, Rong P, Yang J, Wang W, Liu D. A high-throughput colorimetric assay for glucose detection based on glucose oxidase-catalyzed enlargement of gold nanoparticles. *Nanoscale*. 2015;7(38):15584-15588. doi:10.1039/C5NR03758A
75. Zhai H, Bai Y, Qin J, Feng F. Colorimetric and Ratiometric Fluorescence Dual-Mode Sensing of Glucose Based on Carbon Quantum Dots and Potential UV/Fluorescence of o-Diaminobenzene. *Sensors*. 2019;19(3). doi:10.3390/s19030674

76. Sakaguchi Y, Minamikawa T, Yamamuro M, et al. Time-resolved Fluorescent Detection for Glucose Using a Complex of Luminescent Layered Titanates and Enzymes. *Analytical Sciences*. 2017;33(9):989-991. doi:10.2116/analsci.33.989
77. Endo T, Ikeda R, Yanagida Y, Hatsuzawa T. Stimuli-responsive hydrogel–silver nanoparticles composite for development of localized surface plasmon resonance-based optical biosensor. *Analytica Chimica Acta*. 2008;611(2):205-211. doi:https://doi.org/10.1016/j.aca.2008.01.078
78. Tang B, Cao L, Xu K, et al. A New Nanobiosensor for Glucose with High Sensitivity and Selectivity in Serum Based on Fluorescence Resonance Energy Transfer (FRET) between CdTe Quantum Dots and Au Nanoparticles. *Chemistry – A European Journal*. 2008;14(12):3637-3644. doi:10.1002/chem.200701871
79. Yuan J, Guo W, Yin J, Wang E. Glutathione-capped CdTe quantum dots for the sensitive detection of glucose. *Talanta*. 2009;77(5):1858-1863. doi:http://dx.doi.org/10.1016/j.talanta.2008.10.032
80. Duong HD, Rhee J II. Use of CdSe/ZnS core-shell quantum dots as energy transfer donors in sensing glucose. *Talanta*. 2007;73(5):899-905. doi:http://dx.doi.org/10.1016/j.talanta.2007.05.011
81. Huang X, Wang J, Liu H, Lan T, Ren J. Quantum dot-based FRET for sensitive determination of hydrogen peroxide and glucose using tyramide reaction. *Talanta*. 2013;106:79-84. doi:https://doi.org/10.1016/j.talanta.2012.12.014
82. Cao L, Ye J, Tong L, Tang B. A New Route to the Considerable Enhancement of Glucose Oxidase (GOx) Activity: The Simple Assembly of a Complex from CdTe Quantum Dots and GOx, and Its Glucose Sensing. *Chemistry – A European Journal*. 2008;14(31):9633-9640. doi:10.1002/chem.200800681
83. Srinivasan G, Chen J, Parisi J, Brückner C, Yao X, Lei Y. An Injectable PEG-BSA-Coumarin-GOx Hydrogel for Fluorescence Turn-on Glucose Detection. *Applied Biochemistry and Biotechnology*. 2015;177(5):1115-1126. doi:10.1007/s12010-015-1800-2
84. Pires NMM, Dong T, Hanke U, Hoivik N. Recent Developments in Optical Detection Technologies in Lab-on-a-Chip Devices for Biosensing Applications. *Sensors (Basel, Switzerland)*. 2014;14(8):15458-15479. doi:10.3390/s140815458
85. Malikkides CO, Weiland RH. On the mechanism of immobilized glucose oxidase deactivation by hydrogen peroxide. *Biotechnology and Bioengineering*. 1982;24(11):2419-2439. doi:10.1002/bit.260241109
86. Salins LLE, Ware RA, Ensor CM, Daunert S. A Novel Reagentless Sensing System for Measuring Glucose Based on the Galactose/Glucose-Binding Protein. *Analytical Biochemistry*. 2001;294(1):19-26. doi:https://doi.org/10.1006/abio.2001.5131

87. Khan F, Gnudi L, Pickup JC. Fluorescence-based sensing of glucose using engineered glucose/galactose-binding protein: A comparison of fluorescence resonance energy transfer and environmentally sensitive dye labelling strategies. *Biochemical and Biophysical Research Communications*. 2008;365(1):102-106. doi:10.1016/j.bbrc.2007.10.129
88. Hsieh H V., Sherman DB, Andaluz SA, Amiss TJ, Pitner JB. Fluorescence resonance energy transfer glucose sensor from site-specific dual labeling of glucose/galactose binding protein using ligand protection. *Journal of Diabetes Science and Technology*. 2012;6(6):1286-1295. doi:10.1177/193229681200600607
89. Quinn CP, Pathak CP, Heller A, Hubbell JA. Photo-crosslinked copolymers of 2-hydroxyethyl methacrylate, poly(ethylene glycol) tetra-acrylate and ethylene dimethacrylate for improving biocompatibility of biosensors. *Biomaterials*. 1995;16(5):389-396. doi:http://dx.doi.org/10.1016/0142-9612(95)98856-9
90. Ballerstadt R, Schultz JS. A Fluorescence Affinity Hollow Fiber Sensor for Continuous Transdermal Glucose Monitoring. *Analytical Chemistry*. 2000;72(17):4185-4192. doi:10.1021/ac000215r
91. Ballerstadt R, Polak A, Beuhler A, Frye J. In vitro long-term performance study of a near-infrared fluorescence affinity sensor for glucose monitoring. *Biosensors and Bioelectronics*. 2004;19(8):905-914. doi:http://dx.doi.org/10.1016/j.bios.2003.08.019
92. Tolosa L, Malak H, Raob G, Lakowicz JR. Optical assay for glucose based on the luminescence decay time of the long wavelength dye Cy5TM. *Sensors and Actuators B: Chemical*. 1997;45(2):93-99. doi:http://dx.doi.org/10.1016/S0925-4005(97)00275-X
93. Rolinski OJ, Birch DJS, McCartney LJ, Pickup JC. Fluorescence resonance energy transfer from allophycocyanin to malachite green. *Chemical Physics Letters*. 1999;309(5-6):395-401. doi:http://dx.doi.org/10.1016/S0009-2614(99)00707-1
94. Pickup JC, Hussain F, Evans ND, Rolinski OJ, Birch DJS. Fluorescence-based glucose sensors. *Biosensors and Bioelectronics*. 2005;20(12):2555-2565. doi:http://dx.doi.org/10.1016/j.bios.2004.10.002
95. Medintz IL, Clapp AR, Mattoussi H, Goldman ER, Fisher B, Mauro JM. Self-assembled nanoscale biosensors based on quantum dot FRET donors. *Nat Mater*. 2003;2(9):630-638. doi:http://www.nature.com/nmat/journal/v2/n9/supinfo/nmat961_S1.html
96. Tankasala D, Ng GP, Smith MS, Bendell JR, Linnes JC. Selective Collection and Condensation of Exhaled Breath for Glucose Detection. In: *2018 40th Annual International Conference of the IEEE Engineering in Medicine and Biology Society (EMBC)*. ; 2018:3890-3893. doi:10.1109/EMBC.2018.8513393
97. Whipp BJ. Pulmonary Ventilation BT - Comprehensive Human Physiology: From Cellular Mechanisms to Integration. In: Greger R, Windhorst U, eds. Springer Berlin Heidelberg; 1996:2015-2036. doi:10.1007/978-3-642-60946-6_101

98. Verscheure S, Massion PB, Verschuren F, Damas P, Magder S. Volumetric capnography: Lessons from the past and current clinical applications. *Critical Care*. 2016;20(1):1-9. doi:10.1186/s13054-016-1377-3
99. Schubert JK, Spittler K-H, Braun G, Geiger K, Guttman J. CO₂-controlled sampling of alveolar gas in mechanically ventilated patients. *Journal of Applied Physiology*. 2001;90(2):486-492. doi:10.1152/jappl.2001.90.2.486
100. Karlen W, Turner M, Cooke E, Dumont G, Ansermino JM. CapnoBase: Signal database and tools to collect, share and annotate respiratory signals. In: *Annual Meeting of the Society for Technology in Anesthesia (STA)*. ; 2010.
101. Miller DM, Olson JS, Quioco FA. The Mechanism of Sugar Binding to the Periplasmic Receptor for Galactose Chemotaxis and Transport in Escherichia coli. *The Journal of Biological Chemistry*. 1980;255(6):2465-2471.
102. Tiangco C, Fon D, Sardesai N, et al. Fiber optic biosensor for transdermal glucose based on the glucose binding protein. *Sensors and Actuators B: Chemical*. 2017;242:569-576. doi:https://doi.org/10.1016/j.snb.2016.11.077
103. Kulkarni C, Lo M, Fraseur JG, Tirrell DA, Kinzer-Ursem TL. Bioorthogonal Chemoenzymatic Functionalization of Calmodulin for Bioconjugation Applications. *Bioconjugate Chemistry*. 2015;26(10):2153-2160. doi:10.1021/acs.bioconjchem.5b00449
104. Heal WP, Wright MH, Thinon E, Tate EW. Multifunctional protein labeling via enzymatic N-terminal tagging and elaboration by click chemistry. *Nature Protocols*. 2011;7:105.
105. Pickens CJ, Johnson SN, Pressnall MM, Leon MA, Berkland CJ. Practical Considerations, Challenges, and Limitations of Bioconjugation via Azide–Alkyne Cycloaddition. *Bioconjugate Chemistry*. 2018;29(3):686-701. doi:10.1021/acs.bioconjchem.7b00633
106. Mann VR, Powers AS, Tilley DC, Sack JT, Cohen BE. Azide–Alkyne Click Conjugation on Quantum Dots by Selective Copper Coordination. *ACS Nano*. 2018;12(5):4469-4477. doi:10.1021/acsnano.8b00575
107. Agard NJ, Prescher JA, Bertozzi CR. A Strain-Promoted [3 + 2] Azide–Alkyne Cycloaddition for Covalent Modification of Biomolecules in Living Systems. *Journal of the American Chemical Society*. 2004;126(46):15046-15047. doi:10.1021/ja044996f
108. Steiner M-S, Duerkop A, Wolfbeis OS. Optical methods for sensing glucose. *Chemical Society Reviews*. 2011;40(9):4805-4839. doi:10.1039/C1CS15063D
109. van Geel R, Pruijn GJM, van Delft FL, Boelens WC. Preventing Thiol-Yne Addition Improves the Specificity of Strain-Promoted Azide–Alkyne Cycloaddition. *Bioconjugate Chemistry*. 2012;23(3):392-398. doi:10.1021/bc200365k

110. Schieber C, Bestetti A, Lim JP, et al. Conjugation of Transferrin to Azide-Modified CdSe/ZnS Core-Shell Quantum Dots using Cyclooctyne Click Chemistry. *Angew Chem Int Ed*. 2012;51(42):10523-10527. doi:10.1002/anie.201202876
111. Hsieh HV, Sherman DB, Andaluz SA, Amiss TJ, Pitner JB. Fluorescence resonance energy transfer glucose sensor from site-specific dual labeling of glucose/galactose binding protein using ligand protection. *Journal of Diabetes Science and Technology*. 2012;6(6):1286-1295. doi:10.1177/193229681200600607
112. Medintz IL, Goldman ER, Lassman ME, Mauro JM. A fluorescence resonance energy transfer sensor based on maltose binding protein. *Bioconjugate Chemistry*. 2003;14(5):909-918. doi:10.1021/bc020062+
113. Borrok MJ, Kiessling LL, Forest KT. Conformational changes of glucose/galactose-binding protein illuminated by open, unliganded, and ultra-high-resolution ligand-bound structures. *Protein science: a publication of the Protein Society*. 2007;16(6):1032-1041. doi:10.1110/ps.062707807
114. FRET and FCS—Friends or Foes? - Sahoo - 2011 - ChemPhysChem - Wiley Online Library. Accessed July 24, 2020. <https://chemistry-europe.onlinelibrary.wiley.com/doi/abs/10.1002/cphc.201000776>
115. Kilpatrick LE, Hill SJ. The use of fluorescence correlation spectroscopy to characterize the molecular mobility of fluorescently labelled G protein-coupled receptors. *Biochem Soc Trans*. 2016;44(2):624-629. doi:10.1042/BST20150285
116. Shah NB, Duncan TM. Bio-layer Interferometry for Measuring Kinetics of Protein-protein Interactions and Allosteric Ligand Effects. *J Vis Exp*. 2014;(84). doi:10.3791/51383
117. Aloraefy M, Pfefer TJ, Ramella-Roman JC, Sapsford KE. In Vitro Evaluation of Fluorescence Glucose Biosensor Response. *Sensors*. 2014;14(7):12127-12148. doi:10.3390/s140712127
118. Effros RM, Hoagland KW, Bosbous M, et al. Dilution of Respiratory Solutes in Exhaled Condensates. 2002;165:7.
119. Roberts K, Jaffe A, Verge C, Thomas PS. Noninvasive Monitoring of Glucose Levels: Is Exhaled Breath the Answer? *J Diabetes Sci Technol*. 2012;6(3):659-664.

PUBLICATIONS

D Tankasala and J Linnes. "Non-Invasive Glucose Detection in Exhaled Breath Condensate." *Translational Research (Invited Review)*. May 2019.

D Tankasala, G Ng, M Smith, J Bendell, and J Linnes. "Selective Collection and Condensation of Exhaled Breath for Glucose Detection." *IEEE EMBS. (Conference Proceeding)*. October 2018.

S K Misra, F Ostadhosseini, R. Babu, J Kus, D Tankasala, A Sutrisno, K A. Walsh, C R Bromfield, and D Pan. "3D-Printed Multi-drug-eluting Stent from Graphene-nanoplatelet-doped Biodegradable Polymer Composite." *Advanced Healthcare Materials*. Mar 2017.